Cape Peninsula University of Technology

Microstructural effects on properties of additively manufactured Inconel 625 and 718

By

Theo-Neal Booysen

Thesis submitted in partial/fulfilment of the requirements for the degree

Master of Engineering: Mechanical Engineering

In the Faculty of Engineering

at the Cape Peninsula University of Technology

Supervisor: Dr. O. Nemraoui

Co Supervisor Dr. S. Khamlich

Bellville Campus

31 October 2019

DECLARATION

I, Theo-Neal Willando Jade Booysen, declare that the contents of this dissertation/thesis represent my own unaided work, and that the dissertation/thesis has not previously been submitted for academic examination towards any qualification. Furthermore, it represents my own opinions and not necessarily those of the Cape Peninsula University of Technology.

Signed:  **Date: 31 October 2019**

ABSTRACT

Three Dimensional(3D) printing is known as additive manufacturing: it is a method of manufacturing parts or components form sheet, wire or powder in a manufacturing process. This method differs from traditional manufacturing techniques such as casting, moulding or subtracting materials which already exist. The type of material characterization is also very important in the development and improve or manufacturing of new materials for higher strength and various application. Selective Laser Melting(SLM) an additive manufacturing powder-based process has been adopted by automotive and aerospace industries. The reason for this is that it has many potential benefits, such as 3D designs of complex components in a shortened time frame, which offers financial savings. SLM process use metallic powders with different chemical composition to manufacture complex structures, which is an innovative material processing technology.

In this research SLM, a typical additive manufacture process method, was used to manufacture additively manufactured Inconel 625 and 718. These sample specimens were investigated to determine their microstructural features and mechanical properties. The microstructural features were characterized using two different experimental surface microscopy methods: scanning electron microscope(SEM) and light optical microscope (LOM). The mechanical properties were determined by studying deformation and hardness characteristics using three-point bending and hardness tests. The relationship between processing, microstructure, grain sizes and mechanical properties was established.

The understanding of SLM additive manufacturing of alloys is important as well for the adoption of the technology, and the possibility of replacing commercially produced cast and wrought alloys in the near future.

ACKNOWLEDGEMENTS

I wish to thank:

- Chanel Booysen, my wife who always kept me motivated to finish this thesis
- Dr. Ouassini Nemraoui, my supervisor for his input and guidance during my research
- Dr. Saleh Khamlich, my co-supervisor for providing sample specimens for analysis
- Prof. Graeme Oliver, for lecturing course-based subjects
- Lab assistants, for preparation and analysis of sample specimens

DEDICATION

I would like to dedicate my research to family for their inspiration and for supporting every step of the way during my studies. I owe my life achievements to God and my parents, Thank you, Mom and Dad for everything you have done for me.

LIST OF SYMBOLS

Units	Description
θ	theta
λ	lambda
^0C	celsius
μA	micro-Ampere
μm	micro-metres
cm^3	cubic centimetre
g	grams
K	Kelvin
kx	high magnification scale
kg	kilograms
kN	kiloNewtons
kV	kilovolts
mm	millimeters
ml	millilitres
mm^2	square millimetres
MPa	mega-pascals
nm	nanometres
N	Newtons
rpm	revolutions per minute

TABLE OF CONTENTS

LIST OF FIGURES

LIST OF TABLES

CHAPTER 1

1.0 Introduction

For the purpose of understanding the development and prediction of microstructure and properties of additive manufacturing of materials, computational techniques have proven to be a very useful tool to gather insight into additive manufacturing processes and conditioning (Ott et al.,2018). The additive manufacturing process comes with challenges, namely heat transfers and fluid mechanics that occur during melting and re solidification. According to Badiru et al. (2017), the thermal form heat transfers subsequently impacts the solid and solid-to-solid phase transformation and marco scale of any change in temperature. The information from micro scale models will predict an important characteristics of the materials microstructure which include grain morphology, grain size, aspect ratio, precipitate volume fraction and size and build up of plastic strain (Deng et al., 2018; Ott et al., 2018). This process must be developed to translate these microstructural characteristics into mechanical property predictions (Ott et al., 2018). Today much of the focus has been towards the process of understanding additive manufacturing materials and not so much the mechanical response of additive manufacturing.

New technological methods made use of power based manufacturing process such as, electron beam melting (EBM), select laser melting (SLM) and powder bed fusion (PBF) which melt layers of metal powder to produce a part or component from the bottom up. The direct energy deposition (DED) process feeds metal powder through wire feedstock into a melt pool to produce components. The advantage of the powder bed fusion (PBF) process is that it is able to produce more complex components shape and features than the DED additive manufacturing process (Sames, 2015). Most metal additive manufacturing has advantages over traditional machining methods; manufacture their unique geometries (freedom of design), elimination of tooling and retooling, light-weight design and elimination of production steps.

The metallurgical component manufactured from additive manufacturing is determined by a chemical reaction at a certain temperature that the material experience. The heat transfer has different application for DED and PBF for additive manufacturing; the metallurgical principle for both processes produces the same outcome.

Materials are subjected to some kind of loading and its prediction to produce reliable designs must be correct and understanding the properties with numerous metallurgical variables. According to Sames (2015), a combination of metals has been produced for commercial production using additive manufacturing, but recent efforts has made it possible for continuous development of new materials for additive manufacturing processes. This research study will

mainly focus on 3D (Three Dimensional) additive manufactured nickel-based superalloys, the effect of microstructural features on mechanical properties of Inconel 625 and 718 manufactured with 3D (Three Dimensional) additive manufacturing.

1.1 Aim and Objective

The main objective of this work is to study the various influence of microstructure on mechanical properties of 3D additive manufacturing nickel-based alloys Inconel 627 and 718, heat treatment and effect of grain size within the solid phase. The sample models with different parameters for the variation of material properties with grain size can also be determined. The grain boundary, crystal orientation, precipitates and heat treatment are only mentioned in the literature review. According Supermetal (2018), the Finite Element Analysis (FEA) program can be used to incorporate the models of material data. This process will allow for structural analysis with different zones or areas in material having different grain sizes.

Further objective behind this research is to study the microstructural features and mechanical behaviour using two different experimental surface microscopy techniques: light optical microscope (LOM) and scanning electron microscope (SEM) on 3D additive manufacturing concepts of Inconel 625 and 718 a nickel-based superalloys.

1.2 Background and Research

The scientific and industrial application of alloy and metal is determined by its properties. To achieve the microstructure and mechanical behaviour of SLM 3D additive manufactured Inconel 625 and 718 sample specimens, the following will be considered:

- The study and analysis of the mechanical behaviour which will enable the researcher to generalise various conclusion regarding the mechanisms behind the strengthening in metals due to grain size refinement.
- The mechanical behaviour of Inconel 625 and 718, the bending strength, microstructure, and particularly the hardness with respect to grain size.
- (X-ray diffraction) XRD analysis, used to determine the crystal structure and micro elements of materials.
- Energy dispersive X-ray (EDX) analysis to quantify the chemical composition of Inconel 625 and 718 samples specimens.

1.3 Structure of Paper

Chapter 2

This chapter discusses fundamentals of nickel-based superalloys and methodology of additive manufacturing.

Chapter 3

Heat treatment process for Inconel nickel-based superalloys wrought, cast and additive manufactured are considered.

Chapter 4

Chapter four considers mechanical properties and concept of mechanical deformation elastic and plastic deformation and the relationship between processing, microstructure, grain size and mechanical properties of additive manufactured materials. The Influence of grain size and deformation effect on ultimate strength and hardness are also considered.

Chapter 5

This chapter details experimental work on 3D additive manufactured Inconel samples to determine microstructure and mechanical properties.

Chapter 6

Chapter 6 discusses the results obtained from the experimental techniques explained in chapter 5.

Chapter 7

The final chapter sums up this study and suggests possible future research.

CHAPTER 2

2.0 Fundamentals of Nickel-Based Superalloys

According to Zhang and Zhao (2012), nickel-based superalloys are the strongest group superalloys in both strength and temperature capability. The key factor of nickel-based alloys strength can be explained with precipitation hardening. The most useful process at high temperatures is precipitation hardening. This benefits nickel-based superalloys, (γ')gamma prime phase which will be discussed with regards to major phases of phase transformation. The evolution of nickel-based superalloys goes back to solution strengthening the Ni-Cr (nickel chromium) phase illustrated in Figure 2.1, Chromium (Cr) is soluble around 35% and Nickel (Ni) alloys are generally used as resistance wire (Nash, 1992). The 80-20% Ni-Cr (with proper chemical composition will provide a balance between strength, oxidation resistance and ductility (Zhang and Zhao 2012). Nickel-based superalloys such as Inconel 600, 601 and 625 evolved from Ni-Cr alloys and many alloying elements have been added to these superalloys over time in order to improve different properties (Zhang and Zhao 2012). Nickel-based superalloys can be subdivided into three categories, mainly solid solution, precipitation hardened and oxide dispersion strengthening during heat treatment process (Deng, 2018).

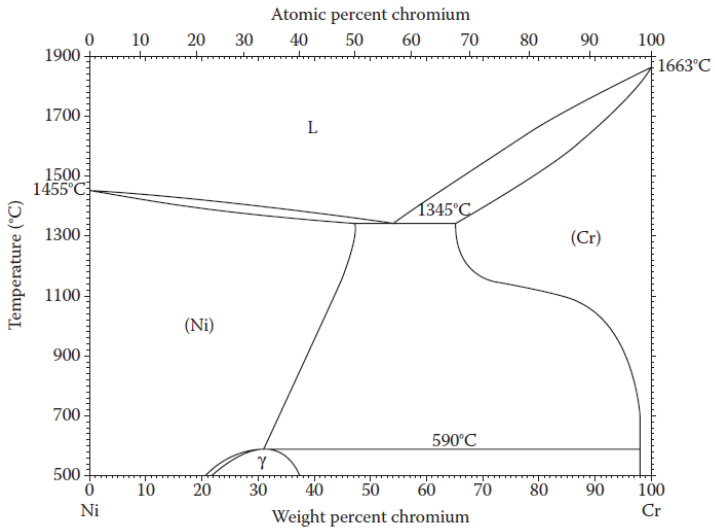

Figure 2.1: Nickel chromium binary phase diagram (Reed, 2008)

According Zhang and Zhao (2012), the main resistance in superalloy are creep, fatigue and corrosion, resistance against these damage mechanisms depends on alloying chemistry, microstructural design, heat treatment history and production technique. The resistances mentioned above affect the alloys strengths mostly negatively and therefore balance between application conditions and properties is required (Reed, 2008). The main strength-limiting

factor of a superalloy are melting and dissolution of the different phases under operation or service temperature.

2.1 Application of Additive Manufactured Nickel based Superalloys

Superalloys are high temperature alloys with superior properties regarding elevated temperatures and corrosion. According to Zhang and Zhao (2012), superalloys are classified into three groups or types based on their base elements: iron-based, cobalt-based and nickel-based superalloys. Alloys that preserve their chemical stability, mechanical properties, and physical appearance at very high temperatures, and in harsh corrosion environments maybe classified as superalloys. The mechanical properties of superalloys may not differ much from steel which is much cheaper and more easily produced. The production of superalloys may be very expensive but stand out from other metallic alloys with their high corrosion resistance, which makes them ideal for aviation applications (Zhang and Zhao, 2012).

According to Stoloff (1990), aviation gas turbines three-quarter of all superalloys; the reaming one-quarter is used in gas turbines, the chemical industry, medical industry, petrochemical equipment, rocket engines, nu clear reactors, submarines and various other application which operate in high temperature with chemical resistance.

The application of additive manufactured currently manufactured at minimal amounts based on mass production, may cause difficulty during manufacturing process, and expensive. Additive manufacturing will be appropriate for developing custom or complex parts for the aerospace, marine and possibly biomedical fields in near future (Kulkarni, n.d). The request for aerospace and aviation applications is minimal compared to other applications, therefore additive manufacturing is suitable for these applications and conditions (Kulkarni, n.d). The investigations and research show that the components manufactured with additive technique possess comparable and sometimes higher strength than traditionally manufactured components for the required applications.

According to Deng (2018), the microstructure of additively manufactured nickel-based superalloys Inconel 625 and 718 is dependent on specific processes with different applications such as component dimensions. This differ from traditional cast and wrought manufactured method of nickel-based superalloys. The heat treatment for additive Inconel 625 and 718 or any superalloy should be modified to suit the specific manufacturing process, as mentioned above with scanning strategy and component geometry (Kulkarni, n.d). The solidification in the additive manufacturing process occurs rapidly compared to the traditional and wrought manufacturing method, with finer grain size modified to suit a particular individual.

Inconel is used in marine application, the construction jet engines, and turbines for aerospace industry. Figures 2.2 illustrates typical application of parts manufactured from Inconel for (a) turbine blades and (b) propeller blade. Table 2.1 illustrates the properties of additive manufactured Inconel 625 and 718. Cooling technologies are used to rapidly reduce temperatures, but temperatures still easily exceed the tolerance of many metals. Inconel retains high oxidation resistance and tensile strength through rapid change in temperature which is ideal for the combustion process and cooling technologies found in the aerospace industry (Wikispace, 2018).

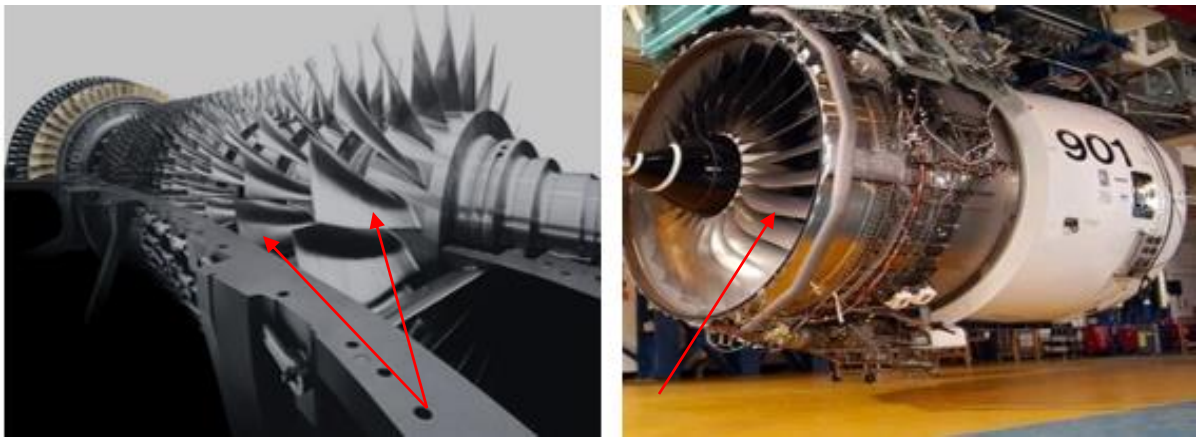

(a)Turbine blades (b) Propeller blade

Figure 2.2: Application of additive manufactured nickel-based superalloys denoted with arrows (pinerest 2018; wikispaces, 2018)

Table 2.1: Properties of Additive manufactured Inconel 625 and 718 at room temperature 20 ^{0}C (Americanelements, 2018)

Properties	Inconel powder 625	Inconel powder 718
Appearance	Metallic	Grey
Density	8.44 g/cm^3	8.19 g/cm^3
Tensile strength	827-1024 MPa	887-1003 MPa
Melting Point	1290 ^{0}C -1350 ^{0}C	1260 ^{0}C -1336 ^{0}C
Modulus of rigidity	79 kN/mm^2	77.2 kN/mm^2
Modulus of elasticity	205.8 kN/mm^2	204.9 kN/mm^2

2.2 SLM (Selective Laser Melting) Additive manufacturing process

In this section a brief introduction will describe the additive manufactured methods; SLM (selective laser melting) was used to manufacture the Inconel 625 and 718 sample specimens. In addition, the SLS (selective laser sintering) and DMLS (direct metal laser sintering) methods will be briefly mentioned. Furthermore these three additive manufacturing methods follow the same manufacturing process procedure as illustrated in Figure 2.3 (a) powder laser beam process and (b) powder bed parameter (Deng, 2018).

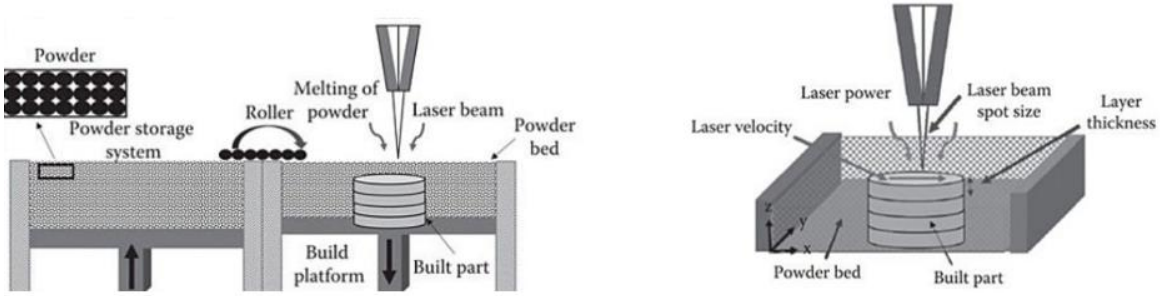

(a) Powder laser beam process (b) Powder bed parameter

Figure 2.3: Additive manufacturing process for SLM (Selective Laser Melting) (Badiru et al., 2017)

According to AZO Materials (2018), SLM and DMLS technologies are quite similar. Both involve the use of a laser for scanning and selectively fusing or melting the metal powder particles. The main difference between SLM and DMLS boils down to the basics of the particle bonding process in manufacturing stage. In SLM the metal powders are fully melted in a single process. In the process of DMLS powder is formed with different melting points that fuse on a molecular level at higher temperatures (AZO Materials; Deng, 2018). The SLS is a compacting and forming process, rather than one melt the powder to liquid form. SLS can be applied to different materials like plastics, polymers and metals.

There are still many technical challenges when it comes 3D additive manufacturing to overcome before this process can be fully taken advantage of. Further work is required to understand solidification metallurgy, material development, process parameter and support structure design of 3D additive manufacturing.

2.3 Powder Characteristics for Additive manufacturing

According to Reed (2008), power metallurgy techniques have been widely applied to the superalloys since the early 1970s. The investment needed for cast or traditional section cast method for manufacturing superalloys is not efficient and may obtain refined chemically, homogenize of final structure in massive parts. Furthermore, powder metallurgy production allows superalloys to contain higher amount of alloying elements and display high temperature capability (Zhang and Zhao, 2012). Powder metallurgy produces fine microstructures homogeneous with uniform phase distribution, less segregation and microstructure greatly increases workability of part or components manufactured by this method (Tien and Caulfield, 1989). In addition, the powder metallurgy process has a degree of freedom which allows the custom of characteristics, properties and performance requirements illustrated in Figure 2.4 (Zhang and Zhao, 2012).

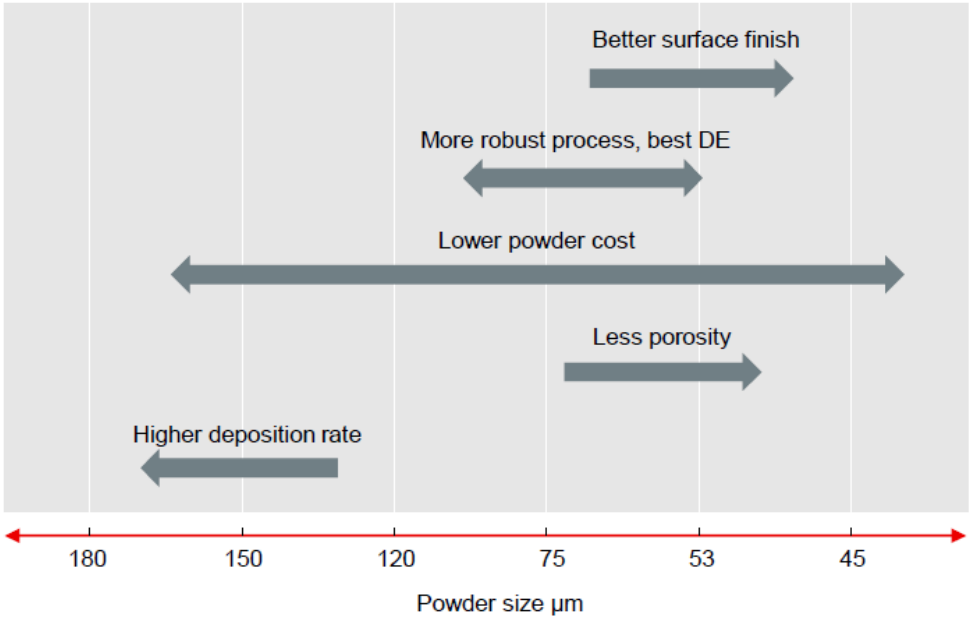

Figure 2.4: Powder size effect denoted with arrow directions (Oerikon, n.d)

The characteristics such as particle size, morphology, distribution, followability, bulk properties and porosity are all important to assess in order to produce a superalloy powder for additive manufacturing (Markusson, 2017). The evenly spreading of powder deposition during the additive manufacturing process is crucial to deposit uniform layers. The correlation between impact factors on additive manufacturing is not simple or easy as there are numerous interactive effects based on characterisation parameters, as illustrated in Figure 2.5 (Benson and Snyder, 2015).

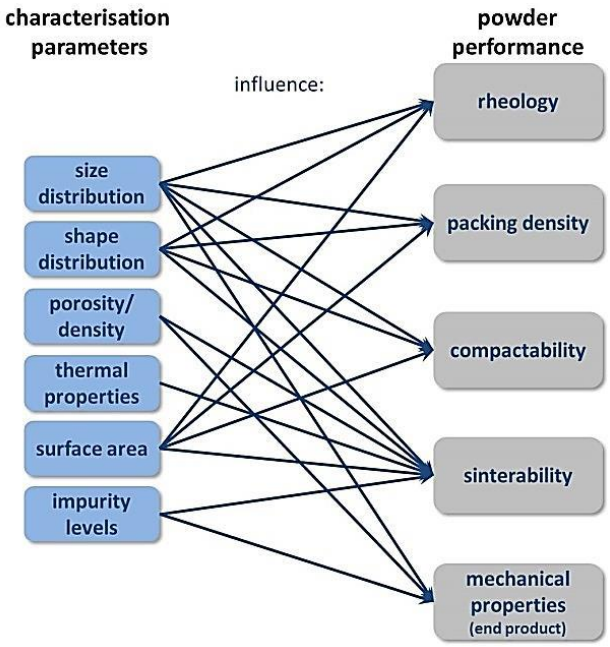

Figure 2.5: The correlation between the factors and their impact on the additive manufacturing processes (Benson and Snyder, 2015)

The final properties of powder metallurgy superalloys depend on alloy composition, powder particle size, consolidation processing, degree of defect free structure and heat treatment (Markusson, 2017). According to Zhang and Zhao (2012), powder metallurgy superalloy microstructure has more uniform and finer grain size than wrought and cast alloys. Powder metallurgy superalloys exhibit better ductility and tensile strength due to finer grain size (Zhang and Zhao, 2012).

2.4 Common defects during additive manufacturing process

According to Deng (2018) the most common defects when it comes to additive manufacturing components or parts are crack, porosity and residual stress, illustrated in Figure 2.6: (a) residual stress, (b) cracking and (c) porosity morphologies. The major or most common defect during additive manufacturing process is residual stress because of stability for geometric accuracy. The surface roughness for laser melting is slightly higher than cast or wrought machined but better than electron beam melting due to less laser beam focus and particle powder size during manufacturing process. The surface roughness won't be discussed as one of the defects.

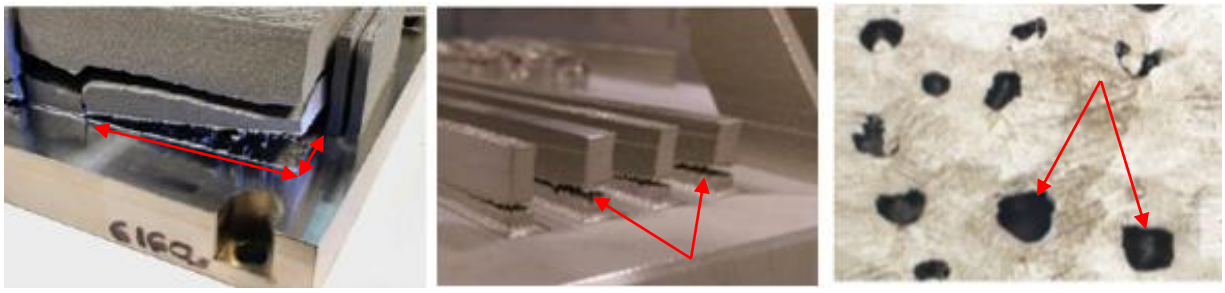

(a) Residual Stress (b) Cracking (c) Porosity morphologies

Figure 2.6: Common defect during additive manufacturing process denoted with arrows (Kasperovich et al., 2016; Molitch-Hou, 2017)

2.4.1 Residual Stress

Accourding to Mercelis and Kruth (2006), residual stress is an internal stress locked within a material that continuous after the removal of an applied stress. The root cause of residual stress in additive manufacturing process is the non-uniform temperature gradient in the heat or thermal zone during melting which may have a negative effect on mechanical properties. This acts as a main driver of focus change in grain structure (Deng, 2018; Sames, 2015). Furthermore, the impact of residual might lead to crack formation which may disconnect the component or part from the building parts or lead to geometrical distortions.

According to Moletsane (2016), residual stress can be defined as macro-residual stresses, also referred at type I, that exist in a component or part larger than the grain size of the material. Micro-residual stresses which may occur with different results in microstructure of a material will be classified as type II or III as illustrated in Figure 2.7. Type II Micro-residual stresses develop at the grain size level while type III are generated at the atomic level (Moletsane, 2016; Paranjpe, 2014). The ways to reduce magnitude of residual stress is process dependent; the residual stress may influence recrystallization.

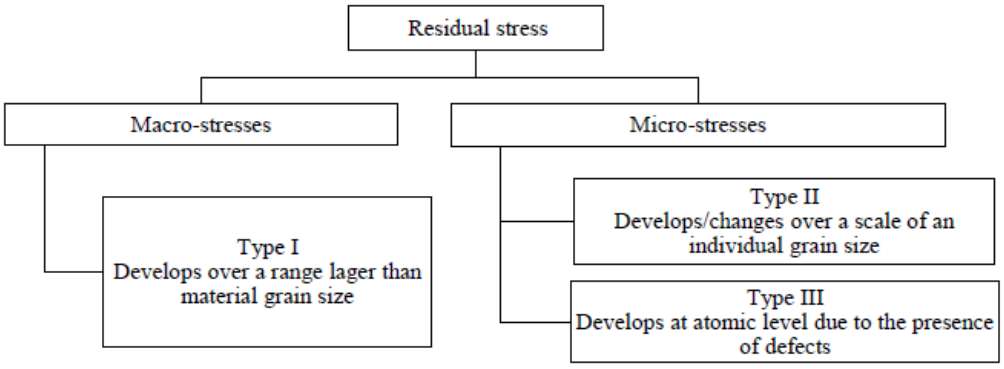

Figure 2.7: Classification of residual stresses (Paranjpe, 2014)

2.4.2 Cracking

Cracking during the additive manufacturing process mostly occur due to relatively high residual stress as mentioned above; when cracks form or expand residual stress will be released (Deng, 2018). Cracking may be caused by the powder not melting during manufacturing process, insufficient layers thickness during melting process, the energy source being too strong or stress may occur during the solidification process illustrated in Figure 2.6 (Molitch-Hou, 2017). According to Song et al. (2015), segregation of chemical elements Nb and Mo at grain boundaries will increase the forming of low melting point and might complicate thermal condition which form cracks at the grain boundaries.

2.4.3 Porosity

Spherical and irregular porosity, illustrated in Figure 2.8, are mostly found in the additive manufacturing process: it is caused by the spherical pores where inert gas is involved during melting pool stage and gas trapped inside the powder which has not escaped from the melting pool. (Song et al., 2015; Deng, 2018). The spherical pores cause less damage to mechanical properties of components being manufactured, but irregular pores raise the concentration of stress and may lead to failure (Deng, 2018). According to Molitch-Hou (2017), pores may occur when powder particles are loosely packed or there is incorrect layer thickness, or melted metal powder don't flow in the desired region.

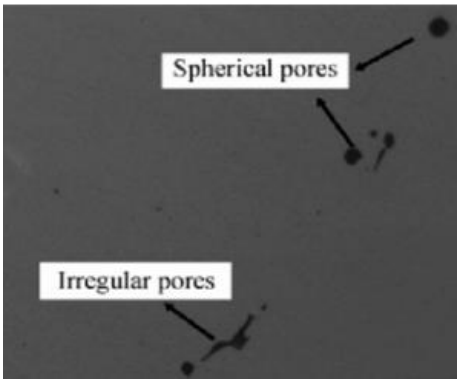

Figure 2.8: Spherical and irregular porosity denoted with arrows (Neghlani, 2016)

2.5 Chemical and common physical properties of Inconel 625 and 718

The chemical properties of Inconel 625 and 718 can be measured or physically observed without any composition changes of any sort. The physical properties used to observe and describe matters may include appearance, colour, boiling point, melting point, density or other properties. Inconel powders 625 and 718 may physically look the same in appearance as powder. In additive manufacturing process a chemical reaction takes place during this process by which, solid form Inconel 625 and 718 was manufactured as illustrated in Figure 2.9. The properties would be different after manufacturing in terms of melting point, tensile strength, hardness and density.

Figure 2.9: 3D additive manufacturing Inconel 625 and 718 sample specimens

Table 2.2: The element composition with percentages in weight rage and limits of Inconel 625 (ASTM International, 2014)

Nickel (58% min)	Chromium (20-23%)	Iron (5%max)
Molybdenum (8-10%)	Copper (0.5% max)	Aluminium (0.4% max)
Niobium (3.2-4.1%)	Silicon (0.5 max)	Carbon (0.10 max)
Sulphur (0.015% max)	Manganese (0.5% max)	Phosphorus (0.02% max)
Titanium (0.4 max)		

Table 2.3: The element composition with percentages in weight rage and limits of Inconel 718 (ASTM International, 2014)

Nickel (50-55%)	Chromium (17-21%),	Iron (24%max)
Molybdenum (2.8-3.3%),	Copper (0.3% max)	Aluminium (0.2-0.8%)
Niobium (4.8-5.5%)	Silicon (0.5 max)	Carbon (0.08% max)
Sulphur(0.015% max)	Manganese(0.3% max)	Phosphorus (0.0015%max)
Titanium (0.7-1.1 max)	Boron (0.006% max)	

As seen in Table 2.3, the range limit of Inconel 718 is less especially for elemental phosphorus, and Inconel 625 has no prescribed boron. According to Nakki (2018), Inconel 718 also has a range limit for Aluminium (Al) and Titanium (Ti), meaning both as lower and upper limits, but the element content range of Inconel 625 can be anywhere between 0 and 0.4%. The recent growth in the field of additive manufactured has had an effect and powder manufacturing companies has introduced their own range limits of powders for additive manufactured (Nakki 2018). Additive manufacturing powder companies like H.C. Starck and Praxair Technology recently introduced Inconel 625 powder with an upper limit of 0.0010% for boron with the remaining elements remaining the same (see Table 2.2) for the American Society for Testing and Materials (ASTM) F3065 – 14E1 (Standard Specification for Additive Manufacturing Nickel Alloy (UNS N06625) with Powder Bed Fusion).

2.6 The Microstructure of Materials

The term microstructure refers in general to grains of materials, the shape and sizes of micro-constituents and their arrangements or morphology and distribution in the structure which are usually indiscernible to the naked eye. The microstructure of an alloy depends on such variables as what the alloying elements present, which is the temperature at heating and cooling rate related to average room temperature. According to Callister and Rethwisch (2013), the mechanical properties of any alloy will change when altering the size, shape and distributions of its various micro-constituents. The sample surface must always be clean and polished, resulting in a smooth mirror finish. This process is possible with a chemical reagent, that should be applied to the surface to reveal the grain boundaries. In addition, in Figure 2.10 typical microstructure of Inconel 625 samples manufactured with (a) wrought and (b) additive manufactured. Figure 2.11 shows typical microstructure of Inconel 718 samples manufactured with (a) casting, (b) wrought and (c) additive manufactured at room temperature 20 ^{0}C .

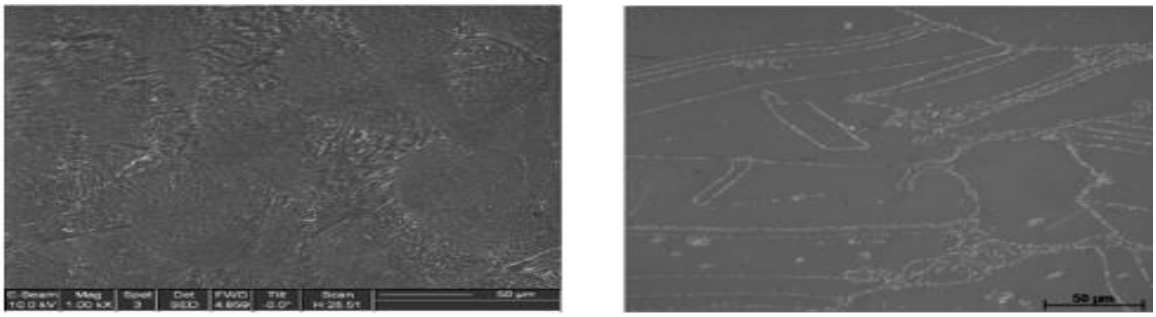

(a) Wrought (b) Additive

Figure 2.10: Microstructure of Inconel 625 samples (Brand, 2016)

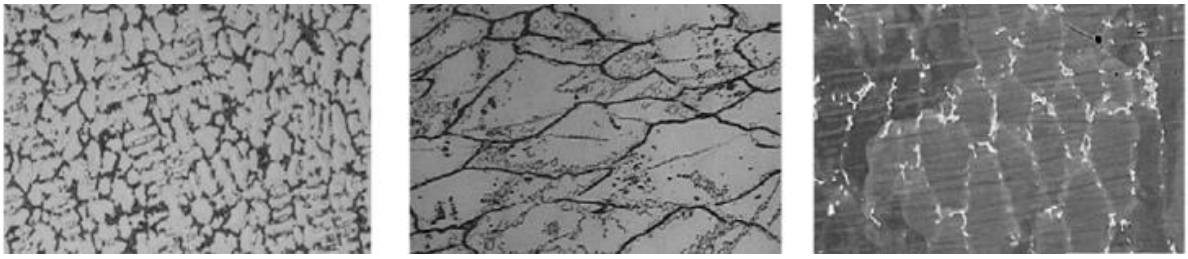

(a) Casting (b) Wrought (c) Additive

Figure 2.11: Microstructure of Inconel 718 samples (Neghlani, 2016)

The different resolutions for microscopy methods and measurements are illustrated in Figure 2.12. Firstly seen with the naked eye; secondly light optical microscope which is made possible with visible light and lenses to magnify images based on the size. There are two types of electron microscopes, the transmission electron microscope (TEM) and scanning electron microscope (SEM) methods. In the SEM method, electron beam scans the sample surface. During this process an image is created form back scatter electrons. In the TEM method an imaged is formed from an electron beam that is scattered while passing through the specimen. The electron microscope method generates a three-dimensional image of the specimen surface.

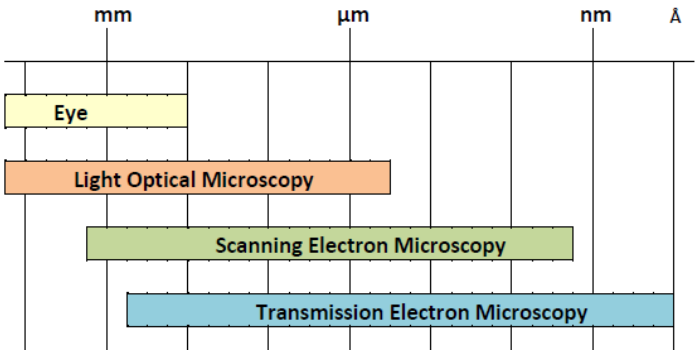

Figure 2.12: Comparison of resolution for different microscopy methods (Brandtberg, 2017)

2.6.1 The Crystal Structure of Metals

Metals today are used for a wide range of applications that have different properties which are useful in different areas in the engineering field (Lundberg and Eliasson, 2015). Mechanical properties of metals include thermal, electric conductivity, high melting point, strength, toughness and ductility. The large metallic bond between atoms in most solid metals typically results in a crystalline structure, which means that atoms within certain materials are situated in a repeating array over a long range the description or arrangement of crystalline structure illustrated in Figure 2.13. (Green, 2013).

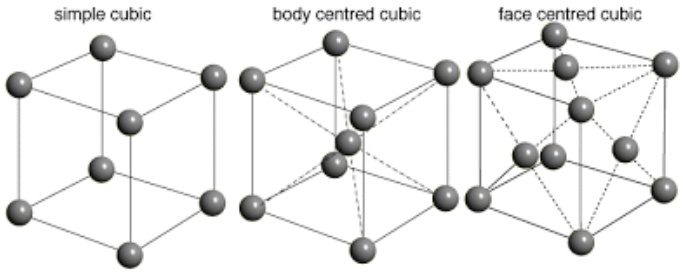

Figure 2.13: Arrangements of atoms (Green, 2013)

The crystal structure of metals formation form a melt start with small regions called nucleation stage 1 (small crystallite nuclei) illustrated in Figure 2.14 as a result of atoms rearrangement. In nucleation, also known as seed, the crystallization (grains) will grow in all directions to stages 2 (growth of the crystallites and the obstruction of some grains) and 3 (upon completion of solidification grain with irregular shapes formed) (Callister and Rethwisch, 2007). The final stage 4 is polycrystalline structure, whereby the grain is limited by another grain, creating a boundary between them.

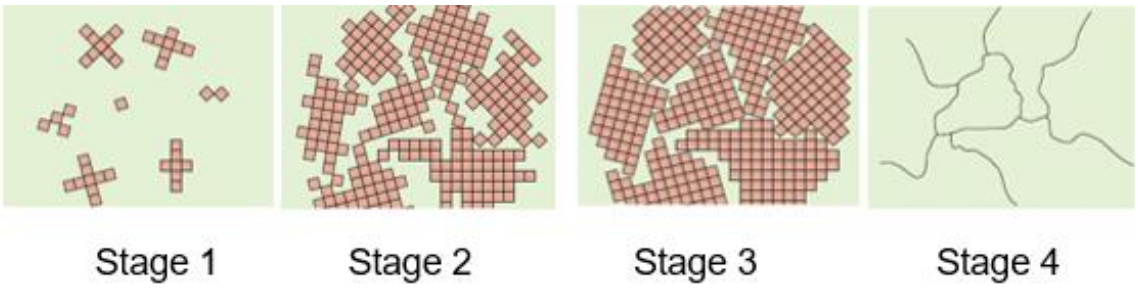

Figure 2.14: Solidification in metals (Carrazana, 2018)

2.6.2 The Grain Size

According to Nayar (2005), the grain size, and grain direction will affect mechanical properties during the manufacturing process. The grain or particle refinement is a technique used to improve a materials wear resistance and strength. The crystal is referred to as a grain in materials used in the engineering field and the common boundary formed between grains is called a grain boundary. When a new grain is nucleated in heat treatment process, the atoms in each grain growth are arranged in a specific pattern. This specific pattern will depend upon the crystal structure of the metal or alloy (Seifert, 2003). The grain structure and grain stability will be controlled with the amount of space filled and minimal interfacial energy (Nayar, 2005).

Most crystalline solids are formed of a collection of smaller crystal or grains, materials labelled as polycrystalline. Various polycrystalline materials can be characterised by specific microstructures and their features (Callister and Rethwisch, 2007). It is predicted that

microstructures transformation resulting from stresses and strain during heat treatment will change the mechanical properties. According to Reed (2008), the phase transformation of materials is one of the challenges of modelling of heat treatment.

2.6.3 Principle Metallic Crystal Structures

The most common type of cubic structure is not simple crystal structure with an atom in each. According to Green (2013), the body centred structure (BCC) and the face centred structure (FFC) are more common. In BBC there are atoms in the centre of the cube which is typically stronger while the FCC has the atoms on the face of the cube which means the atoms can slide easy over each other making the properties of the material ductile. In BBC in some metals will only occur when the metal is softened as the temperature rises closer to the metals melting point (Green, 2013). Figure 2.15 illustrates the variation of melting temperature of the elements with atomic number; the melting of each chemical element has a correlation with the atomic number.

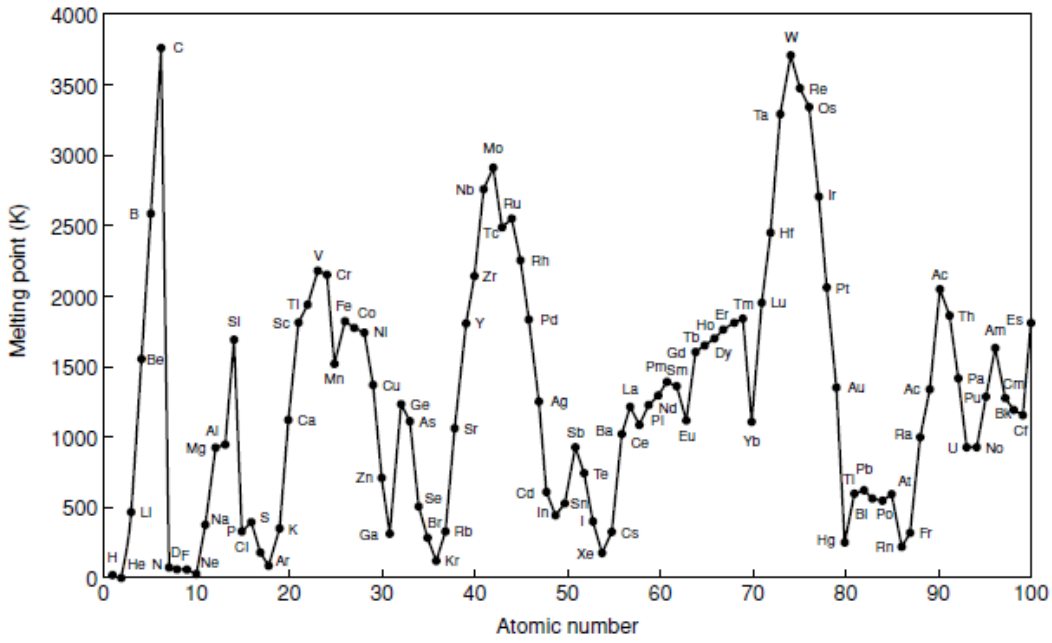

Figure 2.15: Variation of the melting temperature of the elements with atomic number (Reed, 2008)

According to Zaidi (2018), the principle metallic crystal structures for most metals crystalize; atoms closer together bond match more tightly to each other and release energy because of their densely packed structures This lead to lower and more stable energy arrangements. The periodic table in Figure 2.16 illustrates the 4 common phases and the chemical elements in their different phases. Yellow marking indicates simple phase, green BCC, blue FCC and red HCP (Hexagonal Close Packed).

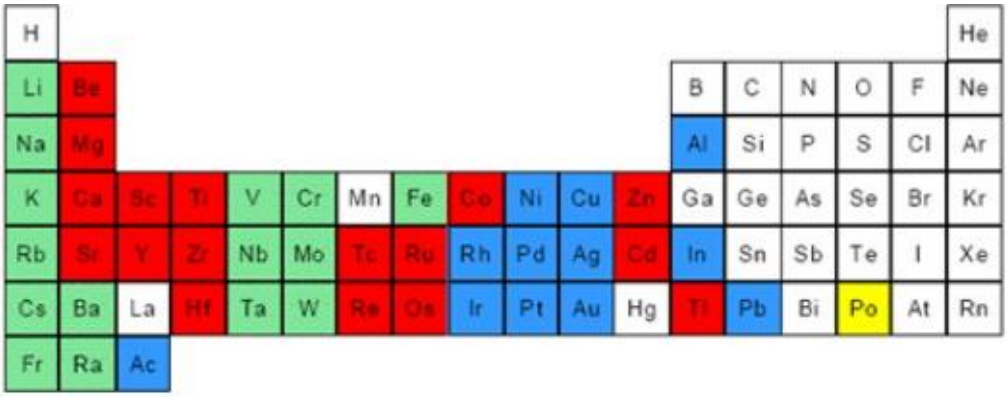

Figure 2.16: Periodic table with chemical elements (Zaidi, 2018)

2.6.3.1 BCC (Body Centred Cubic)

According to Smith and Hashemi (2010), crystal structure at room temperature $20^{0}C$ occurs in most metals such as Cr, (chromium) , Fe (iron), Mo (molybdenum), tungsten (W) and vanadium (V). BCC crystal structure is not 100% closed packed since the atoms could be package closer together. BBC occupies a packing factor of 68% of the atoms and 32% remains as empty space per unit cell illustrated in Figure 2.17, iron may have less than the maximum package factor per unit atom cell.

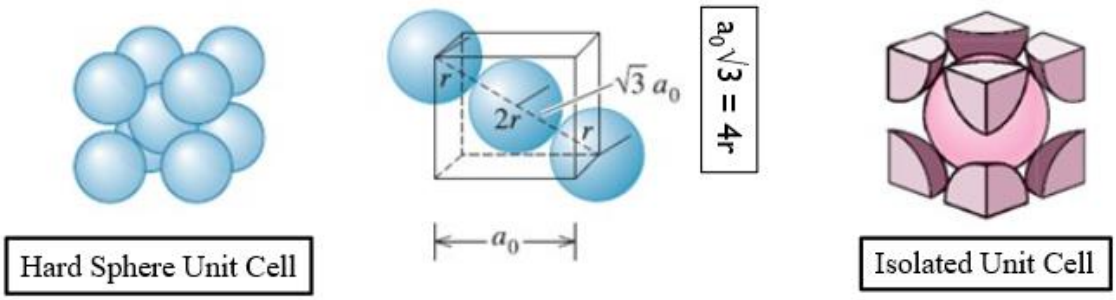

Figure 2.17: BBC (body centred cubic) (Zaidi, 2018)

Table 2.4: Selected Metals that have BCC (body centred cubic) crystal structure at room temperature 20^0C (Adapted from Jee, 2011)

Metals	Lattice constant a (nm)	Atomic radius R (nm)
Cr (Chromium)	0.289	0.125
Fe (Iron)	0.287	0.124
Mo (Molybdenum)	0.315	0.136
K (Potassium)	0.533	0.231
Na (Sodium)	0.429	0.186
Ta (Tantalum)	0.330	0.143
W (Tungsten)	0.136	0.137
V (Vanadium)	0.304	0.132

2.6.3.2 FCC (Face Centred Cubic)

According to Zaidi (2018), metals such as Al (aluminium), Cu (copper) lead, Ni (nickel) and Fe (iron) at temperatures ranges between 910 ^0C and 1394 ^0C crystallize with the FCC (crystal structure. FCC occupies a packing factor of 74% of the atoms and 26% remains as empty space per unit cell, illustrated in Figure 2.18.

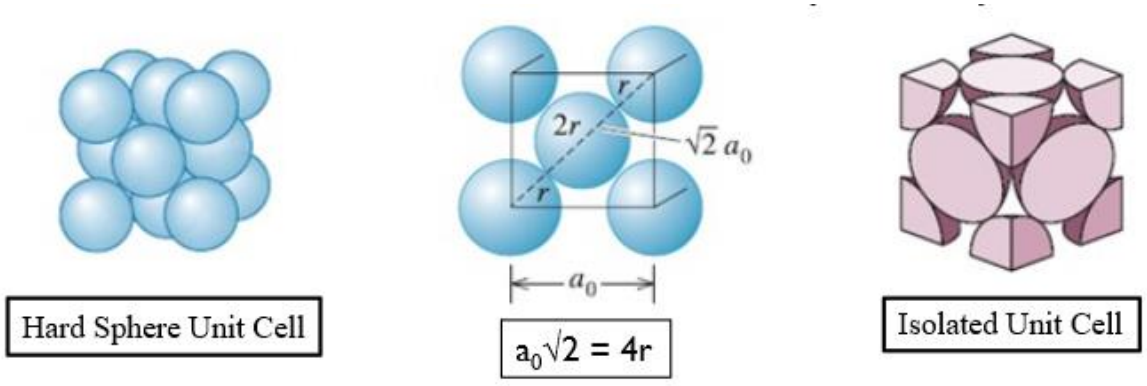

Figure 2.18. FCC (face centred cubic) (Zaidi, 2018)

Table 2.5: Selected Metals that have FCC (face centred cubic) crystal structure at room temperature 20^0C (Adapted from Jee, 2011)

Metals	Lattice constant a (nm)	Atomic radius R (nm)
Al (Aluminium)	0.405	0.143
Cu (Copper)	0.3615	0.128
Au (Gold)	0.408	0.144
Pb (Lead)	0.495	0.175
Ni (Nickel)	0.352	0.125
Pt (Platinum)	0.393	0.139
Ag (Silver)	0.409	0.144

The FCC phase constitutes as the matrix phase for super-alloys; its stability is measured with respect to the crystal structure parameters. The matrix phase during transformation is significantly influential based on thermal cycling or during periods of operation. The driving force which can be estimated for the change of pure Ni to a crystal structure aside from the FCC form will depend on Ni-Cr binary phase diagram as mentioned above in 2.0 fundamentals of nickel-based superalloys.

2.6.3.3 HCP (Hexagonal Closed Packed)

According to Callister and Rethwisch (2017), with regard to HCP (hexagonal closed packed) structure, not all structures are cells with cubic symmetry such as FCC and BCC. HCP) crystal structure has the same packing factor as FCC: 74% of both structures are closely packed, as illustrated in Figure 2.19.

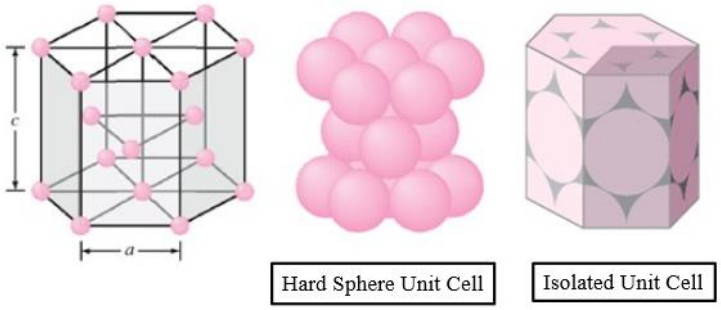

Figure 2.19: HCP (hexagonal closed packed) (Callister and Rethwisch, 2017)

Table 2.6: Selected Metals that have HCP (hexagonal closed packed) crystal structure at room temperature 20^0C (Adapted from Jee, 2011)

Metals	Lattice constant(nm)		Atomic radius R (nm)	c/a ratio	% deviation from ideality
	a	c			
Cd(Cadmium)	0.2973	0.5168	0.149	1.890	+15.7
Zn(Zinc)	0.2665	0.4947	0.133	1.856	+13.6
Ideal HCP	-	-	-	1.633	0
Mg(Magnesium)	0.3209	05209	0.160	1.623	-0.66
Co(Cobalt)	0.2507	0.4069	0.125	1.623	-0.66
Zr(Zirconium)	0.3231	0.5148	0.160	1.593	-0.2.45
Ti(Titanium)	0.2950	0.4683	0.147	1.587	-2.81
Be(Beryllium)	0.2286	0.3584	0.113	1.568	-3.98

2.7 X-Ray Emission

X-ray analysis is a test method used to analyse structure and element information of materials; Figure 2.20 illustrates electron interaction and X-ray emission. According to Petersen-Olverleir (2015), the secondary electrons forms from inelastic collisions: backscattered electrons are a result of changes in their direction which determine the X-ray emission characteristics. The X-ray techniques analyse the crystal structure and identify the crystalline phases in a particular place in a material, also known as electron backscatter diffraction (EBSD) and determine chemical composition information known as energy dispersive X-ray (EDX) (Elements, 2019).

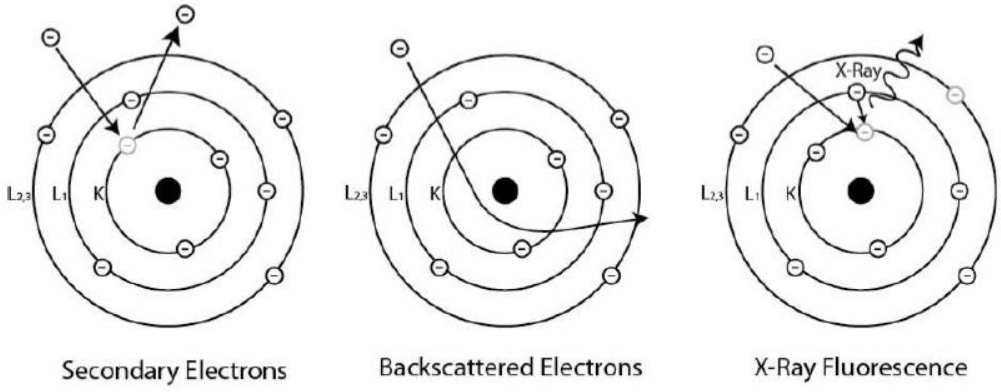

Figure 2.20: Electron interactions and x-ray emission (Ualberta, 2015)

According to Petersen-Overleir (2015), Braggs diffraction occurs when radiation of a wavelength similar to atomic spacing which is scattered by atoms of crystalline systems and results in constructive and destructive interference illustrated, in Figure 2.21. Bragg diffraction analysis is determined and based on the resulting wave interference pattern of crystallographic planes in the crystal lattice.

Bragg's Law

$$n\lambda = 2d\sin\theta \qquad (1)$$

n = order of diffraction , λ = incident wavelength, d = interplanar distance between atoms inside the material, θ = scattered angle

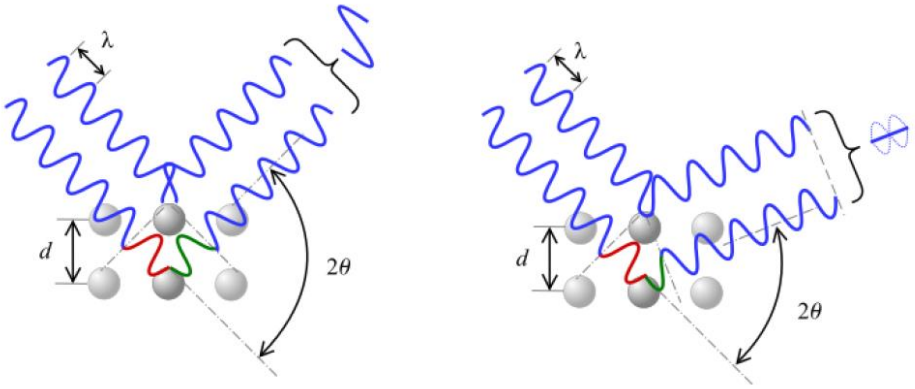

Figure 2.21: Constructive and destructive interference caused by 2θ deviation

(Wikipedia, 2019)

2.7.1 EBSD (Electron Backscatter Diffraction)

According to Stojakovic (2012), microstructural information of crystals orientation, grain orientation, grain boundaries, phase identification and internal stress of crystal regions are quantitatively determined EBSD. The polished sample specimen is mounted at an angle of 20^{0} to the incident electron beam; the back scattered electron cone will reflect the diffraction pattern on the camera screen, as illustrated in Figure 2.22.

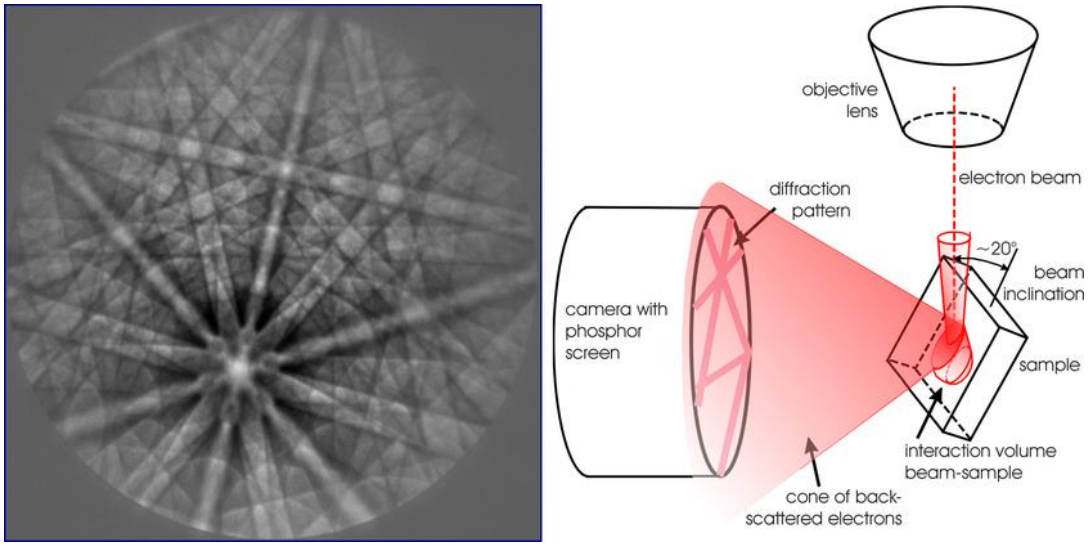

Figure 2.22: EBSD (Electron Backscatter Diffraction) analysis with diffraction pattern (Max Planck Institute, 2003)

2.7.2 EDX (Energy Dispersive X-ray)

EDX (energy dispersive X-ray) analysis works as an integrated feature of SEM. The EDX (Energy Dispersive X-Ray) spectrometer determines the chemical composition in term of percentage by analysing the characteristics of the X-rays. The primary X-rays during EDX are generated form SEM with a modified X-ray beam directed on to the sample specimen's surface. XRF (X-Ray Fluorescence) is the method used to obtain non-destructive element information about the sample being analysed; element information generated by software will be displayed on a computer connected to SEM, as illustrated in Figure 2.23.

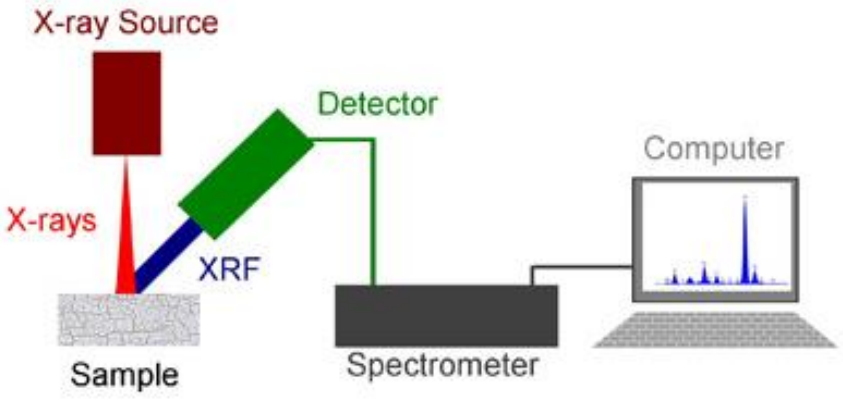

Figure 2.23: Analysis process of EDX (energy dispersive x-ray) (Horiba, 2019)

According to Prevey (1986), X-ray diffraction can also be used to determine both macroscopic and microscopic residual stresses. Marco stress occurs during X-rays diffraction when crystals and grain in materials shift position based on diffraction peak. (Prevey and Young, 1987). Micro stresses in materials are caused by difference in microstructures and are comparable to the grain size and direction in materials.

2.8 Phase Transformation

According to Lundberg and Eliasson (2015), phase transformation is a change from one phase to another phase at a certain time and temperature. During these transformations, characteristics also change. Furthermore, development of microstructure in alloys involves phase transformation, which needs time and cooling rate to diffuse. This process by which Ni (nickel) and Cr (chromium) changes from one atomic arrangement to another when heated to a certain temperature below melting point is illustrated above in Figure 2.1. Phase transformation as well as transformation rate are important to develop a specific microstructure which in turn affects the mechanical properties of a material.

2.8.1 Composition microstructure relationship in Nickel Superalloys of different phases

The major phases present in additive manufactured Inconel 625 and 781 nickel-based superalloys are the following

- Gamma phase (γ)
- Gamma prime phase (γ')
- Carbides and borides phase
- Topologically Closed Packed phases

2.8.1.1 The gamma phase (γ)

This phase includes elements nickel, cobalt, iron, chromium, ruthenium, molybdenum, rhenium and tungsten which tend to partition to nickel based austenitic gamma γ phase. This exhibits the FCC and in most cases it forms a continuous matrix phase. This process has slow diffusion of some elements and alloy exhibits resistance to high temperature creep (Reed, 2008).

2.8.1.2 The gamma prime phase (γ')

The second group of elements include aluminium, Titanium, niobium and tantalum atomic radii and this development of direct phases is often consistent with γ matrix accompanied with elements such as, Ni_3 (aluminium, tantalum and titanium) known as gamma prime phase γ' or precipitate phase, . The γ' is steady at temperatures up to 1373 K, consistence with ductility with matrix as illustrate in Figure 2.24 Ni Al (nickel aluminium) binary phase for wrought and additive manufactured (Zhang and Zhao 2012). According to Carter (2013), the composition denoted with 'x' indicate the area where a particular nickel-based superalloy may form or exist during binary the phase illustrated in Figure 2.24.

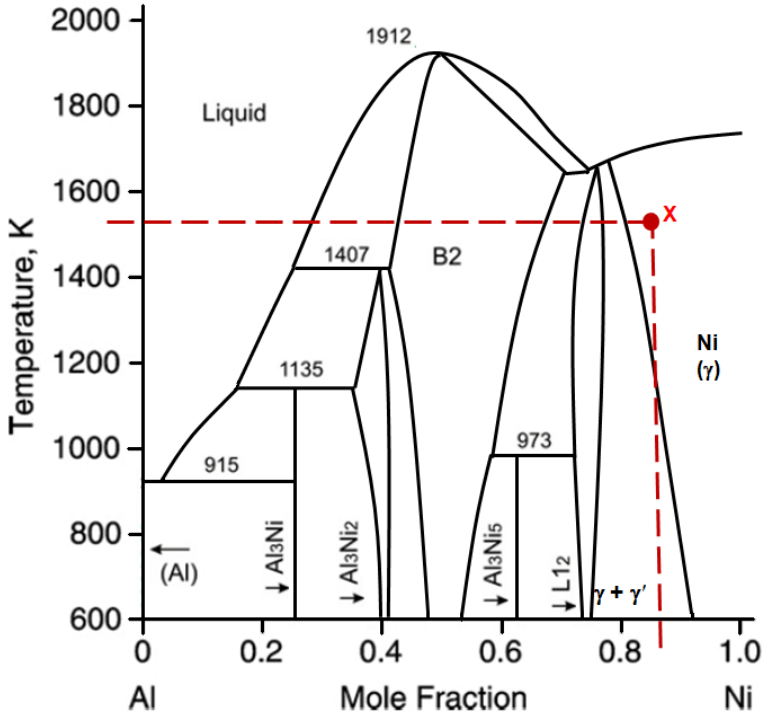

Figure 2.24: Ni-Al (Nickel-Aluminium) phase diagram adapted from Chen et al., (2010)

The γ' and γ'' phases are exit phases, and the γ'' phase is presented as the major strengthening agent at average temperature after heat treatment process (Zhang and Zhao 2012). The phase γ'' occurs only in Ni superalloys with Nb elements, like Inconel 718 illustrated in Figure 2.25 (Glade, 2007). Nickel alloys in γ'' phases have good creep properties and high tensile strength at relatively low temperature. According to Sundararajan et al. (1997) , in the transformation process from γ'' to γ' at temperatures from 650^0C to 675^0C, a significant reduction in strength exits takes place. The γ' phase is ductile which improves material strength without effecting toughness in nickel-based superalloys.

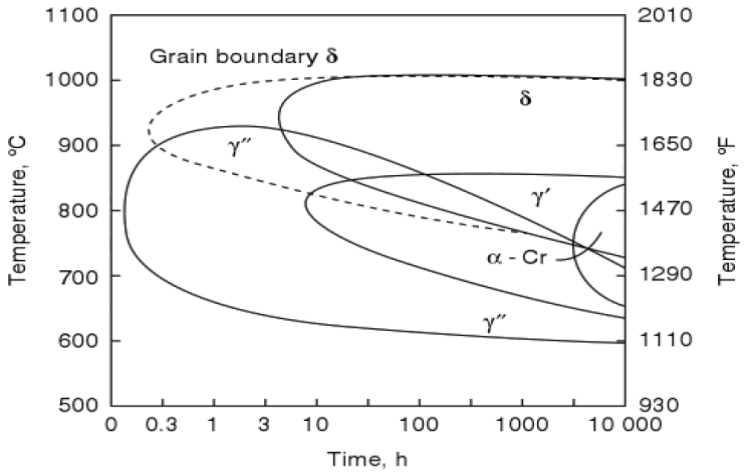

Figure 2.25: An approximate TTT (Time Temperature Transformation) Inconel 718 (Oien, 2014)

2.8.1.3 The Carbides and borides phase

According to Gouge and Michaleris (2018), the carbides and borides process C often exists at concentration up to 0.2 weight percentage which combines with reactive elements such as Ti (titanium), Ta (tantalum) and Hf (hafnium) to form MC carbides. This process decompose to other species, such as $M_{23}C_6$ and M_6C which tend to stay in the γ grain boundaries, which may be rich in Cr, Mo and W. The M elements in $M_{23}C_6$ are Cr, Fe, W and Mo (Molybdenum); the M elements in M_6C are Mo, W, Cr, Co and Ta. When $M_{23}C_6$ is combined in grain boundaries, element Cr state in the matrix become less, and solubility for γ' will increase in that phase (Reed, 2008).

The dominating formulas for formation of $M_{23}C_6$ and M_6C carbides are as follows:

$$MC + \gamma \rightarrow M_6C + \gamma' \quad (1)$$

$$MC + \gamma \rightarrow M_{23}C_6 + \gamma' \quad (2)$$

$$M_6C + M' \rightarrow M_{23}C_6 + M'' \quad (3)$$

During these formations with Cr, Ni or Mo, elements can be used as substitute for M′ and M″; these carbides have free crystals and during this process the rupture may increase as temperature increases.

2.8.1.4 The Topologically closed packed phases

According to Reed (2008), other phases can be found in certain superalloys like Inconel 625 specifically in aged condition for TCP phases σ, μ and Laves illustrated in Figure 2.26 TTT (Time Temperature Transformation) of Inconel 625. The most violable elements for TCP are Ta, Nb, W or Mo. TCP are typically unwanted brittle phases which are formed at a particular temperature during heat treatment (Gouge and Michaleris, 2018).

The creep strength will reduce during this process and simply display as crack initiation due to their brittle features (Glade, 2007). The characteristic of topology is generated with distances caused by large interatomic one below the other.

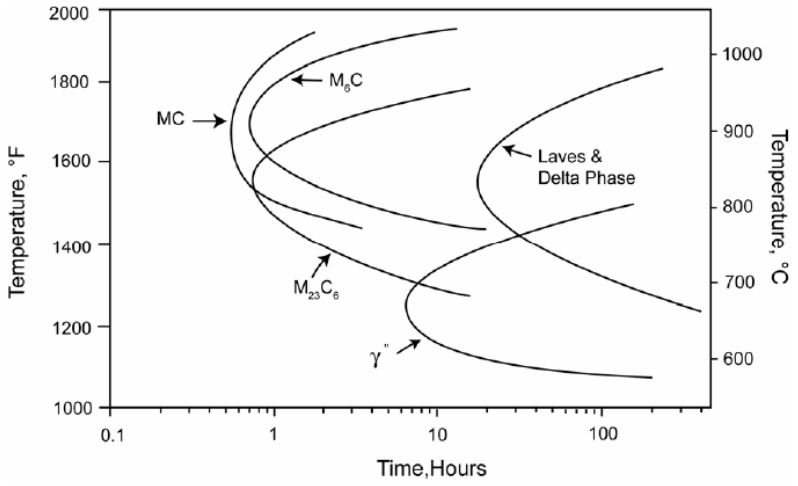

Figure 2.26: An approximate TTT (Time Temperature Transformation) Inconel 625 (Shoemaker, 2005)

According Glade (2007), the σ phase has composition type Cr (Chromium), Mo , Ni and Co which consists of 30 atoms cell and resemble carbides $M_{23}C_6$, and is in its most undesirable form. During this phase shape, hardness initiate cracking which leads to brittle failure, this phase is responsible for reducing creep rupture resistance (Reed, 2008).

The μ phase composition resemble σ phases with most of elements Mo and Co resembling carbides M_6C with 13 atoms per cell (Glade, 2007).

The Laves phases intermetallic compounds chemical composition type is AB_2 where A represent Fe and commonly Cr, Mn (Manganese) and Si (Silicon) and B(Boron) represent Mo, Ti and Nb in iron-nickel alloys (Zhang and Zhao 2013). The Laves formation is promoted by high temperate, time and stress with a negative effect on creep properties and tensile ductility when precipitates are too much (Glade, 2007).

The microstructure of general nickel-based superalloys is mainly constituted by two phases, an FCC γ Ni matrix and ordered distributed γ'phase, with an FCC crystal structure illustrated in Figure 2.27 (Markusson, 2017). The formation of these precipitates is the key strengthening mechanism for many superalloys and the addition of Ta, Ti and Nb promotes this phase. The FCC has higher atomic mobility with better creep resistance than BCC. In addition, FCC structure has higher high temperature strength than BCC because atoms are more densely packed in the FCC structure (Zhang and Zhao, 2012). Nickel-based superalloys generally have a composition element of 55-60 % Ni along with other various alloying elements (Mouritz, 2012).

Figure 2.27: Two main crystal structures in a nickel-based super alloy FCC γ (left) and γ'(right) (Markusson, 2017)

According to Reed (2008), The position of alloy elements within the periodic table determine the influence on phase stabilities, illustrated in Figure 2.28.

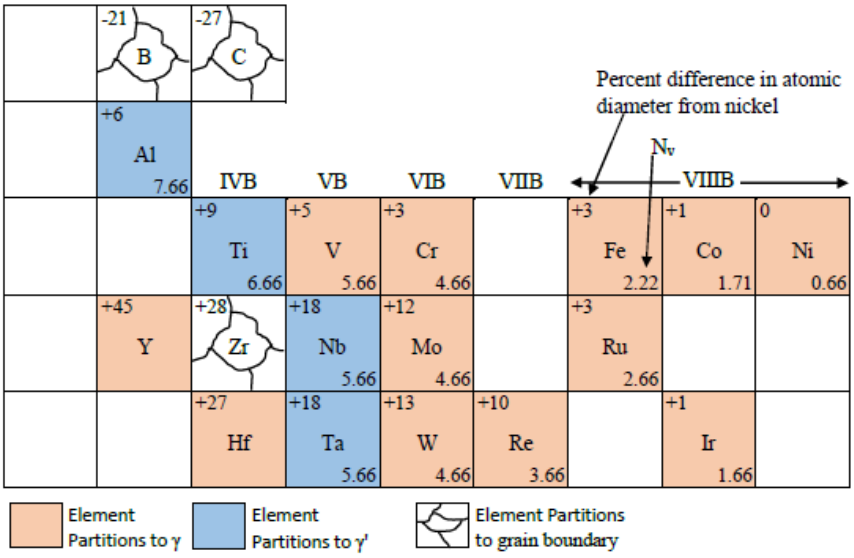

Figure 2.28: Categories of elements to the fundamental principles of nickel-based superalloys and their relative position in the periodic table (Reed, 2008)

2.9 Diffusion in Nickel-Based Superalloys

According Qian et al. (2012), the diffusion process in nickel-based superalloys is important for processing the state of effect on properties of the superalloys and surface stability. Nickel-based superalloys have outstanding mechanical properties and oxidation resistance at higher temperatures (Reed, 2008). According to Karunaratne (2000), diffusion has become important during processing. According to Qiong et al. (2012), the prediction diffusion of superalloys depends on the following alloy elements: Al, Mo, Co, Ta, Ru, W, Cr and, Re in nickel-based superalloys. In diffusion process Al is estimated to be the first element to diffusion and Re the last element to diffusion impurity, sequence order DAl (Diffusion Aluminium) > DCr (Diffusion Chromium) > DCo (Diffusion Cobalt) > DTa (Diffusion Tantalum) > DMo (Diffusion Molybdenum) > DRu (Diffusion Ruthenium) > DW (Diffusion Tungsten) > DRe (Diffusion Rhenium) above $427^{0}C$ (Qiong et al., 2012).The diffusion of transition metal solutes in nickel has been studied using quantum mechanical first principles methods, as in Figure 2.29 (Mantina et al., 2009).

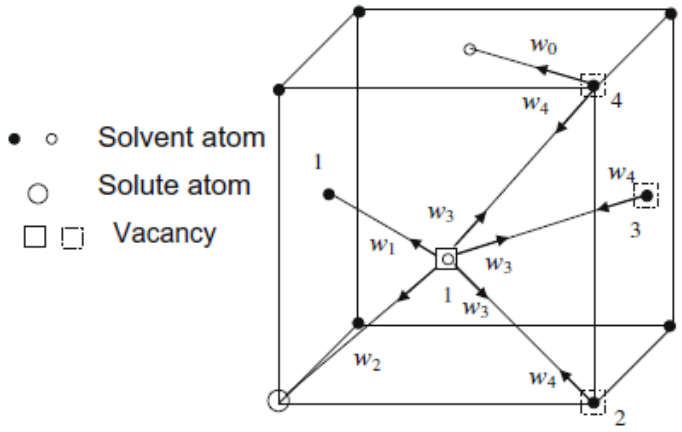

Figure 2.29: FCC (face centred cubic) model for vacancy jumps in a crystal near an impurity (Mantina et al., 2009)

According to Manitna et al. (2009), alloys with weaker vacancy focus in terms of the frequency formula gives the ratio of solute diffusion to the solvent diffusion

$$\frac{D_s}{D_0} = \frac{f_2}{f_0}\frac{w_2}{w_1}\frac{w_4}{w_0}\frac{w_1}{w_3} \qquad (2)$$

where D_s = solute diffusion rate, D_o = self diffusion rate, f_2 = correlation, f_0 = diffusion factor, w_i ($i = 0 \sim 4$) = atom jump frequencies, w_0 = solvent vacancy exchange frequency,

w_1 = solvent vacancy exchange frequency for the rotational jump around one single solute atom, w_3 = solvent vacancy exchange frequency for all energy changes for vacancy, w_4 = solvent vacancy exchange frequency of diffusivity versus inverse of temperature, w_2 = vacancy exchange frequency

Vacancy Assisted Diffusion in Nickel Alloys:

$$D = fa^2\Gamma_s p_v \tag{3}$$

where f = correlation factor, a = lattice parameter, p_v = probability the site next a solute atom is vacant (depend on the energy)

Frequency of solute vacancy exchange:

$$\Gamma_s = v_0 \exp\left\{-\frac{E_b}{kT}\right\} \tag{4}$$

where v_o = Debye frequency, E_b = Barrier energy, k = Boltzmann constant, T = Temperature

Probability the site next a solute atom is vacant (depend on the energy)

$$p_v = C_0 \exp\left\{-\frac{E_f^V}{kT}\right\} \tag{5}$$

$$E_f^V = E_f^{vac,Ni} + \Delta E_V^* \tag{6}$$

where C_o = is a constant, $E_f^{vac,Ni}$ = formation energy in pure nickel, ΔE_V^* = vacancy binding energy, k = Boltzmann constant, T = Temperature in Kelvin

This following form $D = fa^2\Gamma_s p_v$

$$D = v_0 \exp\left\{-\frac{E_b}{kT}\right\} \times C_0 \exp\left\{-\frac{E_f^V}{kT}\right\} \tag{7}$$

The familiar Arrhenius forms

$$D = D_o\left\{-\frac{Q}{kT}\right\} \tag{8}$$

where D_o = diffusion prefactor (intercept), Q = activation energy, k = Boltzmann constant, T = Temperature in Kelvin

With regards to diffusion of transition metals in Nickel, larger atoms diffuse faster, which is due to variations in the solute-solvent bonding characteristics (Fu et al., 2012). According to Qiong et al. (2012), differences in the diffusion coefficient are caused mainly by variations in the barrier energy. The bonding electronics effect dominate, which means solute size effects are relatively unimportant. This effect explains why elements such as Re (Rhenium) improve the temperature properties of nickel-based superalloys (Fu et al., 2012; Rehman, 2016). According to Rehman (2016), the above mentioned diffusion process is one of the best ways to investigate the properties of superalloys.

2.10 Effect of elements on properties of Nickel-Based Superalloys

According to Losertová (2014), Ni is able to dissolve lager amounts of alloying elements in it than iron, and even more so than chromium, molybdenum and tungsten. This allows for applications in much more aggressive environments than stainless steels. The specific effects of major selected element composition additives, on nickel alloys are illustrated in Table 2.7, Note that not all effects may be observable in a given alloy.

Table 2.7: Roles of alloying elements in nickel-based superalloys (Adapted from Donachie, 2002)

Effect	Alloying Elements
Solid solution strengthens	Co (Cobalt), Cr (Chromium), Fe (Iron), Mo (Molybdenum), W (Tungsten), Ta (Titanium)
Carbide formers MC M_7C_3 $M_{23}C_6$ M_6C	 W (Tungsten), Ta (Titanium), Ti (Titanium), Mo (Molybdenum), Nb (Niobium), Hf (Hafnium) Cr (Chromium) Cr (Chromium), Mo (Molybdenum), W (Tungsten) Mo (Molybdenum), W (Tungsten), Nb (Niobium)
Carbonitrides: M(CN)	C (Carbon), N (Nitrogen)
Forms $\gamma' Ni_3(Al, Ti)$	Al, Ti (Titanium)
Raises temperature of γ'	Co (Cobalt)
Hardening precipitates and/or intermetallic	Al, T i(Titanium), Nb (Niobium), Ta (Tantalum)
Oxidation resistance	Al, Cr (Chromium), Y(Yttrium), La (Lanthanum) , Ce (Cerium)
Improve hot corrosion resistance	La (Lanthanum), Th (Thorium)
Improves creep properties	B (Boron), Ta (Tantalum)
Increases rupture strength	B (Boron)
Grain boundary refiners	B (Boron), C (Carbon), Zr (Zirconium), Hf (Hafnium)

2.11 Strengthening Mechanisms for Nickel-Based Superalloys

According to Askeland (1985), nickel-based superalloys have the following mechanisms: precipitation hardening precipitation and solid solution strengthening. In addition to these mechanisms the following add further strength in nickel-based superalloys; controlling of crystal orientation, grain boundary size, grain aspect ratio and orientation, controlling microstructure by heat treatment and application of production process (Decker, 1979). Figure 2.30 illustrates stress rapture comparison of solid solution, carbides and solid solution strengthening behaviour for three class superalloys: nickel-cobalt and iron-based. Furthermore, Table 2.8 shows the principal strengthening mechanism of Inconel 625 and 718 the two nickel-based additive manufactured superalloys on which this paper will mainly focus.

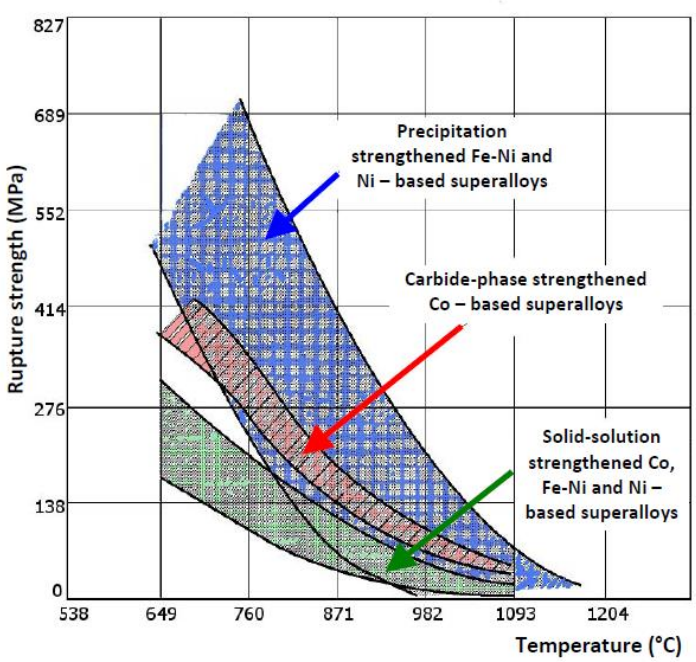

Figure 2.30: Stress rapture strength of nickel, cobalt and iron superalloys denoted with arrows (Donachie and Donachie, 2002)

Table 2.8: Principal Strengthening mechanism of Additive manufactured Inconel 625 and 718 nickel-based superalloys (adapted from Hosseini, and Kishawy, 2018 and Zhang and Zhao, 2013)

Solid solution strengthening	• Efficiency on mechanical strength is limited, very useful to improve creep and stress rupture resistance. • Co, Mo and W influential elements for solution hardening • Solubility in FCC matrix is higher than that in BCC • Fe and Co based alloys are alloyed with Ni solid solution to gain FCC matrix structure
Precipitation hardening of intermetallic	• The main strengthening mechanism of nickel-based superalloys. • Gamma prime phase (γ') can retain their stability up about to 1150^0C, which is well above the (γ'') in Inconel 718 which is only about 650^0C.
Precipitation hardening of carbides	• The brittleness and reduced feasibility of production are the main disadvantages of carbide strengthening.
Grain size	• An important and usually adjustable parameter is that its behaviour is based on the temperature and component height. • Large grains mean less grain boundary in the alloys.
Grain orientation	• Very useful strengthening mechanism when applied loads are anisotropic such as turbine blades. • Orientation can be obtained by directional solidification and rolling technique for cast and wrought alloys respectively.
Crystallographic orientation	• Some orientations are preferable due to higher strength in FCC matrix, such as <100>. • It can be obtained by SX (single crystal) casting technique
Alloy cleanliness	• Cleanliness can dramatically alter the properties of the alloys; it usually causes drop in incipient melting temperature and unwanted phases formation which causes brittleness.

CHAPTER 3

3.0 Heat treatments

3.1 Heat Treatment Process

According El-Bagoury (2016), the purpose of heat treatment is to achieve size and distribution of hardening precipitates in alloys that would result in optimum mechanical properties, namely resistance to fracture, hardness and corrosion at high temperatures. Mechanical properties of superalloys when heat treatment is in process strongly depend on alloy microstructure, chemical composition, volume fraction and phase morphology (Reed, 2006). Because of the complex microstructure in superalloys it can be challenging to formulate a heat treatment regime that is both effective in strengthening, and which affects time and cost of this process (Shaikh, 2018). The effect of heat treatment on mechanical properties is compared with as built specimens illustrated in Figure 3.1.

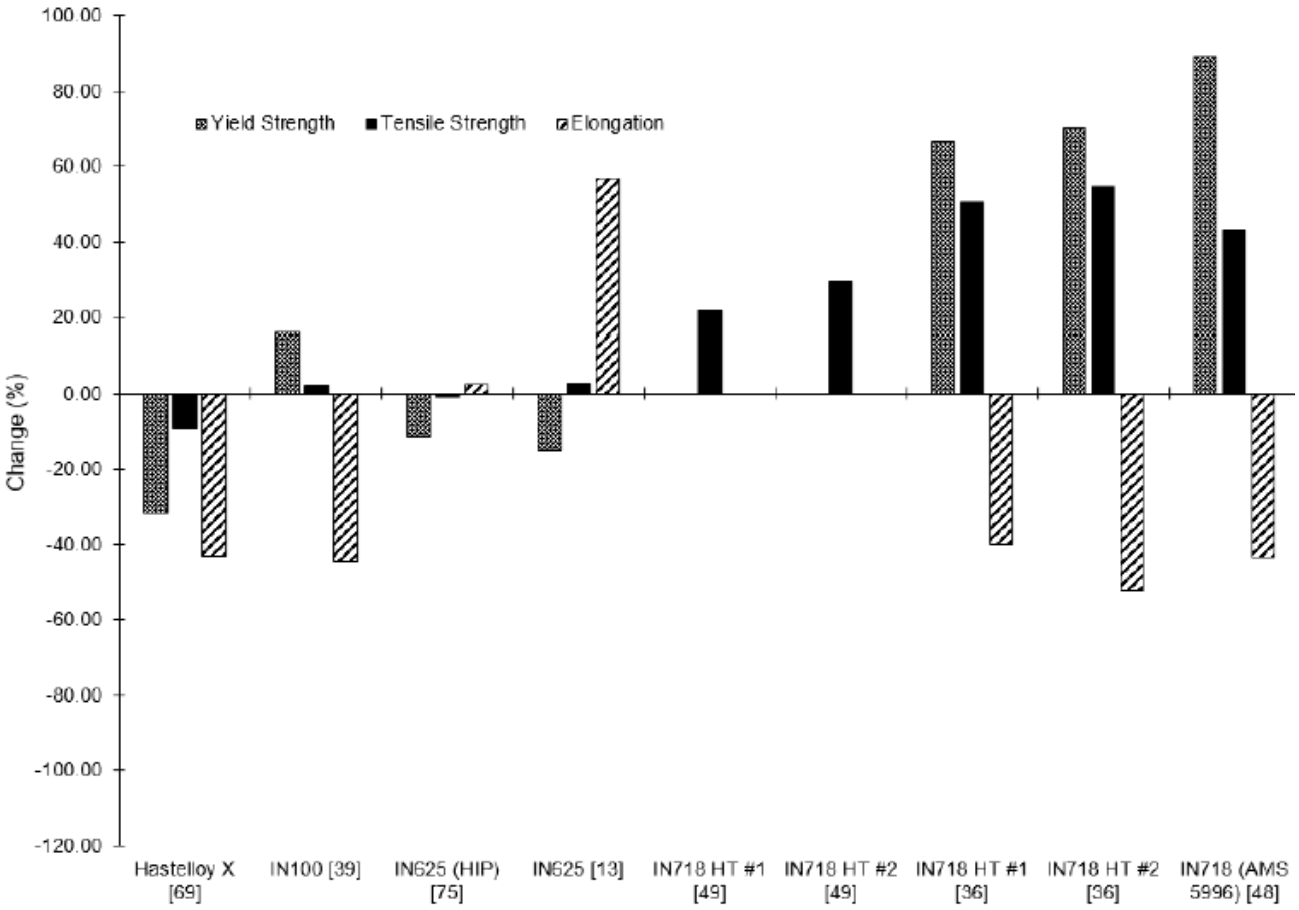

Figure 3.1: Effect of Heat Treatment On Mechanical Properties Compared with as built specimens (Graybil et al., 2018)

Inconel nickel-based superalloys wrought, cast and additive can be used for a higher fraction usually in most case until 70% of the melting temperature (Bhadeshia, 2003). According to El-Bagoury (2016), nickel-based superalloys wrought, cast or additive manufactured may be subjected to one of five types of principal heat treatment methods.

The five methods or principal types include, stress relieving, annealing, solution treating, age hardening and hot isostatic pressing.

3.1.1 Stress Relieving

According to Deng (2018), stress relieving process reduce stresses in work hardened alloys, without recrystallizing any grain structure. According to El-Bagoury (2016), metallurgical characteristics and related properties in part or components all depend on time and temperature.

Nickel alloys temperature range from $425^{0}C$ to $870^{0}C$ is also based on alloy chemical composition, strain hardening, and is normally below annealing or recrystallization (Deng, 2018; El-Bagoury, 2016). Superalloys with complex shapes should be stress relieved to prevent any possibility of crack initiation (Glade, 2007).

Stress equalizing: this heating process is a low temperature heat treatment that evenly distributes stresses in plastic deformation metals without affecting or decreasing the mechanical strength in cold work process (Kopeliovich, 2012).

3.1.2 Annealing

Annealing is usually performed in single phase temperature range from $700^{0}C$ to $1200^{0}C$. This depends on the composition of alloy and characteristics below recrystallization temperature for nickel alloys (Total Materia, 2001). This process is used to complete recrystallized structure to improve ductility, reduce hardness, reduce residual stress further and generate specific microstructures (Glade, 2007).

The open and closed annealing process is often used for Inconel 625 and 718. The open annealing process temperature range between $980^{0}C$ to $1150^{0}C$ for Inconel 625, and 955 ^{0}C to $1110^{0}C$ for Inconel 718, protected from all oxidation by the product of combustion in fuel heated furnace or reducing gas intake into electric furnace (Total Materia, 2001). According to El-Bagoury (2016), after annealing, the grain size of nickel-based superalloy depends on the chemical elements' composition, amount of hot or cold deformation, and annealing temperature which is generally between 1 to 8 hours. According to Total Materia (2001), the closed annealing process require more time than open annealing; because of the lower temperature used, temperature control is less critical then open annealing.

3.1.3 Solution Treatment

According to El-Bagoury (2016), solution treatment is to improve age treatment process made possible with dissolving second phase that homogenize the microstructure and resistance. The main purpose or task of solution treatment is to dissolve gamma prime (γ') phase and carbides, the gamma prime (γ') strengthened nickel-based superalloys are defined by properties after aging process (El-Bagoury, 2016 and Sames, 2015). The increase of temperature, a transformation grain growth occurs and more carbides are dissolved in this process, because of this over aging the strength decreases. Illustrated in Figure 3.2 (a) yield strength vs solution temperature and (b) creep rapture vs solution treatment of nickel-based superalloys (El-Bagoury, 2016).

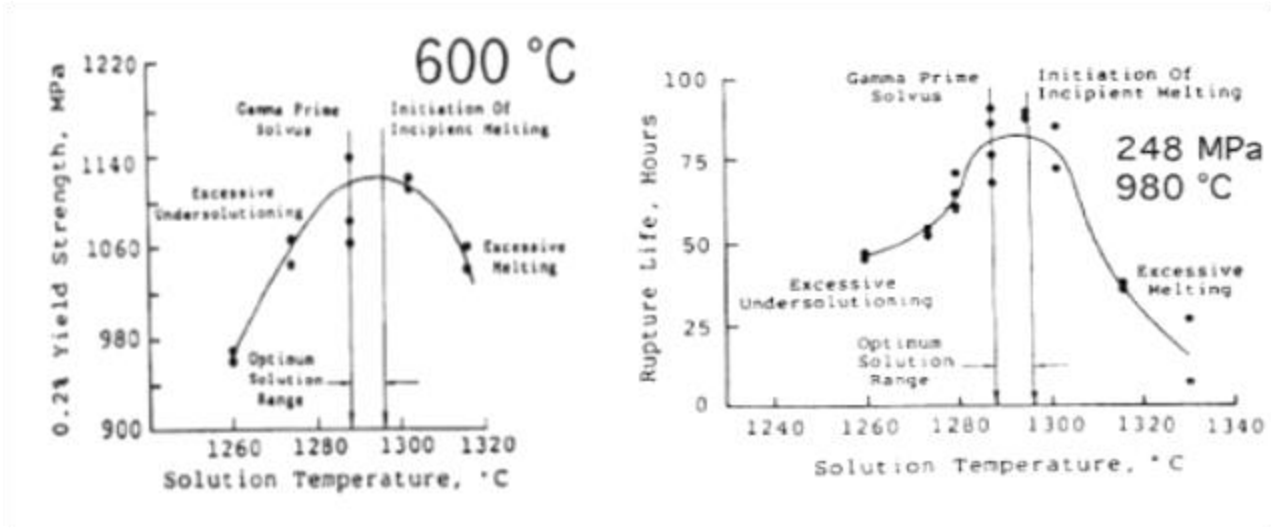

(a)Yield strength vs Solution Temperature (b) Creep rupture vs Solution Temperature

Figure 3.2: Solution Treatment for nickel-based superalloys (El-Bagoury, 2016)

3.1.4 Quenching

According to Moss and Basic (2013), quenching is the cooling of a component or part in water, oil or water (liquid) not air to obtain certain material structures. Quenching is used to obtain the solid solution matrix at room temperature 20^0C, which will produce a finer (γ') gamma prime particle size after a precipitation hardening aging process. According to Wacker et al. (2017), quenching can reduce grain size of metallic and plastic materials and may increase their hardness based on time during thermodynamic and kinetic access.

3.1.5 Precipitation age hardening

According to Retima et al. (2010), the precipitation of multiple phases strengthens nickel-based superalloys and forms a solid solution matrix, a process that is generated by solution treating and quenching. According to El-Bagoury (2016) and Sames (2015), the ageing treatment conditions depend on the number of precipitating phases, which depend mainly on service temperature that dissolves any undesired phases, and on the desired mechanical properties, Figure 3.3 illustrates the typical stepwise precipitation hardening process.

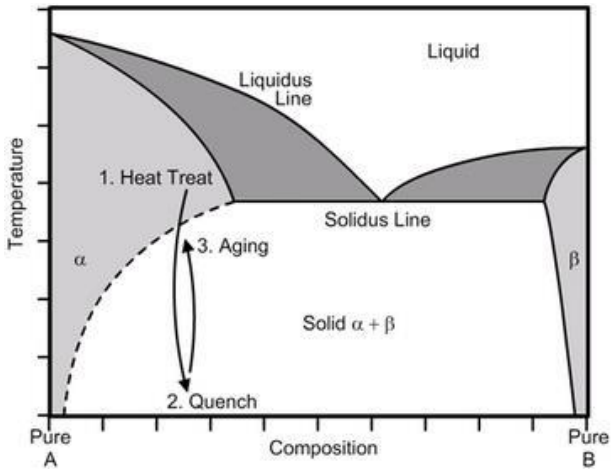

Figure 3.3: Three steps phase diagram of the age hardening process (Petersen-Overleir, 2015)

Table 3.1: Common post heat treatment recommended for Additive Inconel 625 and 718 (adapted from 3dmaterialtech, 2013., ASM Vol 4, 1991., Deng, 2018, and Brand 2016)

Treatment	Inconel 625	Inconel 718(ASM 5664)
Stress Relief Cooling method	$1177^0C \pm 25^0C$ 2hrs ± 15min AC (Air Cooling)	$1066^0C \pm 25^0C$ 1.5hrs, Furnace
Annealing Cooling method	980^0C -1150^0C 1hr Cooling rate is not critical	955^0C -1065^0C 8hrs, AC (Air Cooling)
Solution treating Cooling method	1093^0C – $1204\ ^0C$ Cooling rate has no effect	1065^0C -1900^0C 1hr, AC (Air Cooling)
Aging Cooling method	650^0C ,18hrs AC (Air Cooling) To achieve maximum tensile and hardness properties	$760\ ^0C$ hold 10 hr; furnace cool to $650\ ^0C$ hold until furnace time for entire cycle equals 20 hr AC (Air Cooling)

Note the common post heat treatment recommended provides just a guideline for heat treatment process based on application for Inconel 625 and 718.

CHAPTER 4

4.0 Mechanical Properties

4.1 Mechanical Deformation

According to Moleejane (2009), when a metal or any other structural material has an applied external load which deforms and may change dimensions, this process may be time dependent and defined as stress and strain, as illustrated in Figure 4.1.

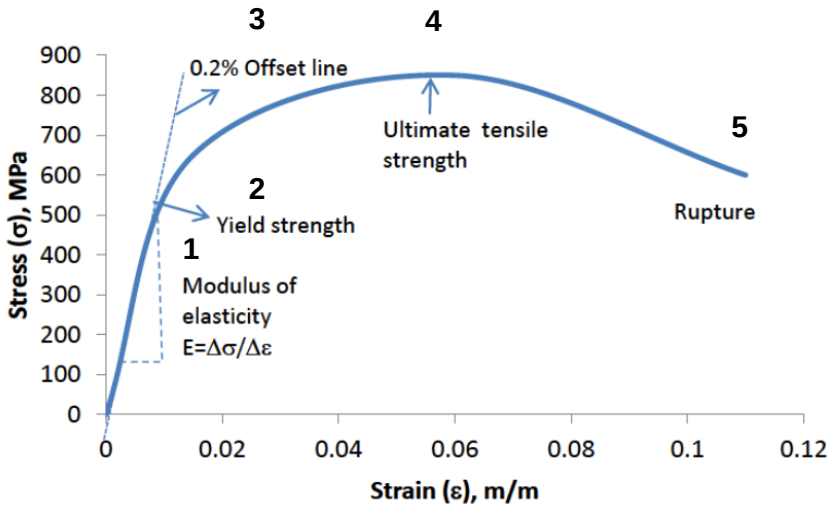

Figure 4.1: Stress and strain (Adapted from Moletsane, 2016)

General stress versus strain response (adapted from Callister, 2013 and Moleejane, 2009)

1. The elastic limit is reached when a material will no longer have its original shape when the applied load has been removed or the maximum stress that may occur.
2. The 0.2% offset yield strength is the stress σ value.
3. σ 0.2% yield strength of the intersection of a line (called the offset) is constructed parallel to the elastic portion of the curve but offset to the right by a strain of 0.002. It represents the onset of plastic deformation. The yield point is when material has a yielding point without increase in load.
4. The maximum coordinate in stress vs strain graph illustrated is ultimate tensile strength.
5. The breaking strength of a material at rupture (instant breaking) point.

4.1.1 Elastic deformation

This means a temporary change in shape after the applied load is removed and a solid body reverts to its original shape and size. Elastic deformation occurs when atomic bonds in the material involves stretching but no slipping past each other, as illustrated in Figure 4.2.
Elastic solid's mainly characterised responses after deformation:

- Removing the load, the deformation disappears completely.
- Rate of applied load does not have an effect.
- Deformation is very small.

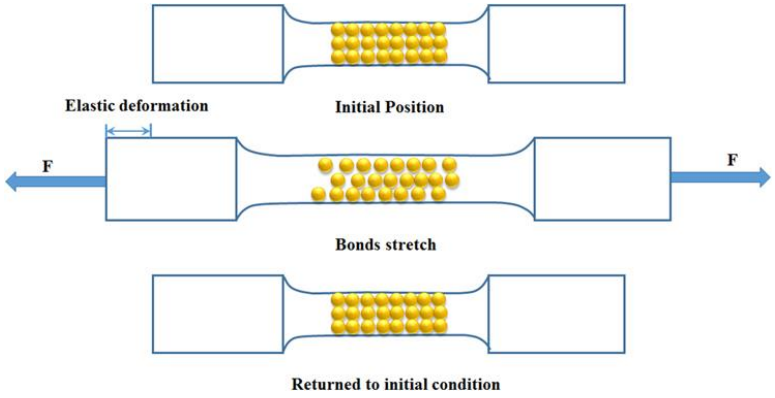

Figure 4.2: Material below yield strength (Lavakumar, 2018)

4.1.2 Plastic Deformation

Applied stress results in deformation of a solid body, which remains deformed after the applied stress is removed. The plastic phase means a transition from pulling or moving atomic bonds from orderly arrangements to a disorderly arrangement which leads to imperfection as illustrated in Figure 4.3. This allow the atoms to slip past each other at a lower stress level (Lavakumar, 2018; Moleejane, 2009).

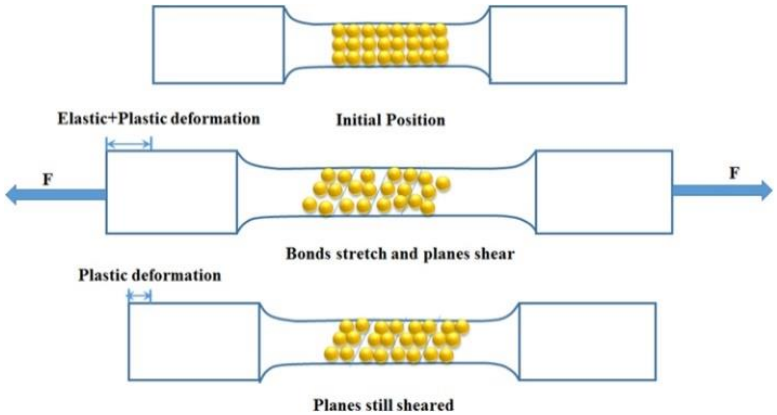

Figure 4.3: Material above yield strength (Lavakumar, 2018)

The energy required to dislocation is lowest along the densest planes of atoms, dislocations have a preferred direction of travel within grains of the material (Moleejane, 2009). According to the Belytschko et al., (2003) and Maugin (1992), plastic deformation result in slip along the parallel planes within the grain. This groups together to form slip bands which can be seen with an optical microscope, illustrated in Figure 4.4.

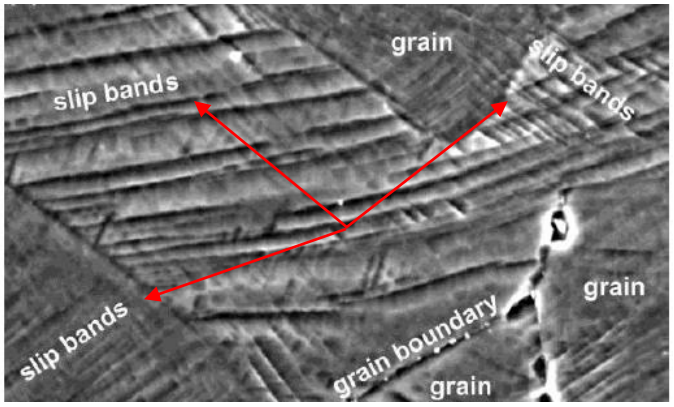

Figure 4.4: Slip bands with in grain caused by plastic deformation denoted with arrows (Mohamed, 2013)

4.2 Three Point Beam Bending

This mechanical testing method measures the behavior of materials subjected to simple bending loads; tensile modulus and bending modulus (stiffness) is calculated from the slope of the bending load. The three-point bending test involves the bending of a material at a point, most bending test experiments calculate the bending in the center or midpoint to determine the bending stress and maximum deflection of the material illustrated in Figure 4.5. Bending stress, bending strain, maximum deflection, modulus of elasticity and other related quantities can be determined when values of three-point bending are given. According to JLW Instruments (1983), the advantage of three-point bending test is the simplicity of sample specimen preparation and testing.

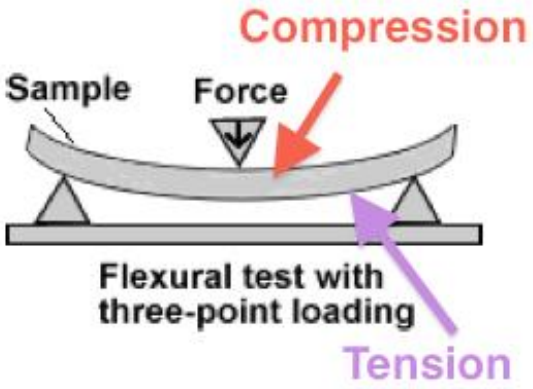

Figure 4.5: Three-point bend sample experiencing compression and tension stresses (Bending Test, n.d)

The basic results of a tensile test are quantities of bending stress, bending strain and modulus of elasticity. The bending strength of a material is defined as the maximum bending stress that can be applied to that material before it yields, which is also called as bending strength or modulus of rapture.

Bending stress σ_f : When a load is applied in the centre between two supports, this load will be perpendicular to the length of the beam and maximum stress occurs at the outer surface of the centre of the sample specimen .

The force multiplied by the length of support span during test is divided by the initial area of the specimen.

$$\sigma_f = \frac{3Fl}{2bd^2} \qquad (9)$$

where $F =$ the load at a given point on the load deflection curve, l = support span , $b =$ width , $d =$ depth or thickness of the specimen.

Bending Strain is the nominal fractional change in the length of an element of the outer surface of the test specimen at the centre, where the maximum strain occurs.

The maximum deflection of the centre of the beam multiplied by depth divided by the support span may be calculated for any deflection using the following formula:

$$\varepsilon_f = \frac{6Dd}{l^2} \qquad (10)$$

D = maximum deflection of the centre of the beam, l = support span, d = depth of the specimen.

Modulus of Elasticity E_b is the ratio within the elastic limit when stress is applied to corresponding strain.

The length of the support span during the test multiplied by the slope of the tangent to the initial straight line divided by the initial area of the specimen:

$$E_b = \frac{l^3 m}{4bd^3} \qquad (11)$$

l = support span, m = slope of the tangent, $b =$ width, $d =$ depth or thickness of the specimen.

4.3 Additive Manufactured Mechanical Properties

According to Sames (2015), the understanding and performance of mechanical properties of additive manufactured materials are still being investigated. The main focus of additive manufacturing is on mechanical properties, mainly tensile behaviour and hardness. Nickel-based additive manufactured superalloys yield a higher ultimate tensile strength than wrought and cast nickel-based super alloys based on the heat treatment process (Adeleji, et al., 2017). According to Wang et al. (2017), the process parameters of additive manufacturing may have a remarkable effect on mechanical properties based on laser power, powder and manufacturing speed: furthermore these mechanical properties will increase after post heat treatment.

There are other factors to consider when it comes to mechanical testing of additive manufactured materials, namely fatigue life, creep, residual stress, porosity, thermal history and the test specimen's orientation for this dissertation, the main focus will be on tensile and hardness behaviour. Table 4.1 displays the general tensile properties of additive manufactured and traditionally manufactured super alloy Inconel 625 and 718 in both // parallel and $\perp$ perpendicular direction. Figure 4.6 illustrated tensile strength and elongation of additively and conventional manufactured Inconel 625 and 718. The chemical elements powder used was produced by NLC (National Laser Centre) in Pretoria South Africa in partnership with Optomec 3D manufacturing company which specialises in additive manufacturing.

According Farinia (2018), from a macroscopic point ultimate tensile strength and elongation will increase, but the effect is different for each powder's chemical elements. The particle pore size has significant influence on mechanical properties. Pores can be regarded as defects as mentioned above which reduce the effective cross section. This means that mechanical properties are degraded as porosity and pore size increase (Sames, 2015).

Table 4.1: Tensile Properties of additive and traditionally manufactured Inconel 625 and 718 at room temperature $20^{0}C$

(Adapted from ASM, 2000; Chlebus et al., 2015; Optomec, 2014; Wang et al., 2009)

Material	Orientation //(Parallel) ⊥ (Perpendicular)	YS Yield Strength (MPa)	UTS Tensile Strength (MPa)	Elongation (%)
625	⊥	964	1052	33
718	⊥	1097	1335	16.6
718 SLM	⊥	1159 ± 32	1377 ± 66	8 ± 6
625 ASTM F3056 - 14e1	⊥	770 ± 30	1040 ± 20	22 ± 2
718 ASTM F3055 -14a	⊥	940	1240	12
625	//	490	829	43
718	//	1088	1247	21.7
718 SLM	//	1074 ± 42	1302 ± 6	19 ± 2
625 ASTM F3056 - 14e1	//	730 ± 20	1030 ± 20	33 ± 1
718 ASTM F3055 -14a	//	920	1240	12
625 ASM 5663	-	517	930	42.5
718 ASM 5663	-	1034	1241	12

Note that mechanical properties can vary with processing parameters, heat treatment and precise chemical elements.

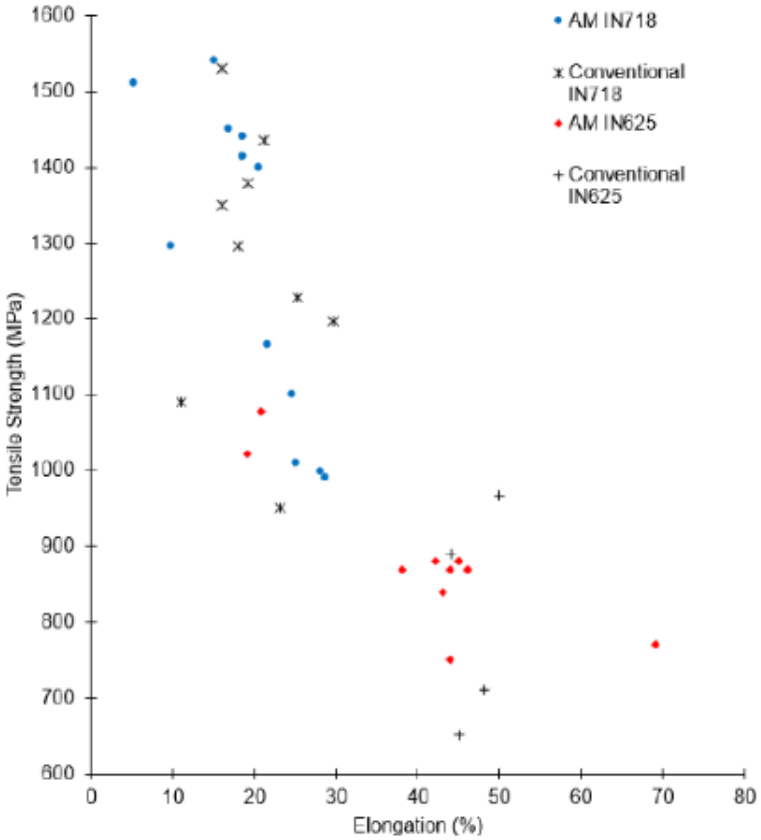

Figure 4.6: Tensile strength and elongation of additively and conventional Inconel 625 and 718 (Graybil et al., 2018)

4.3.1 Relationship between Processing, Microstructure, Grain Size and Mechanical Properties

According to Sames (2015), microstructure process parameters are directly related to the mechanical properties of a material. Figure 4.7 summarizes and explains the process, microstructure and effect relationship. According to Moleejane (2009), the properties of most materials generally depend on the microstructure, arrangement of atoms, orientation and morphology of crystals as well as chemical composition, size of the microstructural in one, two or three dimensions, and thermal mechanical loading.

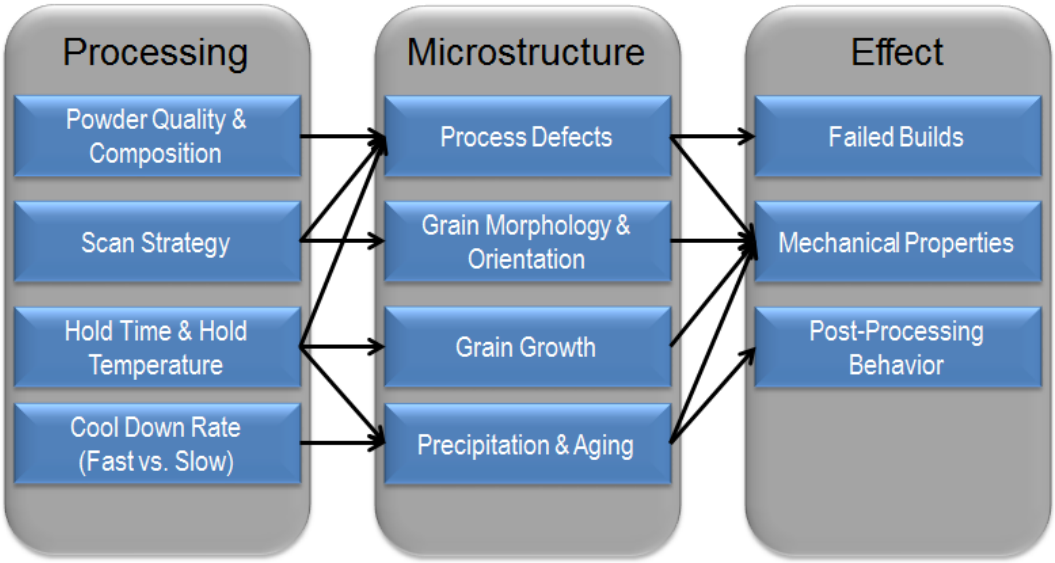

Figure 4.7: Flow diagram showing the relationship of processing, microstructure and impact (Sames, 2015)

The majority of mechanical properties like hardness, tensile strength, impact strength, fatigue strength and yields strength all has an effect based on the grain size; all will increase with grain size decrease, illustrated in Figure 4.8 (Herring, 2005). According to Dieter (1961), the machinability is also affected. Rough machining favours coarse grain size while finish machining favours finer grain size. According to Dieter Jr. (1961) and Thelning, (1967), the grain size has a greater effect on properties with early stages of deformation. For nickel-based superalloys the yield stress may have greater dependence on grain size than tensile strength. The decrease of grain size vs increasing properties illustrated in Figure 4.9 will affect the strength, toughness, weldability and ductility of additive manufactured, wrought and cast nickel-based superalloys.

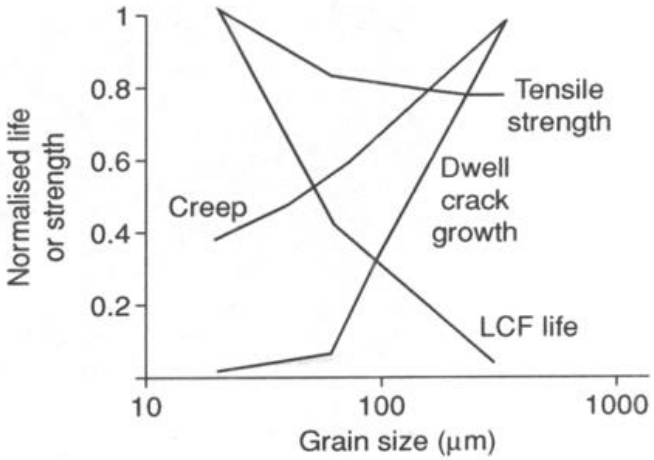

Figure 4.8: Dependence of the mechanical properties on grain size (Reed, 2006)

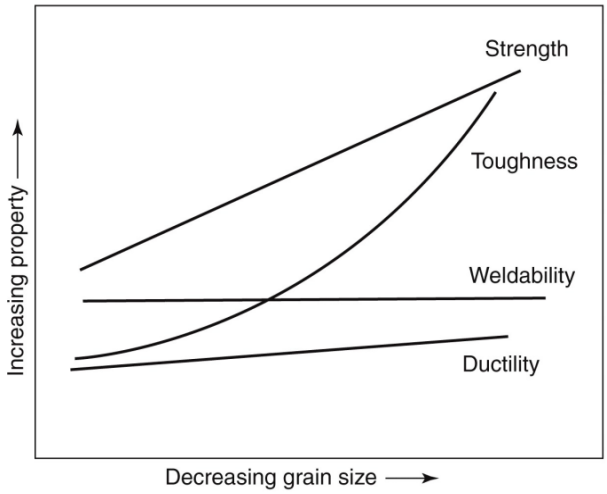

Figure 4.9: Influence of decreasing grain size on mechanical properties (Hertzberg and Vinci, 2013)

4.3.2 Influence of Grain size and deformation effect on Ultimate Strength and Hardness

According to Petersen-Overleir (2015), mechanical properties of multicrystalline or polycrystals materials are effected by grain size. Grain boundaries are shared between neighbouring grains and usually have different crystal structure orientation. There are other properties also influenced beside grain size, yield strength is also influenced by factors such as chemical composition, illustrated in Figure 4.10. The slip motion during plastic deformation must take place from one side to the other across the shared grain boundary. This process activates the shared grain boundary slip barrier. According to Moleejane (2009), the average grain size decreases the more the metal yield strength increases and as grain size increases the yield strength decrease.

The Hall-Petch equation states that yield strength varies with grain size according to:

$$\sigma_y = \sigma_0 + k_y d^{-\frac{1}{2}} \qquad (12)$$

where σ_y = yield strength, σ_0 = frictional stress opposing motion of a dislocation, k_y = extent to which dislocations are piled up at barriers, d = the average grain diameter

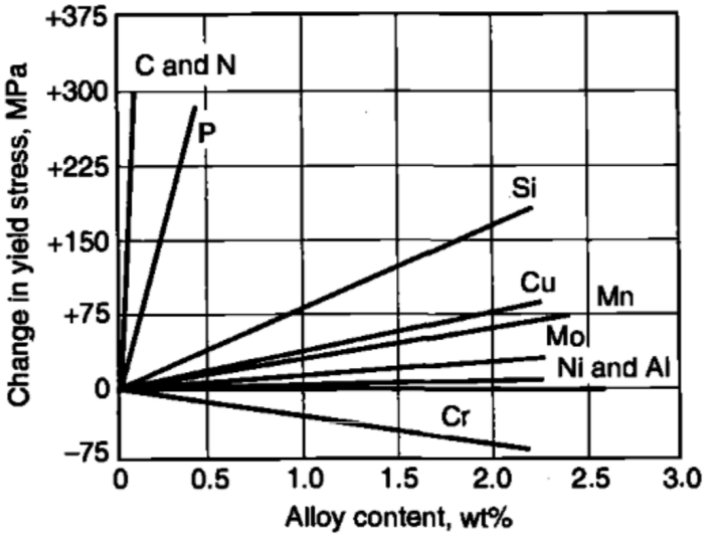

Figure 4.10: Influence of alloying elements on yield strength (Dieter, 1997)

The hardness of metals can be defined as measurement of resistance to plastic deformation, cutting, scratching and resistance to bending; in summary the metal's strength will be determined usually by penetration or indentation. According to Siedoda et al. (2004), polycrystalline materials usually show an increase in hardness and strength with decreasing grain size according to the Hall-Patch relationship. The influence of grain size and strength indicates strength cannot increase infinitely when grain size decreases at critical value d_c illustrated in Figure 4.1. The maximum grain size depends on strength or hardness (Schiotz, 200; Wang, 2010). The strength is related to the deformation process and grain boundary volume, for example creep, which is an important application of polycrystalline materials in the field requiring long term stability.

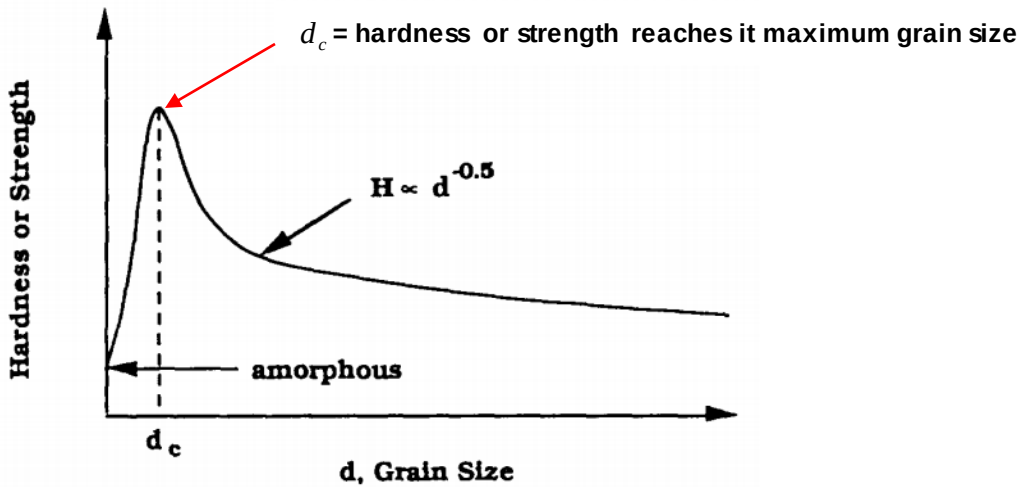

Figure 4.11: Grain size dependence on strength or hardness (Wang, 2010)

CHAPTER 5

5.0 Experimental Techniques for Mechanical Properties Characterisation and Microstructure Investigation

The main focus of this chapter is the consideration of relatively simple experimental methods to determine material properties of additive manufactured Inconel 625 and 718 with different grain size structure and chemical composition. Standard experimental tests were undertaken with the aim of finding the mechanical properties (bending strength, elongation, ultimate strength and hardness), chemical composition, diffraction and grain size for the chosen materials.

5.1 Mechanical Properties Characterisation

5.1.1 Standard tensile stress, strength and yield strength test and the principle of operation

Tensile strength and elastic modulus can be compared to bending modulus, hardness values can be obtained from tensile strength as illustrated in Figure 5.1. This implies that instead of conducting a tensile test to obtain tensile value and hardness test to obtain hardness values, a three-point beam method can be used. Three-point bending is a method whereby an elastic material is tested in bending a simple beam supported at two points and loaded at the midpoint. During this loading process the maximum stress occurs at the outer side if the midpoint illustrated in Figure 5.1.

Test specimen geometry

The measurement of tensile properties was performed using standard rectangular test specimens according to ASTM D 790.

Table 5.1: Standard and Inconel 625 and 718 specimen dimensions

Parameter	Standard specimen *mm*	Inconel specimens *mm*	
	ASTM D 790	625	718
Beam length	125	60.13	60
Beam height	3.2	4.14	2.7
Beam width	12.7	12.98	12.88

1. The test specimens were placed on a bending jig, and the centre of the beam was marked.
2. The force was applied to the centre mark of the specimen, the resulting forces applied to the specimen were measured and recorded simultaneously at regular intervals.
3. During the test, the force applied to the sample specimens and the resulting force applied on the sample specimens were measured and recorded simultaneously at regular intervals.
4. The applied force data was then used to quantify a number of important mechanical properties (bending stress and strain).

The tests were carried out in accordance with ATSM D790 at room temperature $20^{0}C$.

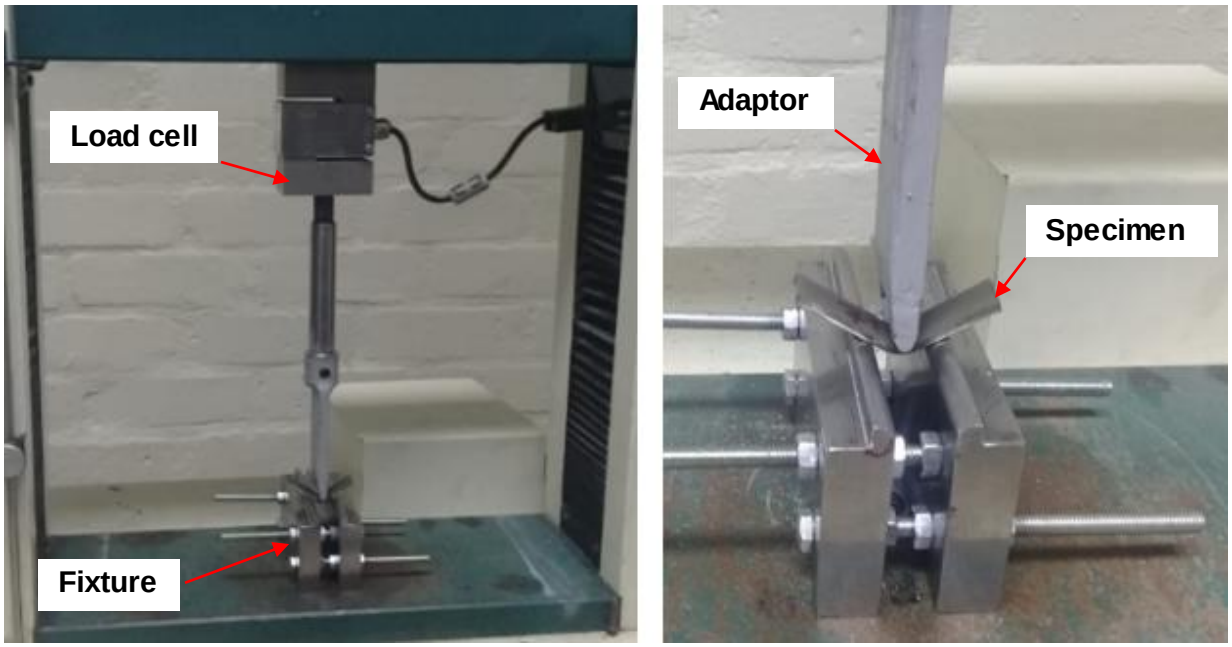

(a) Tensile Test machine (b) Tensile test piece mounted

Figure 5.1: Tensile bending test

The test specimen illustrated in Figure 5.1 subjected to bending test was calculated according to bending equation (9). According to ASTM (2017), during testing the same materials, no breakage occurs of strain up to 5% difference. This may give a load deflection curve that indicate a point if the load does not increase with an increase in strain, as illustrated in Figure 5.2, curve b. The bending strength may be calculated for these materials by letting F in bending equation (9) equal this point.

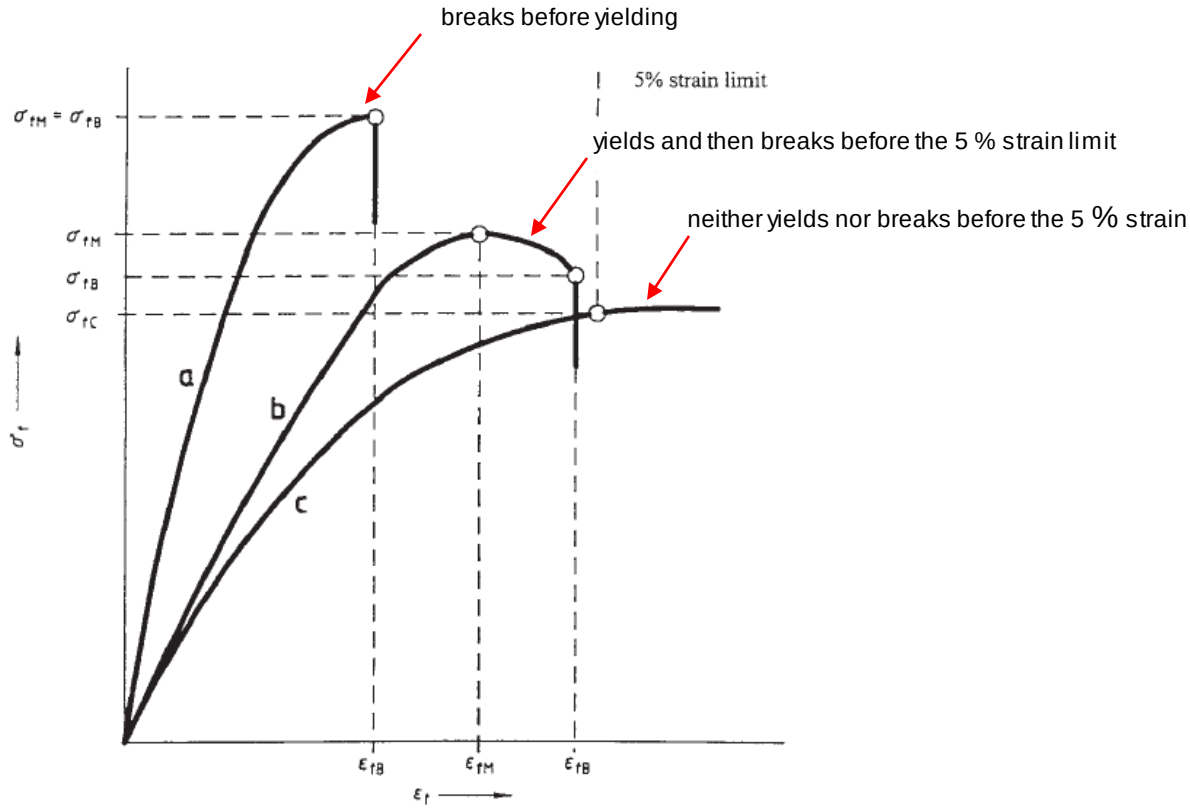

Figure 5.2: Typical Curves of Bending Stress and Bending Strain (ASTM, 2017)

5.2 Hardness Test

According to Tsotetsi et al. (2018), hardness in engineering terms is generally related to the mechanical characteristics and properties of a material, which means the harder the material, the greater the resistance during penetration. The factors material hardness may depend on include microstructure, grain size, ductility, strain and stiffness. Based on material use, the hardness increases therefore yield strength and ultimate tensile strength increase.

There are different types of hardness tests such as Rockwell, Brinell, Knoop and Vickers hardness tests to determine hardness of materials. This study focuses on the Rockwell hardness test, illustrated in Figure 5.3. The results are discussed in section 6.3. experimental results for mechanical properties characterisation.

Figure 5.3: Rockwell hardness test machine

5.2.1 Rockwell Hardness Test

According to Tsotetsi et al. (2018), the Rockwell hardness test has two indenters, normally a diamond cone or hard steel ball depending on material hardness, as illustrated in Figure 5.4. There are several alternative scales, the most commonly used being the "B" and "C" scales. Both scales express hardness as an arbitrary dimensionless number all the scales are given in table 5.2. Rockwell hardness determination of a material includes two steps: the application of minor load and then major. The hardness value is read directly from a dial or display. The main advantage of the Rockwell hardness test as compared with other hardness test is their need for measurement techniques that involve tedious calculations (Moleejane, 2009).

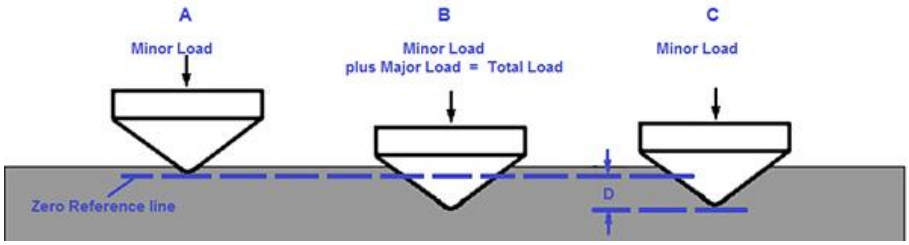

Figure 5.4: Rockwell hardness test (Newage hardness testing, n.d)

Table 5.2: Commonly used Rockwell hardness scales (adapted from Dowling, 2013)

Scale X	Indenter Type mm	Load kg	Typical Application
A	Diamond Brale	60	Tool materials
D	Diamond Brale	100	Cast iron, sheet steels
C	Diamond Brale	150	Steels, hard cast irons, Ti alloys
B	1.588 mm Diamond Ball	100	Soft steels, Cu and Al alloys
E	3.175 mm Diamond Ball	100	Al and Mg alloys, other soft metals: reinforced polymers
M	6.35 mm Diamond Ball	100	Very soft metals; high modulus polymers
R	12.7 mm Diamond Ball	60	Very soft metals; low modulus polymers

5.3 Sample Specimen Preparation

Sample specimen preparation was conducted at Cape Peninsula University Technology (CPUT) Bellville campus for SEM (scanning electron microscope) and LOM (light optical microscope) analysis. This sample was cut and prepared under the supervision of the assigned lab technician wearing the necessary personal protective equipment (PPE) as required.

5.3.1 Wire cutting specimens for thermal moulding process

Samples were prepared as described below following the ASTM A·395 standard. In this study 4 test sample specimens of 40 x 20 mm, 2 of Inconel 625 and 2 Inconel 718 parallel and perpendicular to the building direction were cut using the wire cutting machine illustrated in Figure 5.5.

Figure 5.5: Wire cutting machine

5.3.2 Thermal moulding process for microstructure analysis

The test specimens were embedded in Bakelite hot mounting powder resin using a thermal-compression mounting machine. Standard thermal moulding process was applied as illustrated in Figure 5.6.

1. The specimens were placed one at a time flat on a steel piston rubbed with anti-sticking compound within the machine cylinder.
2. Bakelite hot mounting powder was poured on and around the test specimen in the cylinder.
3. A steel cap was placed and screwed onto the cylinder.
4. A temperature of $\pm 180^{0}C$ and a constant force was set for 20 kN for a period not more than 6 minutes sequentially.
5. After curing the machine was allowed to cool down for 6 minutes and the test specimen was removed from the machine.

a) Thermal compression moulding machine

b) Specimen in mould

Figures 5.6: Thermal moulding specimen preparation

Table 5.3: Specimen grinding and polishing after thermal moulding process

Step	Pad	Polishing solution	Duration min(minutes)
1.Plane Grinding	1500 grit SiC	Water	2 min
2.Fine Grinding	4000 grit SiC	Water	3 min
3.Polishing	Moran	6µm diamond	3 min
4.Polishing	Daran	3µm diamond	3 min
5.Polishing	Napal	1µm diamond	3 min
6.Polishing	Chemal	0.2µm OP solution	1 min
7.Rinsing	Chemal	Water	1 min

The wheel was set to rotate at $\pm$ 200 rpm and the pressure of $\pm 6\,N$ on the test specimens was roughly maintained by periodically adjusting the spring load on the machine illustrated in Figure 5.7. The sample was thoroughly rinsed and dried between steps. For the polishing steps the rinsed samples were covered with a small quantity of ethanol and dried using warm air ready for etching.

Figure 5.7: Rotary Grinding and Polishing machine

5.3.3 Metallographic Etching Solution

The etchant used to determine microstructure and grain boundaries is known as mixed acids etchant.

1. After completion of the last polishing step, the test specimens were taken off the machine and thoroughly cleaned in running water to remove polishing debris.
2. After cleaning the specimens, they were swabb in alcohol to prepare for etching.
3. Inconel 625 specimens was immersed in fresh mixed acid 15 ml HCL (hydrochloric), 10 ml Acetic acid and 10 ml HNO_3 (nitro acid) for 35 seconds.
4. Inconel 718 specimens were also immersed in fresh mixed acid 15 HCL (hydrochloric), 10 ml Acetic acid and 10 ml HNO_3 (nitro acid) for 20 seconds.
5. Afterwards ethanol was used to clean the surface which was then dried using hot air ready for microstructure analysis.

The Inconel 718 specimens were initially etched for 35 seconds for LOM analysis, but it appeared to be over-etching, as noted by the colour tint on the surface and the darkening and deepening of the grain boundaries. Therefore, the polishing process steps were repeated and re etching took place for a short etching time of 20 seconds to achieve clearer microstructure on the surface.

Note that it is best to etch freshly polished samples: mixed acids etchant is only usable for 30 minutes after mixing before it denatures. It cannot be stored and must be discarded. PPE is required and the mixing of etchants and etching must be done in the fume hood.

The particular etching fluid for nickel-based superalloys used for this particular specimens has the effect of changing the reflexion behavior of the integral crystalline component so that an optical difference is possible (ASM, 1985 and Vander Voort, 2003).

5.4 Microstructural Investigation

In this study, SEM and LOM were used for microstructure characterization of Inconel 625 and 781 sample specimens. According to Humphreys (1999), the application of quantitative metallography to SEM mainly focuses on particle size, chemical analysis and volume fraction analysis. In the case of LOM analysis work is concentrated on the application of fundamental stereoscopically based fundamentals principles application. The reason for the difference in, SEM and LOM lies in the strength and weakness of each instruments. The high magnification and chemical analysis of SEM analysis is ideal for identifying fine particles, while LOM image analysis is influenced by the material being tested where phase movement and focusing can be analysed (Vander Voort, 2012).

5.4.1 SEM (Scanning Electron Microscope)

SEM analysis of all samples was carried out on the Tescan Mira 3 at the University of Cape Town which is a 30 kV device with resolution of up 12 nm as illustrated in Figure 5.8. The Tescan Mira 3 machine is equipped with a secondary electron detector and a backscattered electron detector for normal imaging. The working distance of 10.12 mm was generally used during analysis at a scale of 50 μm and 1.00 kx. Backscattered electron images were collected at a working distance that could be adjusted up to 30 mm. Accelerating voltage at a rate of 20 kV was used to bring out certain features on the sample specimen surface or from slightly below the surface with a field view of 208 μm. EDX (energy dispersive x-ray) was used to identify chemical elements within the samples while a filament current ranging between 70 and 80 μA was generally used.

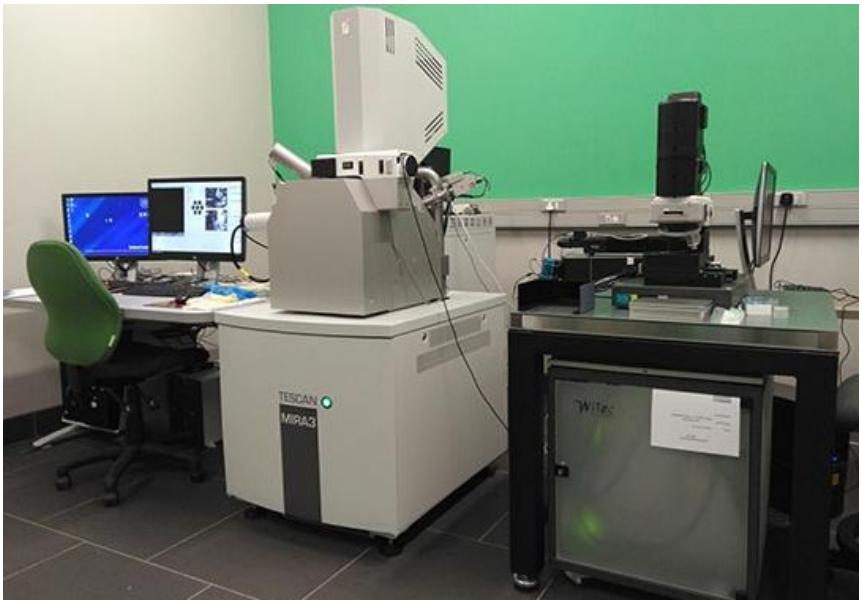

Figure 5.8: SEM (scanning electron microscope) connected with EDX (energy dispersive X-ray)

5.4.2 LOM (Light Optical Microscope)

LOM analysis was carried out on the Motic cam 1080BMH equipped with Motic software plus 30ML for image analysis at CPUT). This machine has a spatial resolution of 2.8 μm and focusable lens of 12 mm with a 1920x1080 high resolution monitor illustrated in Figure 5.9. The LOM is the most common and basic instrument for analysing surface microstructures in sample specimens.

Figure 5.9: LOM (light optical microscope)

5.5 X-Ray Diffraction Test

The technique for X-ray crystallography has three steps (illustrated in Figure 5.10)

1. The initial step is to locate the crystal in the sample specimen. The crystal found should be at least 0.1mm, regular in structure and pure in composition with no major inner limitations such as twinning or cracks.
2. In the following step the crystals are placed in an intense beam of X-rays. The intensities and angles of diffracted X-rays are measured with each compound having a special diffraction pattern.
3. The data are combined computationally, combining chemical information from step 1 and 2 to refine and analyse the arrangement of atoms within the crystal of each sample specimen.

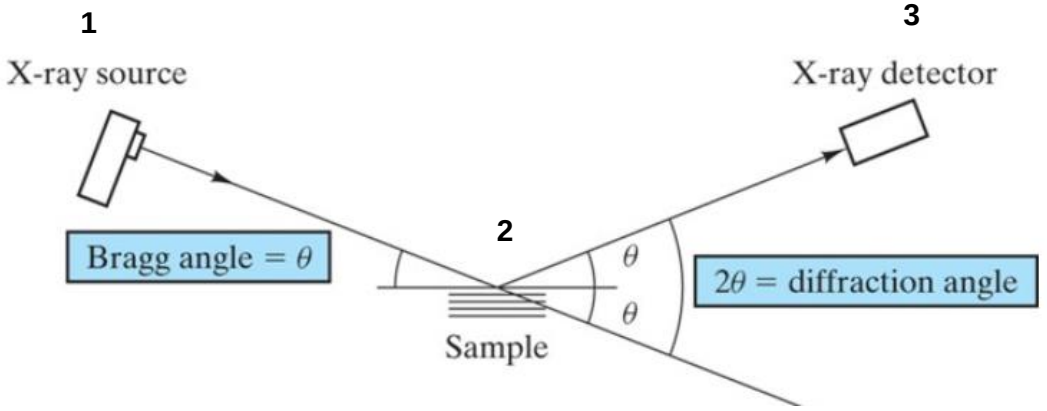

Figure 5.10. Relationship of Bragg angle θ and the experimentally measured diffraction angle 2θ (Moris, n. d)

5.5.1 Micro Element Determination

The 1st peak for crystal structure was used to determine the micro elements Inconel 625 and 718 for each specimen during XRD analysis. Three relatively simple crystal structures were found for most of the common, FCC, BBC and SC metals.

Interplanar spacing or D-spacing

The D-spacing or the lattice spacing or inter-atomic spacing is the distance between the parallel planes of atoms, the minimum distance between two planes.

$$d_{hkl} = \frac{a}{\sqrt{h^2 + k^2 + l^2}} \quad (13)$$

d = interplanar spacing, hkl = Miller indices notation system (first peak indices),

a = lattice value

According to ARC (n.d), Miller indices are vectors which represent directions and planes. The planes are determined by three integers namely h, k and l. The number of indices will be 1 index equals 1 dimensional, 2 indices equals two dimensional and 3 indices equal three dimensional, therefore the indices will match the dimension lattice.

Representation notation summary of brackets for Millller indices:

[hkl] direction, <hkl> family of directions, (hkl) plane and {hkl} family of planes

Lattice value for FCC dimension of unit cells in a crystal lattice

$$a = \frac{4R}{\sqrt{2}} \qquad (14)$$

a = lattice value, R = atomic radius

Unit cell Volume for FCC (coordination number of 12 and contains 4 atoms per unit cell)

Total FCC sphere volume

$$V_s = 4\pi R^3 = \frac{16}{3}\pi R^3 \qquad (15)$$

V_s = sphere volume, R = atomic radius

Total unit cell volume

$$V_c = 16\pi R^3 \qquad (16)$$

V_c = unit cell volume, R = atomic radius

APF (Atomic packing factor) for FCC

$$APF = \frac{V_s}{V_c} = \frac{\frac{16}{3}\pi R^3}{16\pi R^3} = 0.74 \qquad (17)$$

CHAPTER 6

6.0 Experimental Results

6.1 Microstructural and sample chemical identification results

As mentioned, in section 5.4, four samples specimen two were of Inconel 625 and 718, parallel and perpendicular to the build directions with different microstructures were characterised made possible with SEM and LOM analysis at room temperature $20^{0}C$.

6.1.1 SEM (Scanning Electron Microscope) Results

The polished samples were made conductive using coating to enable or improve the imaging of samples; thermal damage will be reduced if the correct amount of coating is applied. The undercoating process improves secondary electron during analysis as, illustrated in Figure 6.1. Micrographs of sample specimens Inconel 625 and Inconel 718 both parallel and perpendicular to the building direction illustrated in Figures 6.2 and 6.3 grain and grain boundaries denoted with arrows.

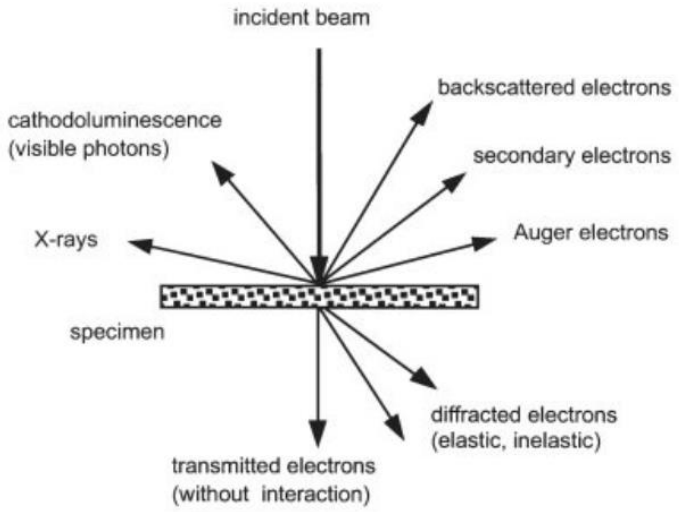

Figure 6.1: Interactions between incident beam and a specimen in a SEM (scanning electron microscope) analysis (Karlik, 2001)

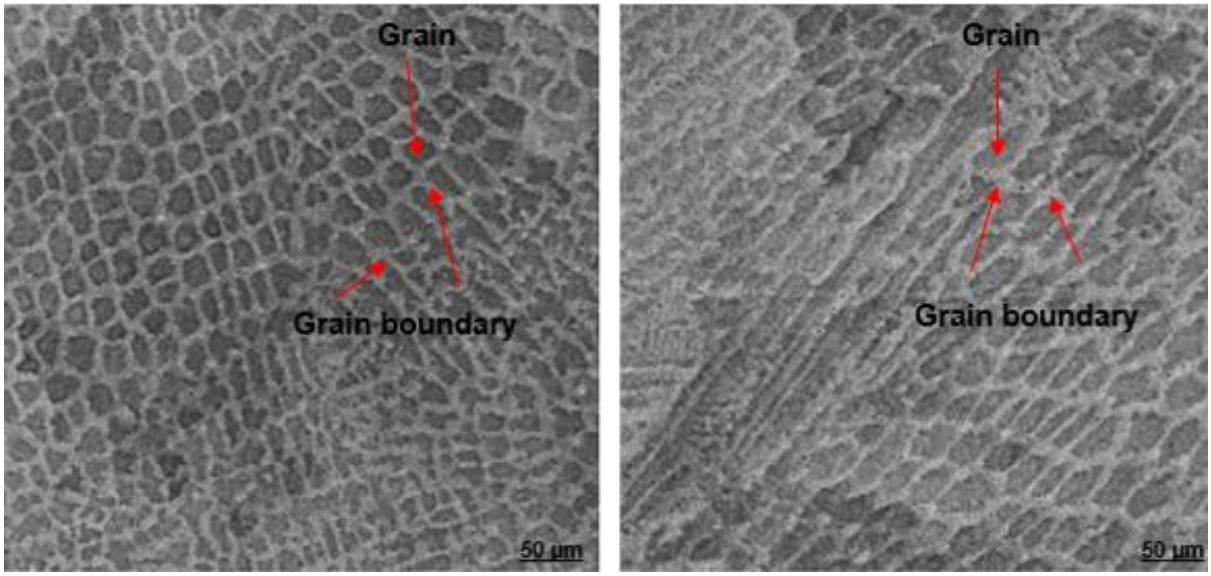

(a) 625 Parallel (b) 625 Perpendicular

Figure 6.2: SEM (scanning electron microscope) Micrograph of Inconel 625

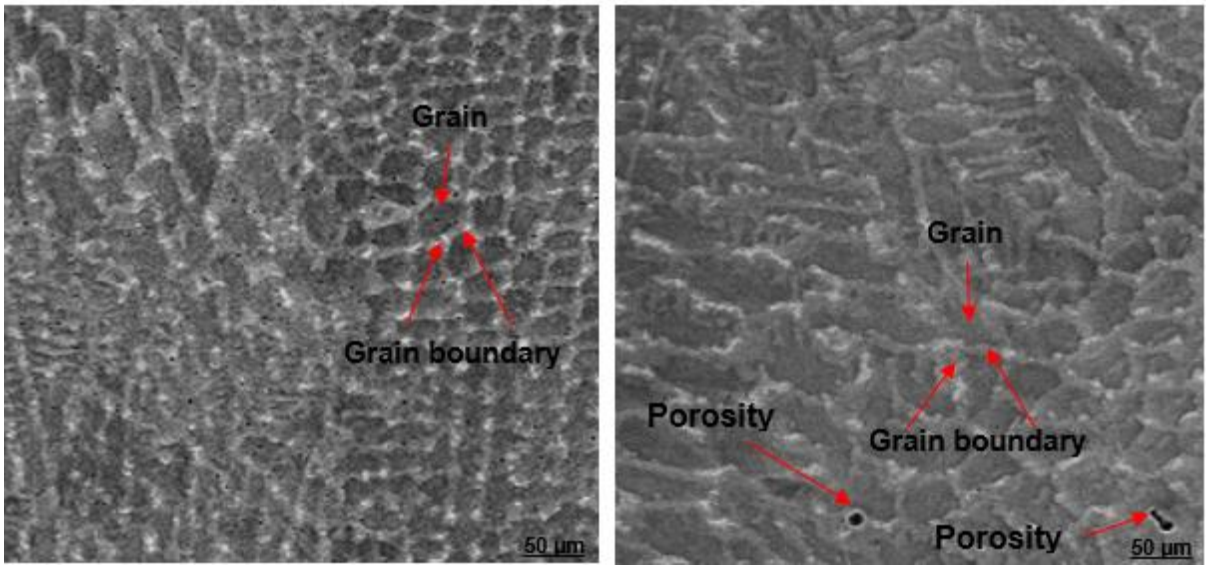

(a) 718 Parallel (b) 718 Perpendicular

Figure 6.3: SEM (scanning electron microscope) Micrograph of Inconel 718

The differences in grain size of sample specimens shown by SEM analysis, show that the grains had a preferred growth direction. Average grain size of both specimens Inconel 625 and 718 perpendiculars is larger than both specimens 625 and 718 parallel illustrated in Figures 6.2 and 6.3. This indicates the preferred grain growth direction of these additive manufactured samples is aligned to the building direction, means that grains are smaller in the direction of the laser motion. This indicates that there may be a connection between crystallographic orientation and mechanical properties (Petersen-Overleir, 2015). The grain orientation of Inconel 625 parallel and perpendicular in Figure 6.4 (a) parallel and (b)

perpendicular illustrated the grain has texture meaning it has a preferred direction. The grain orientation of Inconel 718 in Figure 6.5 (a) parallel and (b) perpendicular show that the grain has random texture, meaning no preferred direction. According to Petersen-Overleir (2015), material with smaller grain size increases tensile strength and may increase ductility, while material with larger grain size improves high temperature creep properties.

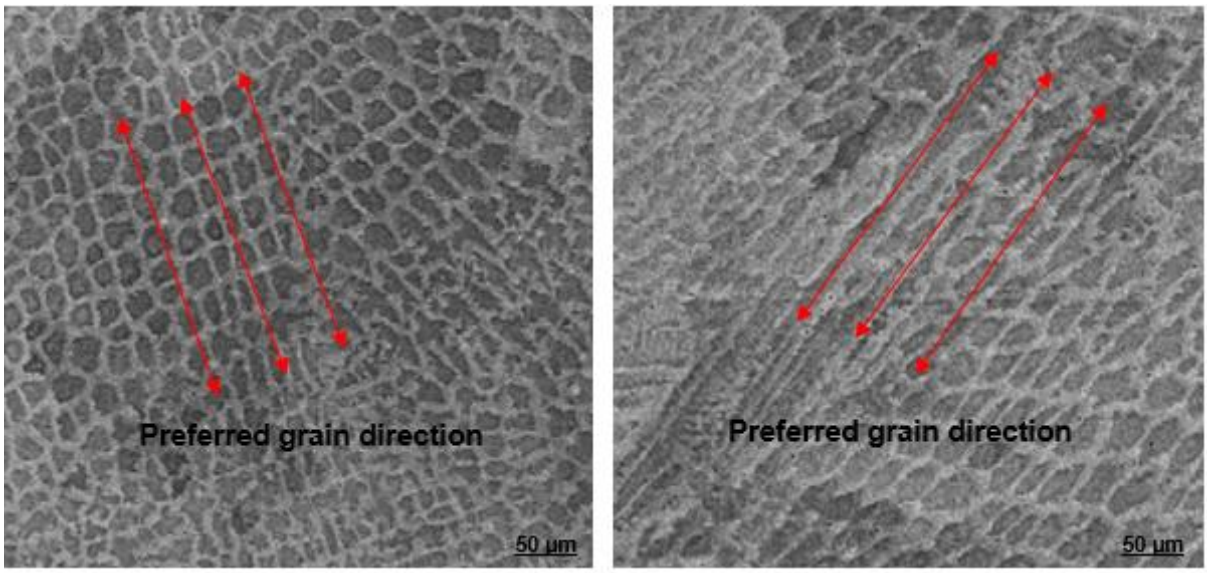

(a) 625 Parallel (b) 625 Perpendicular

Figure 6.4: Micrograph of Inconel 625 with preferred grain direction denoted with arrows

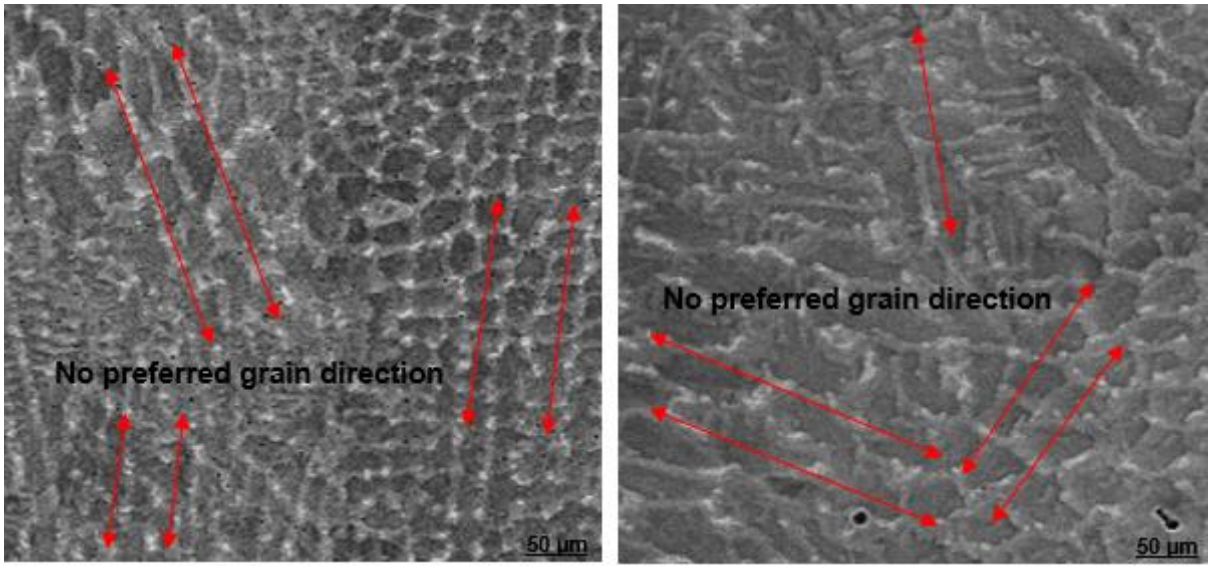

(a) 718 Parallel (b) 718 Perpendicular

Figure 6.5: Micrograph of Inconel 718 with no preferred grain direction denoted with arrows

6.1.2 LOM (Light Optical Microscope) Results

LOM (Optical Light Microscope) micrograph of Inconel 625 and 718 additive manufactured sample specimens illustrate a good understanding of the 3D printing process for layer by layer orientation. Unfortunately, no grain structure or minimal was shown, but porosity is revealed was micrographs of Inconel 625 and 718. LOM analysis was conducted to illustrate the layers formed during 3D SLM process.

Figure 6.6 shows Inconel 625 perpendicular to the building direction. The laser melted track layers are visible in the scanning pattern, and individual melt pool boundaries can be seen where the two tracks meet. There are overlaps in between tracks which are caused by the laser movement which forms each layer during the laser movement and building process layer by layer. These overlaps in each layer may be considered high stress regions because the overlaps formed face rapid reheating and solidification.

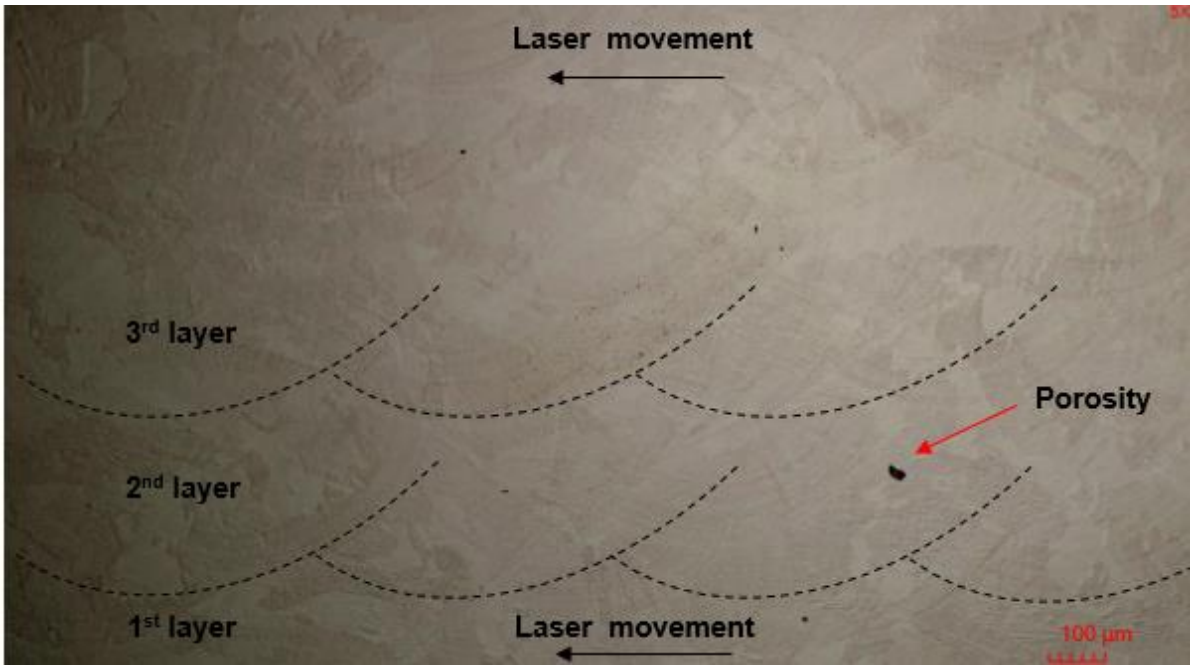

Figure 6.6: LOM (light optical microscope) Micrograph of Inconel 625 perpendicular to the building direction

According to Anam (2018), there are two main types of pores in 3D SLM: gas entrapment pores generally rounded in shape, and lack of fusion pores with linear and sharp angled cracks between layers. Micro pores with small spherical shapes and irregular shape were observed in samples of Inconel 718 both parallel and perpendicular to the build direction illustrated in Figure 6.5 (b) Inconel 718 perpendicular. In samples of Inconel 625 both parallel and perpendicular only small spherical porosity was observed during SEM analysis. The spherical porosity was possibly caused by gas in the powder bed that might have been entrapped by

the high cooling rate. A lack of fusion pores occurs when the molten pool cannot fully encompass the spaces intended to be melted thus leaving a thin flat crack perpendicular to the build direction or between neighbouring tracks (Anam, 2018). The spherical pores may cause less damage to mechanical properties of components being additively manufactured (Deng, 2018). According to Caroll et al. (2015), the tips of irregular shaped pores may introduce local stress during loading and result in early fracture or failure of parts especially for the side perpendicular to the build direction.

Both types of porosity can be reduced by carefully selecting the process parameters. The proper scan speed, scan pattern and laser power, can be chosen to have a melt pool to melt at least 2-3 layers of the substrate to avoid the keyhole effect (Anam, 2018).

6.2 EDX (Energy Dispersive X-Ray) Results

The mechanical properties, corrosion resistance and metal microstructure depends on the different elements from which an alloy is made. The primary alloy elements for nickel-based alloys are Ni, M and Fe, but other elements like W, C, Al, Ti, Cu and S may be minimal but have significant effects. The understanding of chemical elements is important as well as the positive and negative effect of each chemical element which may be of help to identify the application and effect in certain alloys.

The following results can be drawn for this analysis to quantify the chemical composition of the samples illustrated in Tables 6.1 – 6.4. The average of each sample chemical composition was determined by analyzing different sections of each sample's denoted from spectrum 1 to 5 as shown in Figures 6.7- 6.10.

6.2.1 EDX (Energy Dispersive X-Ray) Inconel 625 Results

Table 6.1: Chemical composition impurities of Inconel 625 parallel in weight percentage at room temperature $20^{0}C$

Spectrum	C	Si	Cr	Fe	Ni	Nb	Mo	Total
Spectrum 1	6.29	0.52	21.58	4.14	58.8	-	8.67	100
Spectrum 2	6.96	0.54	20.39	3.92	55.16	3.4	9.64	100
Spectrum 3	6.22	0.43	20.62	4.16	55.97	3.2	9.4	100
Spectrum 4	6.2	0.54	20.43	4.05	55.74	3.55	9.48	100
Spectrum 5	6.63	0.45	20.54	4.19	55.56	3.24	9.39	100
Average	**6.46**	**0.496**	**20.712**	**4.092**	**56.246**	**3.3475**	**9.316**	**100**

C (Carbon), Si (Silicon), Cr (Chromium), Fe (Iron), Ni (Nickel), Nb (Niobium) and Mo (Molybdenum)

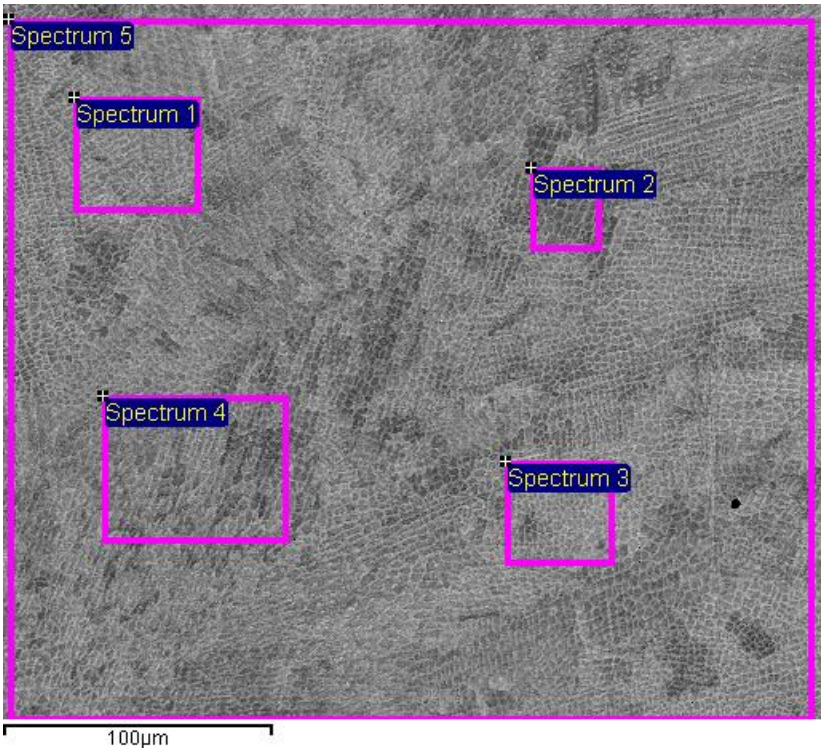

Figure 6.7: EDX (energy dispersive X-ray) analysis of Inconel 625 parallel to building direction

Table 6.2: Chemical composition impurities of Inconel 625 perpendicular in weight percentage at room temperature $20^{0}C$

Spectrum	C	Si	Cr	Fe	Ni	Nb	Mo	Total
Spectrum 1	6.49	0.51	20.79	3.35	56.08	3.33	9.46	100
Spectrum 2	6.24	0.5	20.94	3.01	55.91	3.79	9.62	100
Spectrum 3	7.27	0.51	20.7	2.98	55.76	3.33	9.45	100
Spectrum 4	6.53	0.61	20.56	3.12	55.95	3.52	9.73	100
Spectrum 5	7.14	0.64	20.6	3.16	55.73	3.29	9.42	100
Average	**6.73**	**0.55**	**20.72**	**3.12**	**55.89**	**3.45**	**9.54**	**100**

C (Carbon), Si (Silicon), Cr (Chromium), Fe (Iron), Ni (Nickel), Nb (Niobium) and Mo (Molybdenum)

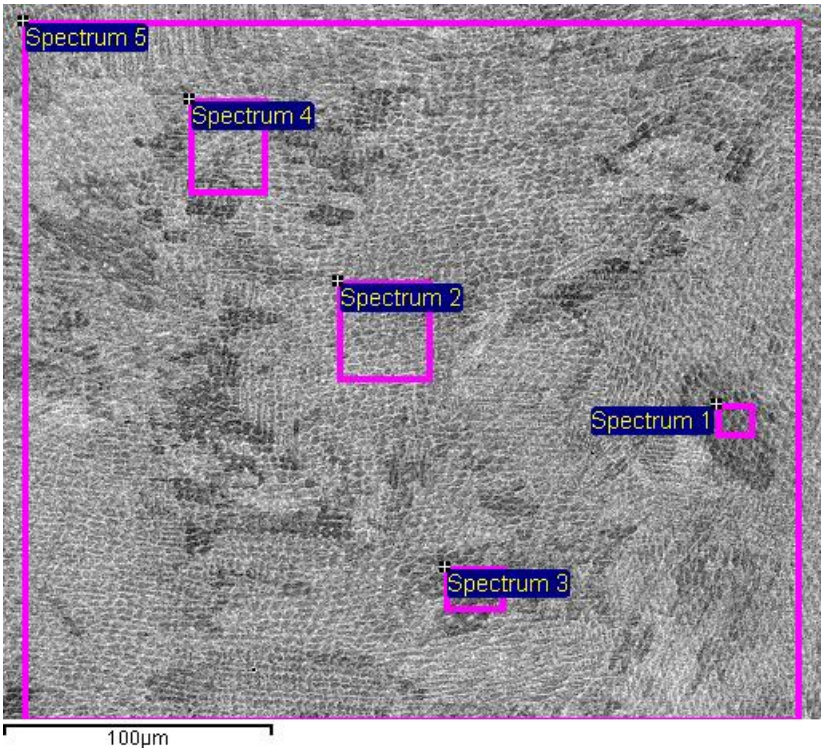

Figure 6.8: EDX (energy dispersive X-ray) analysis of Inconel 625 perpendicular to building direction

The main focus was to determine if the samples analysed were predominantly Ni and Cr and Mo chemical elements, and the contribution of the other elements was minimal. The other chemical elements might have been minimal but would still have an effect on the properties mentioned in Tables 6.1 and 6.2. The results of both samples parallel and perpendicular in Tables 6.2 and 6.2 confirm a combined average of 56.07% Ni, 20.72% Cr and 9.43% Mo chemical elements are indeed prominent in both samples. Ni-Mo-Cr (nickel-molybdenum-chromium), alloy in this category is known for its high strength despite high temperatures and corrosive environments. Histology B which is part of the Nickel alloys is known for its creep and rupture strength and Ni-Cr containing about 15% Cr improve both carburization and oxidation resistance at temperatures greater than $760^{0}C$ (JLCElectromet, 2017).

6.2.2 EDX (Energy Dispersive X-Ray) Inconel 718 Results

Table 6.3: Chemical composition impurities of Inconel 718 parallel in weight percentage at room temperature $20^{0}C$

Spectrum	C	Al	Ti	Cr	Fe	Ni	Nb	Mo	Total
Spectrum 1	5.07	0.61	0.96	17.98	19.13	47.32	5.66	3.26	100
Spectrum 2	6.38	0.63	1.01	17.87	19	46.34	5.42	3.37	100
Spectrum 3	6.14	0.69	1.05	17.76	18.56	46.9	5.89	3	100
Spectrum 4	5.75	0.62	1.02	17.88	19.28	46.33	5.69	3.42	100
Spectrum 5	5.83	0.66	0.89	18.1	19.09	46.3	5.65	3.49	100
Average	**5.83**	**0.64**	**0.99**	**17.92**	**19.01**	**46.64**	**5.66**	**3.31**	**100**

C (Carbon), Al, Ti (Titanium), Cr (Chromium), Fe (Iron), Ni (Nickel), Nb (Niobium), and Mo (Molybdenum)

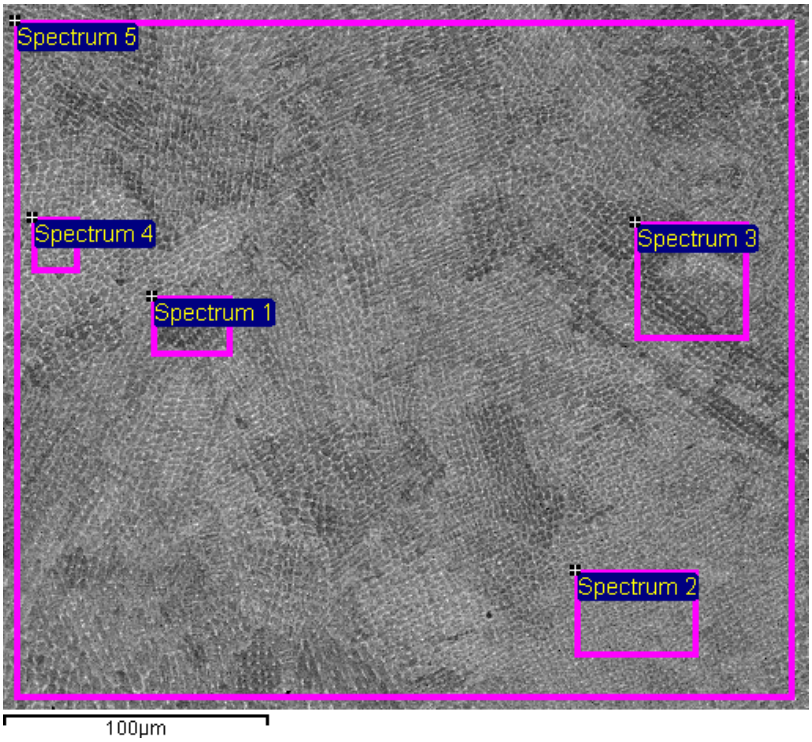

Figure 6.9: EDX (energy dispersive X-ray) analysis of Inconel 718 parallel to building direction

Table 6.4. Chemical composition impurities of Inconel 718 in weight percentage at room temperature $20^{0}C$

Spectrum	C	Al	Ti	Cr	Fe	Ni	Nb	Mo	Total
Spectrum 1	6.83	0.47	0.91	18.04	16.73	47.91	5.88	3.23	100
Spectrum 2	5.99	0.64	0.9	18.13	16.83	48.5	5.82	3.19	100
Spectrum 3	7.15	0.58	1.13	18.11	16.85	47.11	5.45	3.62	100
Spectrum 4	6.87	0.64	1.03	17.82	16.59	47.27	5.94	3.83	100
Spectrum 5	6.33	0.58	0.91	18.4	16.58	48.16	5.75	3.29	100
Average	**6.64**	**0.58**	**0.98**	**18.1**	**16.72**	**47.79**	**5.77**	**3.43**	**100**

C (Carbon), Al, Ti (Titanium), Cr (Chromium), Fe (Iron), Ni (Nickel), Nb (Niobium) and Mo (Molybdenum)

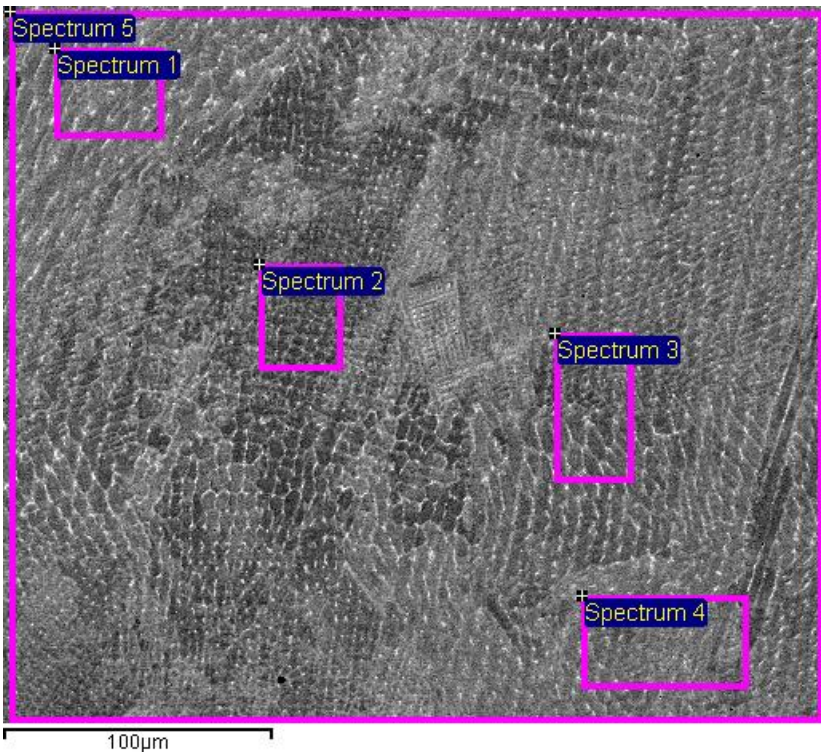

Figure 6.10: EDX (energy dispersive X-ray) analysis of Inconel 718 perpendicular to building direction

As mentioned above in conclusion for Inconel 625 the same focus applies for Inconel 718 samples, to determine which chemical elements was prominent. Ni(Nickel), Cr and Fe (Iron) chemical elements was prominent the contribution of the other elements was minimal. The other chemical elements maybe minimal but also has a roll and effect on the properties mentioned in Tables 6.3 and 6.4. The results of both parallel and perpendicular in Tables 6.3 and 6.4 confirm that with a combined average of 47.23% nickel, 18.01% chromium and

17.87% iron chemical elements are indeed prominent in both samples. According to JLCElectromet (2017), Ni-Cr-Fe alloys add high resistance to oxidation at temperatures up to 1000 ^{0}C, and also provides resistance against stress corrosion in marine environments. Furthermore, Ni-Cr-Fe alloy offers good mechanical properties and workability at high temperature which is ideal in the aerospace industry.

Effect of alloying elements prominent in both additive manufactured Inconel 625 and 718 in this research (Corrosion Materials, 2019)

Nickel (prominent in both 625 and 718)

- Improves high temperature strength and resistance to oxidation
- Provides metallurgical stability
- Improve resistance to stress corrosion cracking

Chromium (prominent in both Inconel 625 and 718 sample specimens)

- Improves resistance to higher temperature oxidizing and, sulfidation

Molybdenum (prominent in Inconel 625 sample specimen)

- Improves the resistance to non-oxidizing hydrofluoric phosphoric and hydrochloric acids
- Improves high temperature strength and resistance corrosion

Iron (prominent in Inconel 718 sample specimen)

Improves and controls thermal expansion and high temperature carburizing resistance

6.2.3 EDXS (energy dispersive x-ray spectrum) Inconel 625 and 718 Results

Two basic types of X-rays are produced on inelastic interaction of the electron beam with the specimen atoms in the SEM (Hafner, n.d). The EDX of Inconel specimens 625 and 718 parallel and perpendicular to the build direction in Figures 6.11 - 6.14 illustrated both characteristic X-rays and continuum X-rays at room temperature of 20 ^{0}C. According to Hafner (n.d), characteristic X-rays occur when the beam electron ejects inner electrons of the sample specimen's atoms, and interaction between the beam electron and nucleus of the sample specimen atoms results in a continuum X-ray peak. According to Koncar (2018), the characteristic X-rays evolve from continuum X-rays and imposed in the background X-rays are illustrated in Figures 6.11 - 6.14. These peaks are specific to an atom and match each

element: the higher a peak reaches the more concentrated the element is in each sample specimen. EDXS analysis not only identifies the corresponding element but the X-ray to which it corresponds as well (EESEM, 2001).

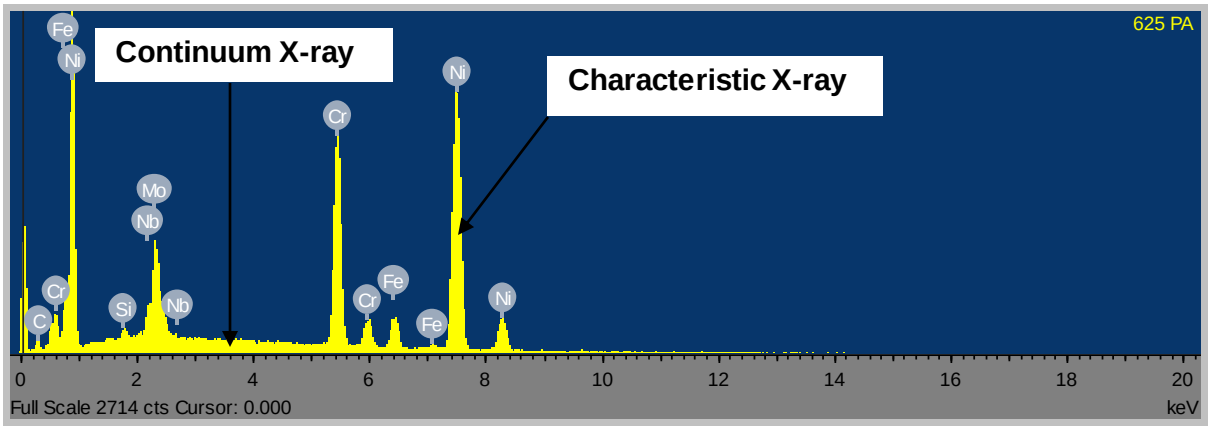

Figure 6.11: EDXS (energy dispersive X-ray spectrum) Inconel 625 parallel spectrum with characteristic and continuum X-ray denoted with arrows

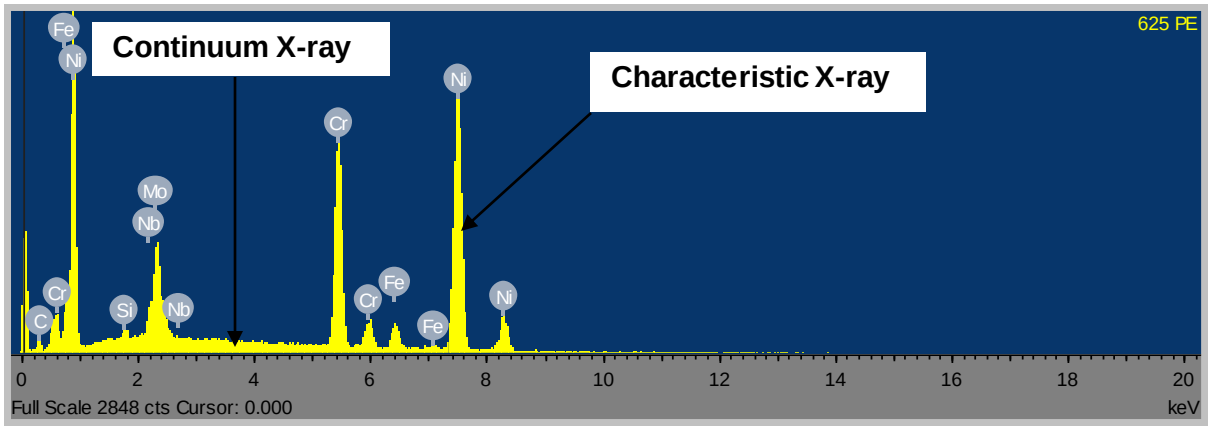

Figure 6.12: EDXS (energy dispersive X-ray spectrum) Inconel 625 perpendicular with Characteristic and Continuum X-ray denoted with arrows

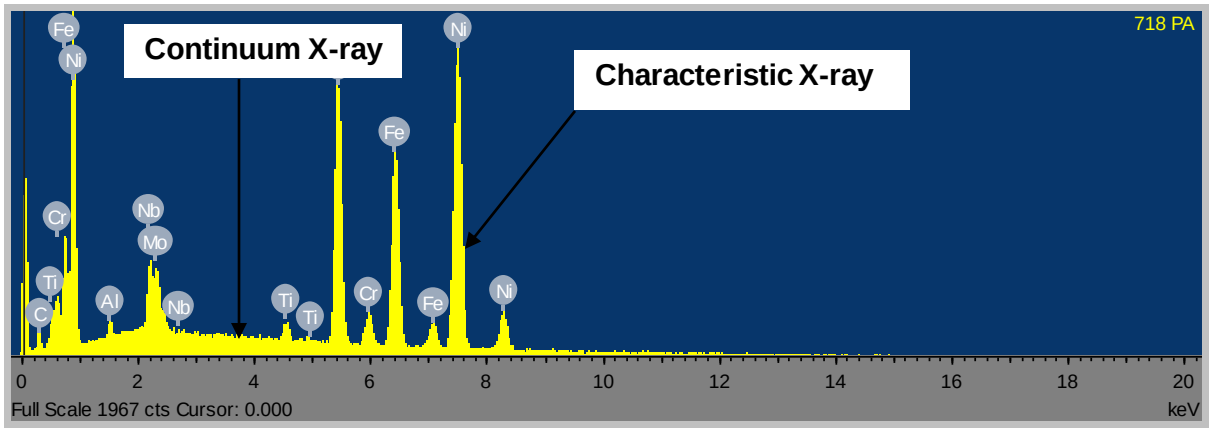

Figure 6.13: EDXS (energy dispersive X-ray spectrum) Inconel 718 parallel spectrum with characteristic and continuum X-ray denoted with arrows

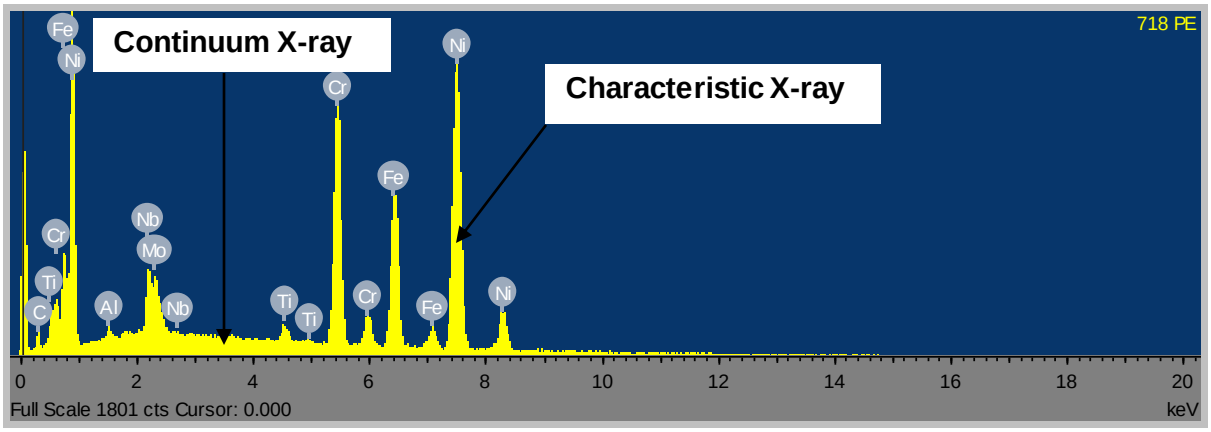

Figure 6.14: EDX (energy dispersive X-rayspectrum) Inconel 718 perpendicular with Characteristic and Continuum X-ray denoted with arrows

It can be concluded that these samples analysed, additive manufactured Inconel 625 and 718, both fall in the percentage range based on the comparison with ASTM F3065 – 14E1 Standard Specification for Additive Manufacturing Nickel Alloy (UNS N06625) with Powder Bed Fusion for Inconel 625, illustrated in Table 2.2 (AMS Inconel 625 table); and ASTM F3055-14a – Standard Specification for Additive Manufacturing Nickel Alloy (UNS N07718) with Powder Bed Fusion illustrated in Table 2.3 (AMS Inconel 718 table) for Inconel 718.

6.3 Hardness Test Results

For each sample a load of $10\,kg$ and dwell time of $\pm$ 10 second was applied at room temperature. No less than 6 indentations were performed to obtain good results. The results from the hardness testing are presented in Tables 6.5 and 6.6.

Table 6.5: Hardness and yield strength value for each position value of Rockwell test for Inconel 625 polished parallel and perpendicular to the building direction at room temperature $20^{0}C$

Test	Inconel 625 // Parallel		Inconel 625 ⊥ Perpendicular	
	HR_B	Yield Strength (MPa)	HR_B	Yield Strength (MPa)
1	95.9	720	104.3	900
2	100.5	812	100.6	835
3	99.6	800	96.3	729
4	98.5	770	102.6	875
5	98.9	790	104.0	900
6	99.5	800	102.0	865
Average	**98.82**	**782**	**101.6**	**851**

Table 6.6: Hardness and Yield Strength value for each position of value Rockwell test for Inconel 718 polished parallel and perpendicular to the building direction at room temperature $20^{0}C$

Test	Inconel 718 // Parallel		Inconel 718 ⊥ Perpendicular	
	HR_B	Yield Strength (MPa)	HR_B	Yield Strength (MPa)
1	97.1	755	95.9	720
2	101.2	840	100.5	830
3	101.7	860	99.6	800
4	95.8	720	98.5	785
5	100.8	835	98.9	790
6	101.8	865	99.5	800
Average	**99.73**	**812.5**	**98.82**	**787.5**

The average HR_B (Rockwell hardness B) value for Inconel 625, both parallel and perpendicular to the build direction, leads to the conclusion that the perpendicular direction has a slightly higher hardness value compared to parallel HR_B (Rockwell hardness B) 101.6 perpendicular greater than HR_B parallel 98.82. In hardness statistics terms, the difference between 101.6 and 98.82 in hardness terms is very small. The average HR_B value for Inconel 718 both parallel and perpendicular to the building direction leads to conclusion that parallel to build direction is slightly higher in hardness compared to HR_B 99.73 parallel is greater than HR_B 98.82 perpendicular. The same applies for 99.73 and 98.82 is super small, if standard deviation or error bars were used, it could have shown an overlap on hardness values.

6.4 Three-point Bending Test Results

Table 6.7: Experimental bending test properties on Inconel 625 and 718 specimens parallel to the build direction at room temperature 20^0C

Specimen	Max Load (kN)	Bending Strength (MPa)	Deflection (mm)	Bending Strain
625	10.78	2125.4	7.674	0.22
718	5.09	2029.95	5.193	0.14

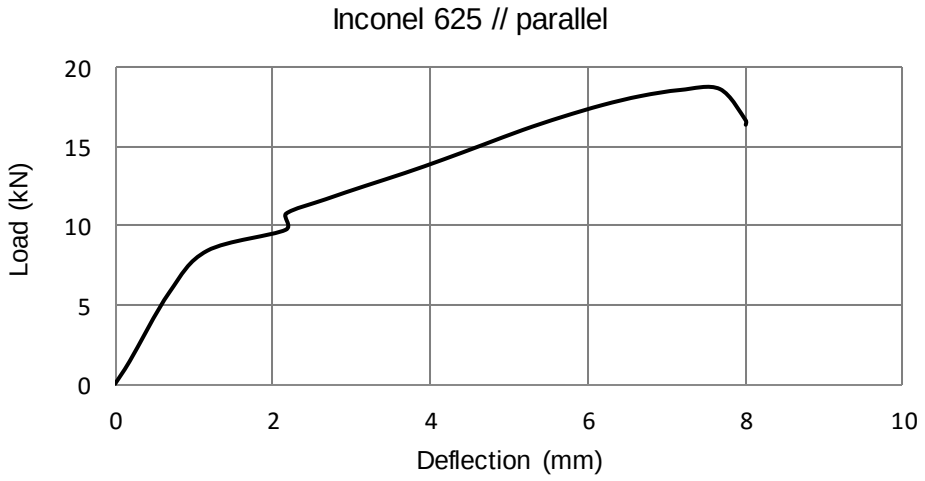

Figure 6.15: Force vs deflection response of Inconel 625 sample specimen parallel to building direction

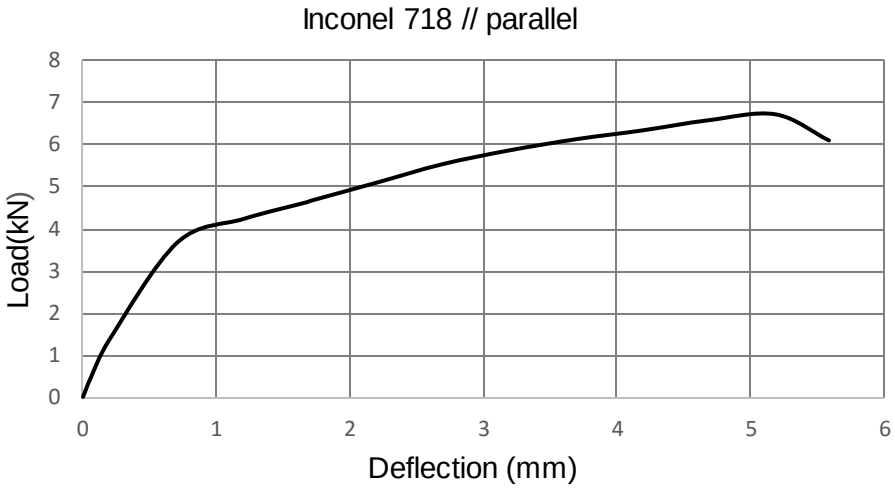

Figure 6.16: Force vs deflection response of Inconel 718 sample specimen parallel to building direction

The aim of the study was to investigate the bending strength of additive manufactured material with selective laser melting on Inconel 625 and 718. A three-point bending test was conducted on Inconel 625 and 718 samples specimens. Table 6.7 above illustrates the maximum load of 10.87 kN applied to Inconel 625 with max deflection of 7.674 mm and bending stress σ_f of 2125,4 MPa (illustrated in Figure 6.15); and bending strain of ε_f 0.22, and Inconel 718 with a maximum load of 5.193 kN and bending stress σ_f of 2029.95 MPa and bending strain ε_f of 0.14 (illustrated in Figure 6.16). Both specimens neither yields nor breaks before the 5 % strain limit, as illustrated in Figure 4.13 (note curve 'C' of bending stress vs bending strain).

6.4.1 The Correlation between Brinell and Rockwell Hardness Tests

Although the HB (Brinell) and HR (Rockwell) hardness methods are based on different parameters, both measure hardness and there is correlation between them. There is a linear relationship between HB and HR hardness. The hardness test results for both Inconel 625 and 781 sample specimens were determined with HR_B. The average HR_B $\perp$ for Inconel 625 is 101.6 and average HR_B $\perp$ for Inconel 718 is 98.82, as illustrated above in table 6.5 and 6.5 . According to Horath (1995), the relationship between HB Brinell and HR Rockwell hardness for HR_B Rockwell hardness scale 'B' values which fall between 35 and 130 can be determined by equation (18). The converting values should fall in the defined hardness range; due to inaccuracies the conversion value should be rounded off to the nearest whole number in accordance with practical experimental standard E29 of the American Society of Microbiology.

Relationship between HB and HR hardness for HR_B Rockwell hardness scale 'B' values

$$HB = \frac{7.3\times10^3}{130 - HR_B} \tag{18}$$

Inconel 625 sample specimen with average HR_B of 101.6

$$HB = \frac{7.3\times10^3}{130-101.6} \tag{19}$$

$$HB = 257.042$$

$$HB \approx 257\,(Approximate\ \ Brinell\ \ \ hardness)$$

Inconel 718 sample specimen with average HR_B of 98.82

$$HB = \frac{7.3\times10^3}{130-98.82} \tag{20}$$

$$HB = 234.124$$

$$HB \approx 234\ \ (Approximate\ \ Brinell\ hardness)$$

These results can also be read from approximation hardness conversion relations of number HR_B and HRc vs the HB number illustrated in Figure 6.17: note that HB for Inconel 625 sample specimen 234 and for Inconel 718 sample specimen 257 is denoted with arrows. According to ASM (1997), Hardness Test ASTM E-140-12b the approximation conversion numbers for nickel and high nickel alloys, HB value of 101.6 equal 257 and the HR_B value of 98.82 equal 234 HB.

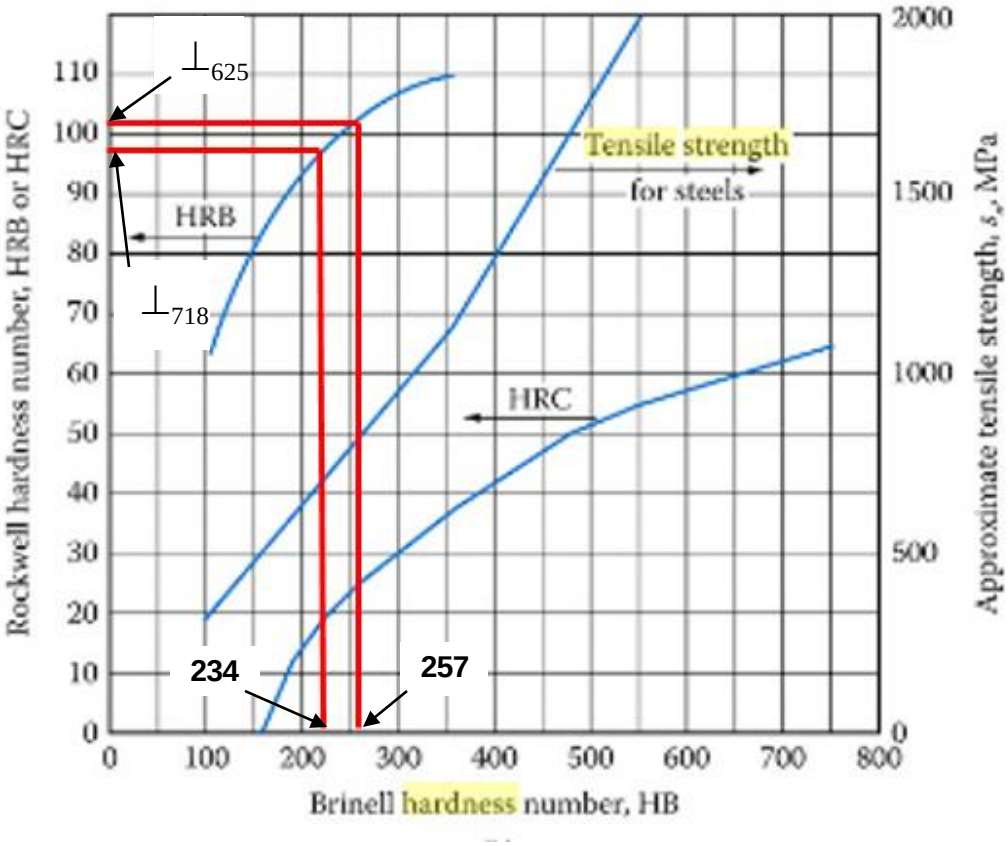

Figure 6.17: Hardness conversions and relations to steel strength for steel (Mott and Untener, 2018)

6.4.2 The Correlation between Bending, Tensile and Hardness Test Values

The approximation bending strength σ_f evident in the experimental bending test result for the sample specimen of Inconel 625 was 2225,4 MPa and for the sample specimen Inconel 718 it was 2029 MPa, as illustrated in Figure 6.15 and 6.16. The correlation between three point bending test σ_f and tensile test σ_{uts} ($\sigma_f = \sigma_{uts}$) for the same specimen cross section areas and bending modulus E_f and Young's modulus E ($E_f = E$) depended on the test speed illustrated in Figure 5.1. The approximation relationships between HB, tensile strength σ_{uts} and bending strength σ_f for both sample specimens are calculated below.

Approximation for sample specimen Inconel 625

$$\begin{aligned} \sigma_f &= HBk = \sigma_{uts} \\ 2225.4 &= 257.402k \\ k &= 8.628\,(conversion\ factor) \\ 8.628HB &= \sigma_{uts} = \sigma_f \end{aligned} \tag{21}$$

Approximation for sample specimen Inconel 718

$$\begin{aligned} \sigma_f &= HBk = \sigma_{uts} \\ 2029.95 &= 234.124k \\ k &= 8.349\,(conversion\ factor) \\ 8.349HB &= \sigma_{uts} = \sigma_f \end{aligned} \tag{22}$$

From the above calculation, using the average of $8.628HB$ for Inconel 625 and $8.349HB$ for Inconel 718, the approximate relationship between Brinell hardness, tensile strength and bending strength for experiment sample specimen Inconel 625 and Inconel 718 can be written as $8.49HB$. The correlation equation can be written as $\sigma_{uts} = 8.49HB = \sigma_f$ for this experimental between bending strength σ_f, tensile strength σ_{uts} and hardness test. These approximate relationships may be used for estimates with $\pm$ 5% difference.

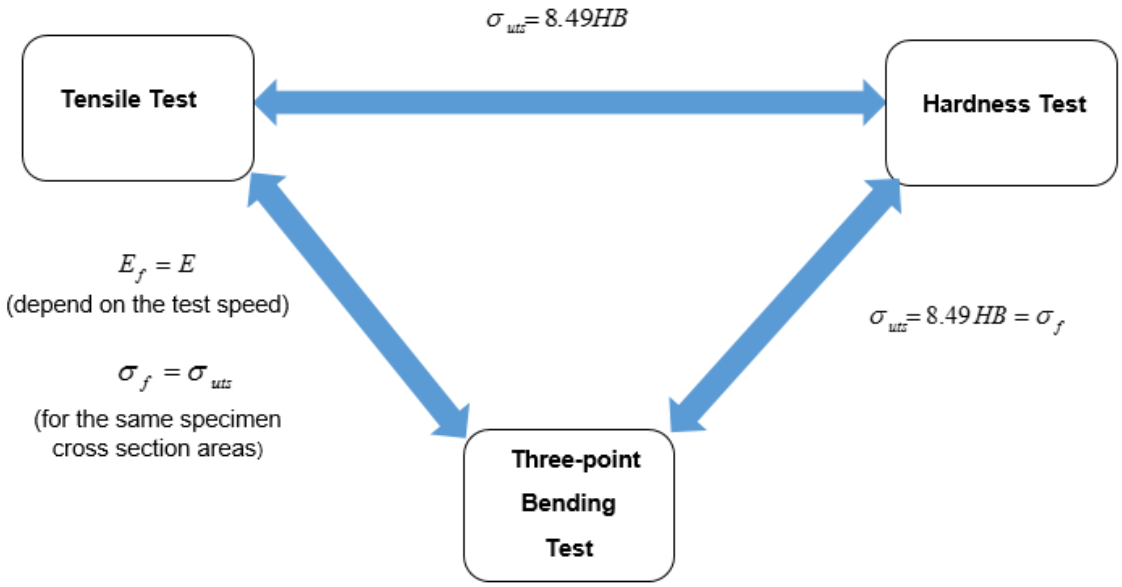

Figure 6.18: The approximate correlation between bending, tensile and hardness test values

For most of traditionally manufactured Inconel 625 and 718 the hardness results were determined using Brinell hardness. The experimental approximation Brinell hardness results samples of Inconel 625 and 718, for this research is compared with traditionally manufactured Inconel 625 and 718, as illustrated in Tables 6.8 and 6.9.

Table 6.8: Experimental approximation Brinell hardness results compared to traditionally manufactured Inconel 625 at room temperature $20^{0}C$ (Adapted from aircraft materials, 2013 and special metals, 2013)

Form and Condition	Orientation //(Parallel)	HB (Brinell hardness)
Sample 625 (Flat Bar)	//	257
Rolled (Flat Bar)	-	175-200
Solution Treated (Bar)	-	287
Solution Treated (Flat Bar)	-	116-194

Table 6.9: Experimental approximation Brinell Hardness results compared to traditionally manufactured Inconel 718 at room temperature $20^{0}C$ (Adapted from aircraft materials, 2013., ASM, 2000 and special metals, 2013)

Form and Condition	Orientation //(Parallel)	HB (Brinell hardness)
Sample 718 (Flat Bar)	//	234
Solution Treated (Flat Bar)	-	341
Hot Rolled (Flat Bar)	-	99
Solution Treated (Flat Bar)	-	277

The compared results indicate based on heat treated condition of the same Brinell hardness traditionally manufactured materials are harder than the sample specimens used for this study. The reason for some of the difference in hardness is that no post heat treatment process was applied to the sample specimens of Inconel 625 and 718.

6.5 XRD (X-RAY Diffraction) Results

Figures 6.19 and 6.20 illustrate XRD peaks at angle of incidence 2θ for Inconel 625 and 718 powder intensity with Miller indices due to XRD from the planes.

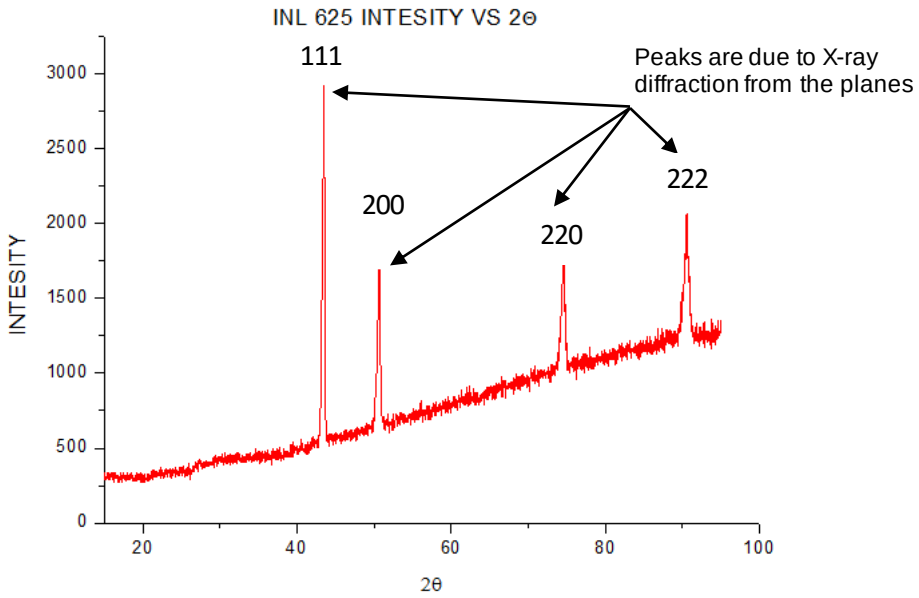

Figure 6.19: Inconel 625 powder Intensity vs diffraction angle denoted with arrows

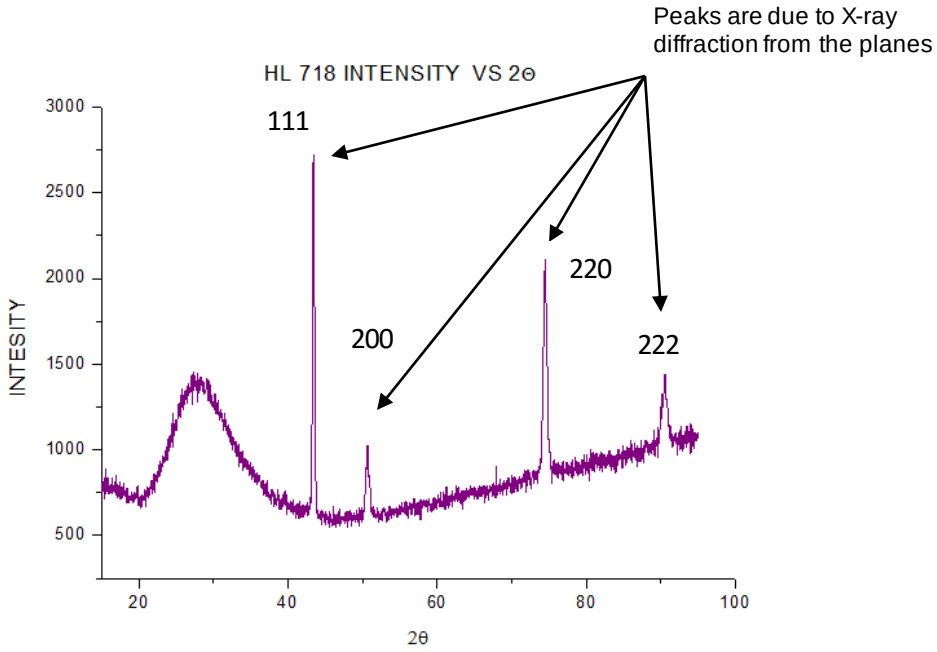

Figure 6.20: Inconel 718 powder intensity vs diffraction angle denoted with arrows

Diffraction results for Inconel 625 and 718 sample specimens were determined using Bragg's Law interplanar spacing data θ scattered angle, 2θ angle of deviation, λ incident wave length and d interplanar distance, as illustrated in Tables 6.10 and 6.11.

Table 6.10: Inconel 625 crystal structure determination of interplanar spacing

X-RAY DIFFRACTION CALCULATIONS							
Inconel 625 crystal structure determination of Interplanar spacing							
2θ	θ	Radii	SINθ	λ (nm)	v	d (nm)	Lattice Values
44.45	22.225	0.387899	0.378245	0.1540598	2	0.203650949	0.352734
50.64	25.32	0.441917	0.427673	0.1540598	2	0.180113835	0.360228
74.48	37.24	0.649961	0.605155	0.1540598	2	0.127289527	0.360029
90.464	45.232	0.789447	0.709964	0.1540598	2	0.108498293	0.375849

Table 6.11: Inconel 718 crystal structure determination of interplanar spacing

X-RAY DIFFRACTION CALCULATIONS							
Inconel 718 crystal structure determination Interplanar spacing							
2θ	θ	Radii	SINθ	λ (nm)	v	d (nm)	Lattice Values
44.37	22.185	0.387201	0.377598	0.15406	2	0.20399955	0.353337586
51.2	25.6	0.446804	0.432086	0.15406	2	0.178274568	0.356549135
75.21	37.605	0.656331	0.610214	0.15406	2	0.126234177	0.357044169
90.8	45.4	0.792379	0.712026	0.15406	2	0.108184104	0.37476073

In cubic systems, the first XRD peaking of the diffraction pattern will be due to diffraction from planes with the lowest Miller indices. To determine atomic radius and crystal structure equations were used with Miller indices defining the first peak, as illustrated in Tables 6.12 and 6.13 below.

Table 6.12: Inconel 625 crystal structure determination of 1st peak

Inconel 625 crystal structure determination of 1st peak			
Crystal structure	FCC	BCC	SC
D spacing	0.203651	0.203651	0.203651
first peak indices	111	110	100
root of indices	1.732051	1.414214	1
Lattice Value	0.352734	0.288006	0.203651
Lattice	2.828427	2.309401	2
atomic radius	0.12471	0.12471	0.101826
Unit cell volume	0.043888	0.023889	0.008446
Sphere volume	0.032477	0.017678	0.006252

Table 6.13: Inconel 781 crystal structure determination of 1st peak

Inconel 718 crystal structure determination of 1st peak			
Crystal structure	FCC	BCC	SC
D spacing	0.204	0.204	0.204
first peak indices	111	110	100
root of indices	1.732051	1.414214	1
Lattice Value	0.353338	0.288499	0.204
Lattice	2.828427	2.309401	2
atomic radius	0.124924	0.124924	0.102
Unit cell volume	0.044113	0.024012	0.00849
Sphere volume	0.032665	0.016333	0.00816

With regards to the peak interplanar spacing for Inconel 625 and 718 it was observed that the peak interplanar spacing decreased as the micro-surface structure was subject to tension, with the X-ray diffraction wavelength kept constant. The peak lattice length initially remained constant from 0 to 75 degrees, with the beam wavelength kept constant, and then approached a linear dependence for a highly beamed state. The dependence of peak lattice length on the X-ray diffraction angle 2θ can be described for the range of materials to investigate crystal structure behaviour at any wavelength.

Using the experimental information data for structure defining first peak illustrated from the tables above Inconel 625 sample atomic radius result was $0.1247\,nm$ .and Inconel 718 sample atomic radius $0.1249\,nm$. The cubic rule for FCC states that the Miller indices must be all odd or even to allow reflection. The Miller indices for the first four peaks of FCC must

be (111), (200), (220), (222). The BCC structure Miller indices, the sum of indices must be an even number. In Figures 6.17 and 6.18 shows the Miller indices for the first four peaks for sample specimens of Inconel 625 and 718 were (111), (200), (211), (222), as in Tables 6.12 and 6.13.

The atomic Radii and crystal structures for 16 metals illustrated below in Table 6.14, in comparison with the first peak experimental data for both Inconel 625 and 718 sample specimens closely matched the atomic radius $0.1246\,nm$ of nickel element with crystal structure lattice FCC. Therefore, this match confirms that the Inconel 625 and 718 sample specimens used for XRD for this paper were nickel-based metals with crystal structure lattice FCC based on the XRD results.

Table 6.14: Atomic Radii and Crystal Structures for 16 Metals (Callister and Rethwisch 2007)

Metal	*Crystal Structure*[a]	*Atomic Radius*[b] *(nm)*	*Metal*	*Crystal Structure*	*Atomic Radius (nm)*
Aluminum	FCC	0.1431	Molybdenum	BCC	0.1363
Cadmium	HCP	0.1490	Nickel	FCC	0.1246
Chromium	BCC	0.1249	Platinum	FCC	0.1387
Cobalt	HCP	0.1253	Silver	FCC	0.1445
Copper	FCC	0.1278	Tantalum	BCC	0.1430
Gold	FCC	0.1442	Titanium (α)	HCP	0.1445
Iron (α)	BCC	0.1241	Tungsten	BCC	0.1371
Lead	FCC	0.1750	Zinc	HCP	0.1332

[a] FCC = face-centered cubic; HCP = hexagonal close-packed; BCC = body-centered cubic.
[b] A nanometer (nm) equals 10^{-9} m; to convert from nanometers to angstrom units (Å), multiply the nanometer value by 10.

XRD data are compared to reference patterns to determine what phases are present. According to Speakman (n.d), when using more peaks, for example 6 peaks and more, from 50° for 2θ accurate when solving lattice parameters, calculating crystallite size improves precision by one to two orders of magnitude. The more peaks used, the more accurate all calculation will be over a longer angular rage, thus all major peaks should be listed in the reference pattern for good results. There are many factors which may affect the results. The most common factor for loss of minor reference peaks during analysis is background noise.

CHAPTER 7

7.0 CONCLUSION

The goal and aim of this work has been to study and analyse the influence of microstructure on mechanical behaviour of 3D additively manufactured Inconel 625 and 718. The plastic deformation behaviour was studied and experimental methods were used to quantify grain structures and mechanical properties.

Additive manufactured Inconel 625 and 718 produced greater mechanical properties which include yield and tensile properties than cast and wrought (commercially produced) Inconel. The grain size and distribution had a major impact on tensile characteristics of both Inconel 625 and 718. Furthermore the structures were composed of multiphase with different grain size distribution. The hardness test shows that values of both 625 and 718 are greater compared to cast and wrought (commercially produced) Inconel. The study of grain size effects on the mechanical properties of Inconel 625 and 718 should be done in conjunction with the effects of other microstructural features such as phase and grain orientation in order to obtain more detailed grain size analysis and accurate results**.**

Three-point beam bending method has been proven to be an alternative method to determine mechanical properties of materials and relationships between mechanical properties were established. Tensile strength and elastic modulus can be compared to bending modulus, and hardness values can be obtained from tensile strength. This implies that instead of conducting a tensile test to obtain tensile value, a three-point beam method can be used to obtain all values (Tsotetsi et al., 2018). The accuracy of the conversion mainly depends on the accuracy of the data collected during the experimental test done. Three-point bending results of testing method are sensitive to specimens and loading geometry and strain rate.

According to Chauhan and Mehta (2018), hardness conversion results have been calculated and are dependent on material properties and characteristics. The correlation between bending, tensile and hardness test values should be used for comparative purposes at this stage only.

Additive manufacturing methods are an asset for rapid manufacturing of components and parts with complex shapes, and increased mechanical properties. Additive manufacturing has potential to decrease the manufacturing time and cost of complex components or parts used in extreme conditions in the near future.

7.1 Future work

Due to time constraints, some experiments were left for future research.

The post heat treatment which affects phase transformation, transformation rate and microstructure, which in turn has an effect on mechanical properties of the additive manufactured samples. This process will determine the combination between grain size, phase transformation (physical state change) and transformation rate.

Future research may include different numerical techniques that may reduce simulation errors during analysis. The numerical simulations of the tensile test in this study implemented ANSYS, a simulation software program using FEM (Finite Elements Method) code. FEM among other methods can determine the micromechanics of materials which are based on solving continuum mechanics problems.

References

3D Material Tech. 2013. Heat treatment superalloys. Available: http://www.3dmaterialtech.com/pdf/3DMT%20718%20Data%20Sheet.pdf [Accessed 29 September 2018].

Aircraft Materials. 2013. Nickel Alloy 625 and 718 / Inconel Mechanical properties. Available: https://www.aircraftmaterials.com/index.html [Accessed 1 October 2019].

Askeland, D. 1985. *The Science and Engineering of Materials*. PWS Engineering: USA.

ASM. 2000. *ASM Specialty Handbook: Nickel, Cobalt, and Their Alloys*. Materials Park, OH: ASM International.

ASM. 1985. *Metals Handbook Ninth Edition Volume 9*. Materials Park, OH. ASM International.

ASM.1997. *Hardness Test*. Available: http://pmt.usp.br/pmt3402/material/E140.13879.pdf [Accessed 16 July 2019].

ASTM. 2017.*Standard Test Methods for Flexural Properties of Unreinforced and Reinforced Plastics and Electrical Insulating Materials*.
Available: https://www.astm.org/Standards/D790.htm [Accessed 7 May 2019].

ASTM. 2014. *ASTM Standard F3055-14a- Standard Specification for Additive Manufacturing Nickel Alloy (UNS N07718) with Powder Bed Fusion and ASTM Standard F3056-14e1- Standard Specification for Additive Manufacturing Nickel Alloy (UNS N06625) with Powder Bed Fusion*, West Conshohocken, PA.

ATM. 2019. *Metallography / Materialography Machines and Equipment for an Informative Sample.* Available:
https://www.atmm.com/products?gclid=Cj0KCQiAnY_jBRDdARIsAIEqpJ0Eiynzlc-JQHY8hq0vDked5TLL9AQfVvw4HAm3gp8QKqq-Sw2y2SEaAvMiEALw_wcBoroughly
[Accessed 12 January 2019].

American Elements. 1998. *The Materials Science Manufacturer.*
Available: https://www.americanelements.com/inconel-625-powder#section-properties
[Accessed13 April 2018].

Anam, A. 2018. Microstructure and mechanical properties of selective laser melted superalloy Inconel 625. Masters thesis. University of Louisville. Kentucky. USA.

ARC. n.d. *Miller Indices*. Available from: https://web.iit.edu/sites/web/files/departments/academic-affairs/academic-resource-center/pdfs/Miller_Indices.pdf [Accessed 27 November 2019].

AZO Materials. 2018. *A Comparison of Selective Laser Melting (SLM) and Direct Metal Laser Sintering (DMLS).* Available: https://www.azom.com/article.aspx?ArticleID=16683 [Accessed 11 September 2018].

Badiru, B., Valencia, V and Liu., D. 2017. *Additive Manufacturing Handbook: Development for the Defence Industry*. crc press, Taylor and Francis group.

Belytschko, T., Liu, W and Moran, B. 2003. *Nonlinear Finite Element for Continua and Structures*. England: John Wiley and Sons Ltd.

Benson, J. and E. Snyder. 2015. The Need for Powder Characterisation in The Additive Manufacturing Industry: The Establishment of a National Facility. *South African Journal of Industrial Engineering*, 26(2): 104-114, August.

Bhadeshia, H. 2003. *Nickel-Based Superalloys*. Available: http://www..phase-trans.msm.cam.ac.uk/2003/Superalloys.html [Accessed 15June 2018].

Bodycote. 2019. *Solute and age Nickel alloys.* Available: https://www.bodycote.com/services/heat-treatment/solution-and-age/solution-and-age-nickel-alloys/ [Accessed 10 October 2018].

Brand, M. 2016. Mechanical Properties and Microstructure Evaluation of Power BED Fused Inconel 625 Nickel Alloy. Masters thesis. New Mexico Institute of Mining and Technology, New Mexico. Available: https://permalink.lanl.gov/object/tr?what=info:lanl-repo/lareport/LA-UR-16-22684 [Accessed 24 April 2019].

Brandtberg, S. 2017. Microstructural inhomogeneity and anisotropic properties in IN-718 structures fabricated by Electron Beam Melting. Masters thesis. Linköping University, Linköping, Sweden. Available: https://pdfs.semanticscholar.org/e609/6a9339d0ebab81bf5edfd438fbf0dc773c07.pdf [Accessed 3 February 2019].

Callister W, Jr. and Rethwisch G. 2007. *Material Science and Engineering 7th.* USA. John Wiley & Sons, Inc.

Callister, D. and Rethwisch. 2012. *Fundamentals of Material Science and Engineering*. 4th.USA. John Wiley and Sons.

Carter, L. 2013. Selective Laser Melting of Nickel Superalloys for High Temperature Application. Doctoral thesis. School of Metallurgy and Materials College of Engineering and Physical Sciences. University of Birmingham, England.

Carroll, B., Palmer, T. and Beese, A. 2015. Anisotropic tensile behaviour of Ti–6Al–4V components fabricated with directed energy deposition additive manufacturing. *Acta Materialia,* 87: 309-320.

Corrosion Materials. 2019. *Effect of Alloying Elements in Nickel Based Alloys*. Available: https://www.corrosionmaterials.com/effects-of-alloying-elements-in-nickel-base-alloys/ 2019 [Accessed 17 September 2019].

Chen, H., Doernberg E., Svoboda, P and Schmid-Fetzer, R. 2010. Thermodynamics of the Al3Ni phase and revision of the Al-Ni system. *Thermochemical Acta,* 512 (1):189-195.

Chauha, J and Metho, V. 2018. *Nano material Volume 1*. Educreation.

Chlebus, E., Gruber, K., Kuznicka, B., Kurzac, J. and Kurzynowski, T. 2015. Effect of heat treatment on the microstructure and mechanical properties of Inconel 718 processed by selective laser melting, *Materials Science and Engineering,* A 693: 647-655.

Decker, R. 1979. *Source Book on Materials for Elevated Temperature Applications*: *Strengthening Mechanisms in Nickel-Base Superalloys*: Ohio American Society for Metals:

Deng, D., Peng, R., Brodin, H. and Moverare, J. 2018. Microstructure and mechanical properties of Inconel 718 produced by selective laser melting: Sample orientation dependence and effects of post heat treatments. *Materials Science and Engineering A*, 713:294-306. January.

Donachie, M and Donachie, S. 2002. *Superalloys: A Technical Guide 2nd*, ed. USA: ASM International.

Dowling, E. 2013. *Mechanical Behaviour of Materials 4th,* ed. England: *Engineering Methods for Deformation, Fracture and Fatigue*. Pearson.

Dieter Jr. G, 1961. *Mechanical Metallurgy.* New York McGraw-Hill.

Dieter, G.1997. *ASM Handbook, Vol 20. Materials Selection and Design* .C R C Press LLC.

EESEM. 2001. *EDX Analysis and WDX Analysis*. Available: https://eesemi.com/edxwdx.htm [Accesses 2 September 2019].

El-Bagoury, N. 2016. Ni based superalloy: casting technology, metallurgy, development, properties and applications. *International Journal of Engineering Sciences & Research Technology*, 5(2).

Elements. 2019. *Material Testing Services*. Available: https://www.element.com/materials-testing-services/x-ray-diffraction [Accessed 19 February 2019].

Farina.2018. *Additive Manufacturing Mechanical Properties*. Available :https://www.farinia.com/additive-manufacturing/3d-materials/mechanical_properties_in_additive_layer_manufacturing_is_all_about_metallurgy_2_of_2 [Accessed 17 September 2018].

Fu, C., Reed, R., Anderson, J. and Krcmar, M. 2004. On the Diffusion of Alloying Elements in the Nickel Base Superalloys. Available: https://www.researchgate.net/publication/223014140_On_the_Diffusion_of_Alloying_Elements_in_the_Nickel-Base_Superalloys [Accessed 2 November 2018].

Gouge, M and Michaleris, P. 2018. *Thermo- Mechanical Modeling of Additive Manufacturing*. USA: Butterworth – Heinemen/ Elsevier.

Glage, A. 2006. *Nickel based Super alloy and their application in the aircraft industry*. Department of Metallurgy Engineering, University of delgi Studi di Trento. Italy. Available: https://www.slideshare.net/Sreekumarr73/nickel-base-superalloys [Accessed 13 August 2018].

Graybil, B., Li, M., Malawey, D., Ma, C., Alvarado-Orozco, J., and Martinez-Franco, E. 2018. Additive Manufacturing of Nickel-Based Super alloys. Available: https://www.researchgate.net/publication/327854594_Additive_Manufacturing_of_Nickel-Based_Superalloys [Accessed 22 September 2019].

Green, W. 2013. The structure of materials. Available: https://www.askwillonline.com/2013/10/the-structure-of-materials.html [Accessed 26 March 2018].

Hafner, B. n.d. *Energy Dispersive Spectroscopy on the SEM*. Characterization Facility University of Minnesota. USA. Available: http://www.charfac.umn.edu/instruments/eds_on_sem_primer.pdf [Accessed 27 August 2019].

HCStarck. 2017. *Amperprint – The powder to create.* Available: https://www.hcstarck.com/hcsadmin/file/ae23e4b25ccebdc3015da241c6df5af9.de.0/AMPERPRINT_alle%20Tabellen.pdf [Accessed 05 May 2019].

Herring, D. 2005. *Grain size and its influence on materials properties*. Available: http://www.heat-treat-doctor.com/documents/grainsize.pdf [Accessed 23 January 2019].

Humphreys, F. 1999. Quantitative metallography by electron backscattered diffraction. *Journal of Engineering*, 195 (3): 170-185. Available: https://doi.org/10.1046/j.1365-2818.1999.00578.x [Accessed 19 August 2019].

Horath, L.1995. *Fundamentals of Materials Science for Technologists*. 3rd edition. Waveland Press, Inc.

Horiba Scientific. 2019. Energy Dispersive X-Ray. Available form: http://www.horiba.com/scientific/products/x-ray-fluorescence-analysis/tutorial/xrf-spectroscopy/ [Accessed 22June 2019].

Hertzberg, R. and Vinci, R. 2013. *Deformation and Fracture Mechanics of Engineering Materials*, 5th. *edition.* New Jersey John Wiley and Sons Inc.

Hosseini, A. and Kishawy, H. 2018. *Machining Difficult to Cut Materials: Basic Principles and Challenges.* Springer International Publishing.

Molitch-Hou, M. 2017. *Issues to Look Out for in Metal 3D Printing*. Available: https://www.engineering.com/3DPrinting/3DPrintingArticles/ArticleID/15202/7-Issues-to-Look-Out-for-in-Metal-3D-Printing.aspx [Accessed 19 September 2018].

Jee, M. 2011. *Engineering Materials: Crystalline structure of Metals.* Available: https://www.slideshare.net/manigee65/l-01 [Access 14 July 2019].

JLC Electromet. 2017. *Nickel Alloy Engineering*. Available: https://www.jlcelectromet.com/jlc600-high-temperature-alloy-grades.html [Accessed 17 September 2019].

JLW Instruments. 1983. *Flex Strength Test*. Available: http://www.jlwinstruments.com/products/test-solutions/flexural-strength-testing/ [Accessed 8 September 2019].

Kabekkodu, S. and Fawcett, T. n.d. International Centre for Diffraction Data. Available: https://www.nist.gov/sites/default/files/documents/mml/1-3_SooryaK_APD_IV.pdf [Accessed 19 February 2019].

Karlik, M. 2001. Lattice imaging in transmission electron microscopy. *Materials Structure*, 1 (8): 3-16.

Karunaratne, S. 2000. *Diffusional Phenomena in Nickel-Base Superalloys.* Cambridge: University Press.

Kasperovich, G Haubrich, J., Gussone, J. and Guillermo Requena. 2016. Correlation between porosity and processing parameters in TiAl6V4 produced by selective laser melting. *Material anddesign*,105:160-170. Available: https://core.ac.uk/download/pdf/77231580.pdf [Accessed 31 October 2019].

Koncar, V. 2018. *Smart Textiles for in Situ Monitoring of Composites*. WoodHead, United Kingdom.

Kopeliovich, D. 2012. *Basic principles of heat treatment*. Available: http://www.substech.com/dokuwiki/doku.php?id=basic_principles_of_heat_treatment [Accessed 28 September 2018].

Kruth, J., Mercelis, P., Van Vaerenbergh, J., Froyen, L. and Rombouts, M. 2005. Binding mechanisms in selective laser sintering and selective laser melting. *Rapid prototyping journal,* 11(1):26–36. February.

Kulkarni, A. n.d. Additive Manufacturing of Nickel-based Superalloys, Thesis, Michigan Technological University, Houghton 49931, USA.

Lufaso, M. n.d. *Physical method for characterizing solids*. Available:https://www.unf.edu/~michael.lufaso/chem4627/ch2_solid_state.pdf [Accessed 3 June 2019].

Lundberg, A. and Eliasson, S. 2015. Effects of Martensitic Phase Transformation on Advancing Cracks in Austenitic Steel Masters thesis Department of Construction Sciences Solid Mechanics. ISRN LUTFD2/TFHF-15/5199-SE (1-70) Division of Solid Mechanics, Lund University, Box 118, SE-221 00 Lund, Sweden.

Losertova, M. 2014. Advanced Materials. thesis, Technical University of Ostrava, Czech Republic.

Maugin, G. 1992. *The thermodynamics of plasticity and fracture*. Cambridge: University Press.

Mantina, M., Wang Chen, L., Liu, Z. and Wolverton, C.2009. First principles impurity diffusion coefficients. *Acta Materialia,* 14(57) 4102–4108.

Malvern. 2017. *Material Characterization Solutions for Powder Metallurgy*. Available: https://www.malvernpanalytical.com/en/assets/MRK2319_tcm50-55142.pdf [Accessed 27 August 2018]

Max Planck Institute. 2003. *EBSD (Electron Backscatter Diffraction).* Available: https://www.mpie.de/2281/en [Accessed 22 June 2019].

Mercelis, P and Kruth, JP. 2006. Residual stresses in selective laser sintering and selective laser melting, *Rapid Prototyping Journal,* 5(12):254-265.

Moletsane, M. 2016. Microstructure and Mechanical Properties of Ti6Al4V (ELI) Parts Produced by DMLS. Masters thesis, Central University of Technology, Free State, Bloemfontein.

Moleejane, C. 2009. An Experimental Investigation of the Effect of Microstructural Features On Mechanical Properties of En8 Steel. Masters thesis, CPUT, Cape Town.

Mohamed, A. 2013. Cyclic Deformation of Hastelloy and Inconel Alloys and Slip Bands Formation International. *Journal of Modern Engineering Research*, 2(3):1253-1255. March Available from: www.ijmer.com [Accessed 27 January 2019].

Mouritz, A. 2012. *Introduction to Aerospace materials*. Reston, Vancouver: Woodhead Publishing.

Mott, R. and Untener, J. 2018. *Applied Strength of Materials 6th edition*. CRC Press, Taylor and Francis Group.

Moris, S. n.d. Determination of Crystal Structures by X-ray Diffraction Sydnie Moris. Available from: https://slideplayer.com/slide/3866732/ [Accessed 19 June 2019].

Moss, D. and Basic, M. 2013. *Pressure Vessel Design Manual 4th edition.* USA. Butterworth-Heinemann.

Nakki, J. 2018. Properties of alloy 625 claddings made with laser and CMT methods. Doctoral thesis. Tampere University of Technology, Tampere, Finland. Available: https://tutcris.tut.fi/portal/files/17117598/n_kki_1593.pdf [Accessed 26 April 2019].

Nash, P. 1992. *AMS Handbook Vol. 3 Alloy Phase Diagrams*. USA. ASM International.

Nannan Guo, M. 2013. Additive manufacturing: Technology, applications and research needs. *Frontiers of Mechanical Engineering,* 3(8): 215-243.

Newage Hardness Testing. n. d. *Rockwell Hardness Test*. Available: https://www.hardnesstesters.com/test-types/rockwell-hardness-testing [Accessed 20 September 2018].

Ott, E., Liu, X., Andersson, J., Bi, Z., Bockenstedt, K., Dempster,I., Groh, J., Jablonski, P., Kaplan,M., Nagahama, D. and Sudbrack, C. 2018. *Proceedings pf the 9th International Symposium on Superalloys 718 & Derivatives: Energy, Aerospace and Industrial Applications.* Springer

Oerlikon, n.d. *Effect of minor elements on properties of C300 Maraging steel parts by SLM process*. Available: https://additiveworld.com/upload/file/20170315%20Additive%20World%20Conference%20-%20Oerlikon.pdf [Accessed 12 February 2019].

Ualberta.ca. 2015. *CCWJ Teaching*. Available: http://www.ualberta.ca/~ccwj/teaching/microscopy/. [Accessed 22 June 2019].

Paranjpe, A. 2014. Residual stresses in machined titanium (Ti-6Al-4V). Doctoral dissertation. The University of Utah.

Petersen- Overleir, E. 2015. Effect of 3D printing on the Microstructure and Mechanical Properties of an Inconel 718 Nickel-alloy (UNS N07718). Masters thesis. Faculty of Science and Technology. University of Stavanger, Norway. Available : https://brage.bibsys.no/xmlui/bitstream/handle/11250/297562/Petersen-Overleir_Eivind.pdf?sequence=1 [Accessed 27 January 2019].

Praxair S.T. Technology. 2016. Material Specifications – TruForm 625 Metal Powder. Available : http://www.praxairsurfacetechnologies.com/-/media/us/documents/brochures/truform-625-metal-powder.pdf?la=en [Accessed 05 May 2019].

Prevey, P.1986. *X-ray Diffraction Residual Stress Techniques. Metal Handbook 10TH*.USA ASM International.

Reed, R. 2008. *The Superalloys: Fundamentals and Applications.* Cambridge: University Press.

Rehman, H. 2016. *Solid Solution Strengthening and Diffusion in Nickel- and Cobalt-based Superalloys.* FAU University Press.

Retima, M., Bouyegh, S., Chadli, H. 2011. Effect of The Heat Treatment on the Microstructural Evolution of the Nickel-based Superalloy**.** *Metalurgija-MJoM*,17(2):71-77.

Sames, W. 2015. Additive Manufacturing of Inconel 718. Doctoral Thesis, Nuclear Engineering, Texas A&M University, Texas.

Shaikh, A. 2018. Development of a γ' Precipitation Hardening Nickel-Base Superalloy for Additive. Thesis, Department of Industrial and Materials Science Chalmers University of Technology, Gothenburg. Sweden. Available : http://publications.lib.chalmers.se/records/fulltext/255645/255645.pdf [Accessed 19 April 2019].

Shoemaker. L. 2005. Alloys 625 and 725: Trends in Properties and Applications. Thesis, Huntington Alloys/ Special Metals Corporation, Huntington, USA.

Smith, F and Hashemi, J. 2010. *Foundation of Material Science and Engineering* 5th *edition*. McGraw-Hill.

Special Metals. 2018. *Inconel alloy 625 and 718*.Avaliable: www.specialmetals.com. [Accessed 30 September 2019].

Small, K. 2017. Characterization of Microstructure and Residual Strain in Inconel 625 Fabricated by Additive Manufacturing. Masters Thesis. Drexel University, Pennsylvania, USA.

Sundararaman, M., Mukhopadhyay, P., Banerjee, S. 1997. Carbide Precipitation in Nickel Base Superalloys 718 and 625 and Their Effect On Mechanical Properties. Thesis, Material Science Division Bhabha Atomic Research Centre, Mumbai, India.

Song, Zhao, B., Li, S., Han, C., Wei, Q., Liu, S and Sh, Y. 2015. Differences in microstructure and properties between selective laser melting and traditional manufacturing for fabrication of metal parts. *Frontiers of Mechanical Engineering* 10(2):111–125.

Speakman, S. n.d. Basics of X-Ray Powder Diffraction. Available: http://prism.mit.edu/xray/Basics%20of%20X-Ray%20Powder%20Diffraction.pdf [Accessed 10 September 2019].

Thelning, K,1967. *Steel and Its Heat Treatment,* Butterworths: Bofors Handbook.

Thorton, R. 2015. *Fracture of Fatigue*. University of Leicester. Available: https://www.le.ac.uk/eg/mct6/teaching/EG2101-L21_RT2014.pdf [Accessed 19 March 2018].

Total Materia. 2001. *Heat Treating of Nickel and Nickel Alloys*. Available: http://www.totalmateria.com/Article32.htm [Accessed 22 April 2018].

Vander Voort, F. 2003. *Metallography of Superalloys.* Buehler Ltd. Available: https://www.buehler.com/solutions/technotes/Superalloy_Metallography_IH-10-03.pdf [Accessed 20 June 2019].

Vande Voort, G. 2012. *Applied Metallography*. New York: Van Nostrand Reinhold Inc.

Wadkar, S., Patil, H. and Tiwari, S. 2017. Simulation of Low Pressure Carburizing and Low Pressure Oil Quenching Process using ABAQUS for Finding Distortions in Component. *Proceedings of the World Congress on Engineering,* (2):1-2. 5-7.

Wang, C. 2010. Study of Deformation Behaviour of Nanocrystal Lline Nickel using Nano Indentation Techniques. PhD dissertation. University of Tennessee, USA.

Wang, X., Gong, X. and Chou, K. 2017. Review on power bed laser additive manufacturing of Inconel 718 parts, *Engineering Manufacture*, 11(231): 1890-1903. January.

Wang, Y, L. Zhen, Shao, W., Yang, L and Zhang, X. 2009. Hot working characteristics and dynamic recrystallization of delta-processed superalloy 718. *Journal of Alloys and Compounds,* 1-2(474): 341-346.

Wikipedia. 2019. *Bragg's law.* Available: https://en.wikipedia.org/wiki/Bragg%27s_law#cite_note-5. [Accessed 19 February 2019].

Wikispaces. 2018. *Materials*. Available: http://tecnolowikia.wikispaces.com/file/view/motor_de_avion_de_titanio.jpg/203748070/394x319/motor_de_avion_de_titanio.jpg [Accessed 13 April 2018].

Young, B.1987. *Process and Materials Selection*. USA. ASM International.

Zaidi, S. 2018. Industrial Materials, Thesis, IQRA College of Technology (ICT) International Islamic University, Islamabad, Pakistan.
Available: https://slideplayer.com/slide/4353931/ [Accessed 01 August 2018].

APPENDIX: The crystal structure determination 2nd, 3rd and 4th peak indices for Inconel 625 and 718

Table 1: Inconel 625 crystal structure 2nd peak indices

Inconel 625 crystal structure determination 2nd peak indices			
Crystal structure	FCC	BCC	SC
D spacing	0.180114	0.180114	0.180113835
2nd peak indices	200	200	110
Root of indices	2	2	1.414213562
Lattice Value	0.360228	0.360228	0.254719428
Latticec	2.828427	2.309401	2
Atomic radius	0.12736	0.155983	0.127359714
Unit cell volume	0.046745	0.046745	0.016526703
Sphere volume	0.034591	0.034591	0.01222976

Table 2: Inconel 625 crystal structure 3rd peak indices

Inconel 625 crystal structure determination 3rd peak indices			
Crystal structure	FCC	BCC	SC
D spacing	0.12729	0.12729	0.127289527
3rd peak indices	220	211	111
Root of indices	2.828427	2.44949	1.732050808
Lattice Value	0.360029	0.311794	0.220471928
Latticec	2.828427	2.309401	2
Atomic radius	0.12729	0.135011	0.110235964
Unit cell volume	0.046667	0.030311	0.010716671
Sphere volume	0.034534	0.02243	0.007930337

Table 3: Inconel 625 crystal structure 4th peak indices

Inconel 625 crystal structure determination 4th peak indices			
Crystal structure	FCC	BCC	SC
D spacing	0.108498	0.108498	0.108498293
4th peak indices	222	222	200
Root of indices	3.464102	3.464102	2
Lattice Value	0.375849	0.375849	0.216996585
Latticec	2.828427	2.309401	2
Atomic radius	0.132883	0.162747	0.108498293
Unit cell volume	0.053093	0.053093	0.010217831

Table 4: Inconel 718 crystal structure 2nd peak indices

Inconel 718 crystal structure determination 2nd peak indices			
Crystal structure	FCC	BCC	SC
D spacing	0.178275	0.178275	0.178275
2nd peak indices	200	200	110
Root of indices	2	2	1.414214
Lattice Value	0.356549	0.356549	0.252118
Latticec	2.828427	2.309401	2
Atomic radius	0.126059	0.15439	0.126059
Unit cell volume	0.045327	0.045327	0.016026

Table 5: Inconel 718 crystal structure 3rd peak indices

Inconel 718 crystal structure determination 3rd peak indices			
Crystal structure	FCC	BCC	SC
D spacing	0.126234	0.126234	0.126234
3rd peak indices	220	211	111
Root of indices	2.828427	2.44949	1.732051
Lattice Value	0.357044	0.309209	0.218644
Latticec	2.828427	2.309401	2
Atomic radius	0.126234	0.133892	0.109322
Unit cell volume	0.045516	0.029564	0.010452

Table 6: Inconel 718 crystal structure 4th peak indices

Inconel 718 crystal structure determination 4th peak indices			
Crystal structure	FCC	BCC	SC
D spacing	0.108184	0.108184	0.108184
4th peak indices	222	222	200
Root of indices	3.464102	3.464102	2
Lattice Value	0.374761	0.374761	0.216368
Latticec	2.828427	2.309401	2
Atomic radius	0.132498	0.162276	0.108184
Unit cell volume	0.052633	0.052633	0.010129